DEVELOPMENT OF AN INTENSITY INTERFEROMETRY ARRAY AND FIRST OBSERVATIONS OF RESOLVED STARS

by

Nolan Matthews

A dissertation submitted to the faculty of
The University of Utah
in partial fulfillment of the requirements for the degree of

Doctor of Philosophy

in

Physics

Department of Physics and Astronomy

The University of Utah

December 2020

The University of Utah Graduate School

STATEMENT OF DISSERTATION APPROVAL

The dissertation of **Nolan Matthews**

has been approved by the following supervisory committee members:

David B. Kieda, Chair(s) **10.29.20**
Date Approved

Kyle Dawson, Member **10.12.20**
Date Approved

Zheng Zheng, Member **10.12.20**
Date Approved

Oleg Starykh, Member **10.12.20**
Date Approved

Elena Cherkaev, Member **10.12.20**
Date Approved

by **Christoph Boehme**, Chair/Dean of

the Department/College/School of **Physics and Astronomy**

and by **David B. Kieda**, Dean of The Graduate School.

ABSTRACT

The techniques employed to study stars often characterize them as point sources due to the limited spatial resolution and extremely small size of most stars in the sky. To spatially resolve stars, the preferred method is interferometry. Modern astronomical interferometric observatories work upon the principle of Michelson interferometry and have been used with great success, particularly in the last two decades, in advancing our knowledge of stellar astrophysics. The emergence of arrays of large diameter optical telescopes and advancement of high-speed digital electronics have revived interest in the once abandoned astronomical technique of intensity interferometry for high angular resolution observations of stars.

An experimental system using imaging air Cherenkov telescopes (IACTs), originally designed for gamma-ray astronomy, was developed for use as an intensity interferometer. This system was successfully deployed onto the four IACTs of the Very Energetic Radiation Imaging Telescope Array System (VERITAS) located near Tucson, Arizona, USA at the Fred Lawrence Whipple Observatory. Stellar angular diameters of the two bright B spectral type stars β CMa and ϵ Ori were measured with an improved uncertainty of less than 5 %, and both were found to be in agreement with past measurements. The observations demonstrated the capability to readily scale intensity interferometry measurements onto an array of several telescopes, with implications for future IACT observatories that will employ many more telescopes with larger baselines advancing the current capabilities of SII observations.

Studies with current and future systems can be used to study several interesting stellar objects and are particularly well suited for characterizing the hottest stars. Generally these include the spectral types O, B, and A, which are still relatively challenging to spatially resolve today given their rarity and typically very small angular sizes. Potential scientific programs include surveying the angular diameters of hot stars, observing the oblation and

temperature gradients of rapidly rotating stars, characterizing the orbital and individual component properties of short period binary systems, and perhaps even performing imaging studies to reveal hot and cold spots on stellar surfaces.

CONTENTS

CHAPTERS

LIST OF TABLES

CHAPTER 1

STELLAR INTERFEROMETRY

1.1 Introduction

Our ability to resolve spatial features of astrophysical objects is a core driver in the study of the cosmos. From Galileo's observations of Saturn's rings in 1610, to the extremely large collection of captivating and detailed images of galaxies produced using modern observatories, improving our angular resolution capabilities has enriched our scientific understanding of the universe and conveyed the fascinating beauty of space to the general public. Despite the immense technological development of astronomical observatories, it remains significantly challenging to spatially resolve a large fraction of stars with a resolution smaller at scales smaller than the diameter. Only a handful of stars have actually been "imaged," although the number has been growing over the last few years. This is due to the extremely small angular extent of most stars in the sky. Indeed, most stars are treated as point sources of light, and information about them is generally extracted through the time evolution of the light intensity and spectrum of the source. By spatially resolving stars, complex phenomena that governs their dynamics can be revealed and then used to further our understanding of stellar physics.

The Rayleigh criterion states that the angular resolution of a telescope is proportional to the wavelength of the light divided by the diameter of the mirror, i.e., $\theta \sim \lambda / D$ (Hecht, 2010). Most stars exhibit an angular diameter on the order of 1 milli-arcsecond requiring a telescope with $\sim 100\,\mathrm{m}$ diameter at a visible wavelength of $500\,\mathrm{nm}$. To resolve stellar features at $1/10$th of the diameter then requires a telescope with a diameter of $1\,\mathrm{km}$. Clearly, construction of such an optical telescope is unfeasible, but these resolutions can be obtained using a synthetic aperture through interferometery. Interferometry makes use of multiple, spatially-separated telescopes in combination to achieve an angular resolution that is effectively equivalent to that of a single telescope with a diameter equal to the separation of the telescopes (Labeyrie et al., 2006). The angular resolution then goes as

$\sim \lambda/B$ where B is the separation of the telescopes.

Current state of the art optical interferometry observatories all utilize Michelson interferometry, often referred to as “amplitude” or “direct” interferometry. An alternative to direct interferometry (DI), and the focus of this work, is “stellar intensity interferometry” (SII). SII was originally pioneered in the 1950s by Robert Hanbury-Brown and Richard Q. Twiss, culminating with construction and operation of the Narrabri Stellar Intensity Interferometer (NSII) that operated from 1963 to 1974 (Hanbury Brown, 1974). After the observations of the NSII, SII was abandoned in astronomy, but has been revived over the past decade. Largely, this is due to the possibility to outfit current and future observatories with SII capabilities (LeBohec and Holder, 2006; Pilyavsky et al., 2017a) leading to several independent efforts towards a modern intensity interferometer (Tan et al., 2016; Zampieri et al., 2016; Weiss et al., 2018; Zmija et al., 2020), with successful on-sky measurements of correlated starlight intensity fluctuations (Guerin et al., 2017, 2018; Matthews, 2019; Acciari et al., 2020). Notably, astrophysical measurements are being performed with distance calibration to the luminous blue variable P Cyg (Rivet et al., 2020) and stellar angular diameter measurements of two bright stars (Abeysekara et al., 2020). Many of these efforts were spawned due to the realization that imaging air Cherenkov telescope (IACT) arrays used in ground-based gamma-ray astronomy were also well-suited for performing SII measurements (LeBohec and Holder, 2006). These observatories employ very large telescopes, each typically greater than 10 m in diameter, and are dispersed in an array with separations between telescopes ranging from tens to hundreds of meters, thus making them capable for SII studies. Simulations of SII with IACT arrays demonstrated the feasibility of performing SII observations of stars several magnitudes fainter than the NSII, with limiting magnitudes comparable to current OAI observatories (Rou et al., 2013). Chapter 1 presents an overview of the SII technique, its application in astronomy, and presents scientific motivation for pursuing a modern SII observatory. Furthermore, particular considerations for implementing an SII system onto IACT arrays arise due to unique optical properties of IACTs, and the implications of these constraints are reviewed.

The core focus of this work was towards the development of an experimental system that is now used for SII observations during bright moon periods at the Very Energetic Radiation Imaging Telescope Array System (VERITAS) gamma-ray observatory. The basic principles of an SII instrument were first demonstrated in the laboratory using a pseudo-thermal light source generated from scattered laser light. The tests were based a similar laboratory experiment that demonstrated SII observations of an artificial star using an array of "telescopes" connected only electronically (Dravins et al., 2015). Temporal and spatial coherence tests separated detectors were performed for several laboratory sources that mimicked single and binary star systems. The results of these initial tests are presented in Chapter 2. However, the expected signal for astrophysical starlight exhibits a signal-to-noise ratio that is several orders of magnitude lower than for the psuedo-thermal light source due to significant differences in the temporal coherence time. To more accurately represent starlight, light from an Hg arc-lamp was substituted for the psuedo-thermal light source. The coherence time, and therefore the signal-to-noise, is comparable to stellar sources, allowing it to serve as a more valid test of the instrumentation. Significant challenges were encountered in measuring the coherence properties of the arc-lamp source due to the effects of radio-frequency interference leading to spurious correlations. A background correlation measurement was performed by measuring the light in orthogonal polarizations, or at large detector separations where coherence was destroyed, but spurious correlations remained. The inclusion of the background subtraction allowed us to detect the spatial coherence of the arc-lamp source demonstrating a working SII laboratory setup. The coherence was measured in two separate regimes, both at high flux using correlations of a continuous current from the detector, and at low flux, where individual photons could be identified. These results on the measurements on the coherence of thermal light are presented and shown in Chapter 4.

Once a working laboratory setup with a thermal light was demonstrated, the system was scaled to allow for operation on the VERITAS telescopes. Chapter 5 provides a description of the instrumental setup, including discussions of the camera, data acquisition system, correlator, and data analysis. Initial commissioning was performed in Fall 2018 with the first on-sky tests beginning in December 2018. Coherent fluctuations between two of the VERITAS telescopes were seen in January 2019 of the two sources γ Orionis and κ Orionis. Additional SII capabilities were then installed on the other two VERITAS telescopes, enabling full 4-telescope SII observations. Observations with the system have been ongoing, and recent results are measured the stellar angular diameter measurements of the two bright blue giant and blue supergiant stars β CMa and ϵ Ori with a precision of less than 5% (Abeysekara et al., 2020).

1.1.1 Brief historical context

In 1921, Albert A. Michelson and F. G. Pease measured the stellar angular diameter of α Orionis (Betelgeuse) using a 20 ft. stellar interferometer located on the top of Mount Wilson in California (Michelson and Pease, 1921). This was the first time the angular diameter measurement was performed for a star other than our own Sun, marking the birth of observational stellar interferometry. The same interferometer was then used to measure the angular diameters of six other stars (Pease, 1921a,b) all on the order of tens of mas. In an attempt to increase the number of measurable stars, Pease built a stellar interferometer with a baseline of up to 50 ft thus in principle allowing for angular diameter measurements of smaller stars. However, he was unable to attain consistent results due to the effects of atmospheric turbulence. It was not until almost 30 years later with the development of the intensity interferometer that the problem of atmospheric turbulence could be overcome.

The intensity interferometry technique is relatively insensitive to path length fluctuations induced by the Earth's atmosphere and therefore allows for arbitrarily large baselines. After the theoretical basis of the technique was formally developed by Hanbury-Brown and Twiss, first for radio-waves (Hanbury Brown and Twiss, 1954) and then for optical light (Hanbury Brown and Twiss, 1957), a "pilot model" of an optical stellar interferometer was built by Hanbury-Brown using borrowed Army searchlight mirrors. This interferometer was successfully used to measure the angular diameter of α Canis Majoris (Sirius). These successes, albeit not without controversy, paved the way towards the funding and construction of the Narrabri Stellar Intensity Interferometer (NSII). The principal achievement of the NSII was the measurement of the stellar angular diameter of 32 stars (Hanbury Brown et al., 1974a), expanding the total number of known angular diameters from Michelson and Pease by over a factor of 6. There were also several other notable achievements. The orbital parameters, individual stellar angular diameters, and even the distance to the interacting binary star system α Virginis (Spica) were all measured through NSII observations that spanned from 1966 to 1970 and were performed jointly with spectroscopic observations (Herbison-Evans et al., 1971). Observations of the system γ Velorum revealed an extended emission-line region that was approximately five times that of the star photosphere (Hanbury Brown et al., 1970). Their work established the theoretical foundation for many important topics of stellar physics that can be studied with an interferometer, including stellar limb-darkening, rapid rotators, estimation of effective temperatures from angular diameters, binary systems, and Cepheid variables (Hanbury Brown and Twiss, 1958a). Eventually, the capabilities of the NSII were exhausted after the observations of all stars in the Southern hemisphere with visible band magnitudes brighter than +2.5. NSII observations of a star near the limiting magnitude typically required over 75 hours. Additional limitations in the electronics prevented reasonable observations of dimmer stars. While plans for a future stellar intensity interferometer were ongoing in the early 1970s, technical developments in direct interferometry provided superior sensitivity with much smaller telescopes, and the intensity interferometry technique was abandoned in astronomy.

In 1970, Antoine Laberyie described the first of these breakthroughs with the creation of speckle interferometry (Labeyrie, 1970). Simply put, the effects of atmospheric turbulence can be removed by recording images at timescales faster than atmospheric turbulence, on the order of a few tens of ms for visible light. Such rapid observations "freeze out" the atmosphere, and diffraction-limited imaging of the telescope can be achieved. Further developments from Laberyie led to the measurement of the visibility of interference fringes resulting from the superposition of light from two optical telescopes separated by 12 meters during observations of α Lyrae (Vega) (Labeyrie, 1975). These observations were the first successful demonstration of a Michelson interferometer since the observations of Michelson and Pease made almost 50 years earlier and set off a resurgence of interest in the technique.

The realization of optical long baseline interferometry with multiple apertures (telescopes) via the amplitude interferometry technique has been developed with amazing success. There are now several major observatories world-wide including the Center for High-Angular Resolution Astronomy (CHARA),[1] the Navy Precision Optical Interferome-

---

[1] http://www.chara.gsu.edu/

ter (NPOI),[2] and the Very Large Telescope Interferometer (VLTI).[3] Some notable results include the angular diameter measurements of hundreds of stars (Duvert, 2016), observation of periodic changes in the angular diameter of Cepheid variable stars (Kervella et al., 2017), and mapping the orbits of stars at the center of the Milky Way (Gravity Collaboration et al., 2018). Stellar imaging is now possible for numerous types of stellar systems and used to observe the oblation of rapidly rotating stars (Che et al., 2011), expansion of nova ejecta (Schaefer et al., 2014), eclipse of a star by a companion (Kloppenborg et al., 2010), and convective cells on giant stars (Paladini et al., 2018). For a more comprehensive review of the capabilities and results produced with modern interferometers see Ridgway et al. (2019) and van Belle et al. (2019).

1.2 Coherence properties of quasi-monochromatic light

1.2.1 Temporal coherence

To better understand the basic principles of an intensity interferometer, we first review the properties of quasi-monochromatic light. A quasi-monochromatic source emits light over a finite bandpass $\Delta\lambda$ that is sufficiently narrow such that $\Delta\lambda/\lambda_0 << 1$ where λ_0 is the center-wavelength. Writing it in terms of the angular frequency $\omega = 2\pi c/\lambda$, the electric field can be described as a superposition of harmonic functions

$$E(t) = \int_{\Delta\omega} E(\omega)\cos\left(\omega t + \phi(\omega)\right) d\omega \tag{1.1}$$

where $E(\omega)$ and $\phi(\omega)$ are frequency dependent amplitude and phase factors. The intensity of the field can be calculated as $I(t) \propto |E(t)|^2$. In the optical/visible domain, the oscillations of the electric field are far too rapid to detect, and therefore any practical measurement device averages the intensity over some time duration T where the averaged intensity is

$$\langle I(t)\rangle \propto \frac{1}{T}\int_0^T |E(t)|^2 dt. \tag{1.2}$$

For monochromatic light, the electric field will oscillate at a frequency $\nu = c/\lambda$ and

---

[2] http://www2.lowell.edu/rsch/npoi/index.php

[3] https://www.eso.org/sci/facilities/paranal/telescopes/vlti.html

the intensity is given by the square of the electric field. For quasi-monochromatic light, a time-varying amplitude of the electric field arises due to the beating of different frequency components. The timescale of these amplitude variations is commonly referred to as the light coherence time and corresponds to the optical bandwidth of the light $\tau_c = 1/\Delta\nu$. For the case of a simple rectangular bandpass, the coherence time written in terms of the wavelength is

$$\tau_c = \frac{\lambda^2}{c\Delta\lambda}. \tag{1.3}$$

The electric field of a quasi-monochromatic light was simulated for $\lambda_0 = 500\,\mathrm{nm}$ and a bandpass of $\Delta\lambda = 1\,\mathrm{nm}$ and is shown in Figure 1.1. The integral in Equation 1.1 was performed by summing over 10000 uniformly spaced frequencies within the optical bandwidth. A random phase was given to each frequency component uniformly distributed between 0 and 2π radians. Additionally, the relative intensity, shown as the dotted black line, is calculated over an integration period that is several times the oscillation time of the field λ_0/c. In Figure 1.1, the rapid oscillations are shown in the inset figure that displays a smaller time window. Over longer timescales, fluctuations of the field amplitude and intensity can be observed over timescales of τ_c. These slower fluctuations demonstrate that interference effects persist even in the case of a finite bandpass with random phases. The fluctuations manifest themselves as correlations of light intensity that can be measured experimentally by different detectors pointed at the same source. So far, only temporal coherence has been discussed and in the next section the effects of spatial coherence are described to illustrate how light intensity correlations vary with respect to the separation of a pair of detectors.

1.2.2 Spatial coherence

The previous section illustrates how quasi-monochromatic light gives rise to temporally coherent fluctuations in the electric field amplitude and overall intensity. The current section extends these ideas to the concept of spatial coherence, or in other words, how these intensity fluctuations change in space for a given spatial configuration of a quasi-monochromatic light source. Consider the scenario depicted in Figure 1.2, consisting of two quasi-monochromatic point sources with a separation a illuminating two detectors at a distance L. Here we assume a far-field approximation $a \ll L$ so the far-field approximation is applicable. In Section 1.2, the electric field of a quasi-monochromatic source was shown to undergo amplitude and phase variations. Including the effects of propagation, the field from either of the sources can be written

$$E(r,t) = A(t)\cos\left(\overline{\omega}t + \phi(t)\right) \tag{1.4}$$

where $\overline{\omega}$ is the mean angular frequency, and $A(t)$ and $\phi(t)$ are the time-dependent amplitude and phase factors. The total electric field at one of the detectors will be given by the superposition of the individual field contributions from each source, where for example, the field at D_1 is

$$E(D_1,t) = E(r_{11}, t - t_{11}) + E(r_{21}, t - t_{21}) \tag{1.5}$$

where t_{11} and t_{21} are the light travel times from the respective sources to the detector. The averaged intensity is then

$$\begin{aligned}\langle I(D_1,t)\rangle = \langle |E(r_{11}, t - t_{11})|^2\rangle + \langle |E(r_{21}, t - t_{21})|^2\rangle \\ + 2\,\mathrm{Re}\{\langle E^*(r_{11}, t - t_{11})E(r_{21}, t - t_{21})\rangle\}.\end{aligned} \tag{1.6}$$

The first two terms on the left hand side of Equation 1.6 are simply the averaged intensities received from either of the point sources in the absence of the other. To simplify the notation, we write $I(\mathbf{r}_{11}) = \langle |E(r_{11},t)|^2\rangle$ and $I(\mathbf{r}_{21}) = \langle |E(r_{21},t)|^2\rangle$. The last term in the above equation results from the interference of the electric fields from both sources and includes the so-called mutual degree of coherence given as the time-averaged correlation of the electric fields from both sources,

$$\Gamma(r_{11}, r_{21}, \tau) = \langle E^*(r_{11}, t)E(r_{21}, t+\tau)\rangle \tag{1.7}$$

where $\tau = t_1 - t_2$ is the relative time delay between the arrival of the fields measured from the point D_1. Both of the electric fields can be described by Equation 1.4, and after substitution into Equation 1.7, the mutual degree of cohererence is

$$\Gamma(r_{11}, r_{21}, \tau) = \langle A_{11}(t)A_{21}(t)\cos\left(\overline{\omega}t + \phi(t)\right)\cos\left(\overline{\omega}(t+\tau) + \phi(t+\tau)\right)\rangle, \tag{1.8}$$

and after use of the trigonometric identity $\cos\theta\cos\Phi = \cos(\theta - \Phi) + \cos(\theta + \Phi)$ we obtain,

$$\Gamma(r_{11}, r_{21}, \tau) = \langle A_{11}(t) A_{21}(t) \cos(\overline{\omega}\tau + \phi(t) - \phi(t+\tau)) \rangle \\ + \langle A_{11}(t) A_{21}(t) \cos(2\overline{\omega}t + \overline{\omega}\tau + \phi(t+\tau)) \rangle. \quad (1.9)$$

The latter time-average term in the above equation can be ignored, as it goes to zero over any practical observation time. The former term remains and so the equation reduces to

$$\Gamma(r_{11}, r_{21}, \tau) = \langle A_{11}(t) A_{21}(t) \cos(\overline{\omega}\tau + \Delta\phi(t)) \rangle \quad (1.10)$$

where $\Delta\phi(t) = \phi(t) - \phi(t+\tau)$. Under the assumption that the amplitude and phase terms are constant over the duration of the integration, and that the amplitudes are equal, $A_{11} = A_{21} = A$, the mutual coherence is

$$\Gamma(r_{11}, r_{21}, \tau) = A^2 \cos(\overline{\omega}\tau + \Delta\phi). \quad (1.11)$$

Substitution of Equation 1.11 into Equation 1.6 then gives

$$\langle I(D_1, t) \rangle = 2A^2(1 + \cos(\overline{\omega}\tau + \Delta\phi)). \quad (1.12)$$

Rewriting $\tau = (r_{11} - r_{21})/c$, and arbitrarily assuming $\Delta\phi = 0$, the averaged intensity is

$$\langle I(D_1, t) \rangle = 2A^2 \left(1 + \cos \frac{\overline{\omega}(r_{11} - r_{21})}{c}\right). \quad (1.13)$$

The above shows that the intensity of the field is dependent on the relative path length that is maximized at a value of $4A^2$ when $\overline{\omega}(r_{11} - r_{21}) = 2\pi n$, where n is a integer, and minimized with a value of 0 when $\overline{\omega}(r_{11} - r_{21}) = \pi n$. In terms of the path length, these criteria correspond to integer and half-integer multiples of the mean wavelength, such that the maxima are at $r_{11} - r_{21} = n\overline{\lambda}$ and the minima at $r_{11} - r_{21} = n\overline{\lambda}/2$, respectively, resulting from the constructive and destructive interference of the two fields.

Now consider the inclusion of detector 2 at a position D_2 as shown in Figure 1.2. The mutual coherence function observed between the two positions will be given by

$$\Gamma(D_1, D_2, \tau) = \langle E^*(D_1, t) E(D_2, t+\tau) \rangle \quad (1.14)$$

that would arise from the superposition of the fields at D_1 and D_2. After normalization, the mutual degree of coherence is related to the complex degree of coherence by

$$\gamma(D_1, D_2, \tau) = \frac{\Gamma(D_1, D_2, \tau)}{\sqrt{I(D_1)}\sqrt{I(D_2)}}. \tag{1.15}$$

If the light received at the points D_1 and D_2 is considered to be coherent (i.e., $\gamma > 0$), then the superposition of those fields will lead to interference fringes. The fringe contrast, commonly known as the *visibility* is given by

$$\mathcal{V} = \frac{\langle I\rangle_{\max} - \langle I\rangle_{\min}}{\langle I\rangle_{\max} + \langle I\rangle_{\min}} \tag{1.16}$$

where $\langle I\rangle_{\max}$ and $\langle I\rangle_{\min}$ are the maximum and minimum values of the intensities produced in the interference pattern. For a fully coherent source $\gamma = 1$, the intensities will vary from a value of zero to a maximum of $4I_0$, where I_0 is the average intensity received from one of the sources, and assumed to be equal for both. In the case of partial coherence where $0 < \gamma < 1$, the visibility of the fringe pattern is reduced. In the general case where the intensities at D_1 and D_2 are equal, the visibility then directly measures the modulus of the complex degree of coherence

$$\mathcal{V}(D_1, D_2) = |\gamma(D_1, D_2)|, \tag{1.17}$$

and therefore can be used to study the temporal and spatial properties of the source. Most optical interferometers rely on the measurement of the visibility to study the sources of interest. Astronomical optical interferometers perform this by bringing the light collected at separate telescopes to a single location for combination. The visibility between all possible telescope pairs can be observed to study the source over a range of angular scales that are inversely proportional to the telescope baselines.

1.2.3 Measuring coherence from intensity correlations

The previous section shows how the mutual degree of coherence can be used to measure the spatial properties of a quasi-monochromatic light source by superimposing the electromagnetic field in the light collected at two separate locations. As first demonstrated by Hanbury-Brown and Twiss (Hanbury Brown and Twiss, 1956), the coherence properties of the source can also result in correlated intensity fluctuations. Consider again the example shown in Figure 1.2, where the intensity at the point D_1 is given by Equation 1.6. A similar procedure can be used to derive the intensity at the point D_2 which is given by

$$\langle I(D_2,t)\rangle = \langle |E(r_{22},t)|^2\rangle + \langle |E(r_{12},t)|^2\rangle + \langle E^*(r_{22},t)E(r_{12},t)\rangle. \tag{1.18}$$

The last term in the above equation results from the interference of the electric fields from both sources. The manner in which they interfere is dependent on the detector locations. When the detectors are at the same location, the electric fields and intensities will follow the same time evolution. When the separation between the sources is non-zero, the electric field at either detector is modulated due to shifts in the relative path length to both sources. For D_1 the relative path length difference is $\Delta_1 = |\mathbf{r}_{11}| - |\mathbf{r}_{21}|$ and similarly for D_2 the path length is $\Delta_2 = |\mathbf{r}_{12}| - |\mathbf{r}_{22}|$.

To better illustrate the concept of spatial coherence and intensity correlations, the scenario depicted in Figure 1.2 was simulated with partially-coherent light for a central wavelength of $\lambda = 500\,\mathrm{nm}$ over a bandwidth of $\Delta\lambda = 10\,\mathrm{nm}$. Multiple frequency components were generated by summing over 10000 frequencies each with random phase. The intensity at each detector, given by Equation 1.5, was simulated over a duration many times greater than the coherence time of the light. The separation of the sources was set to $a = 5\,\mu\mathrm{m}$ and the distance to the detectors was set to $L = 20\,\mathrm{m}$. The left side of Figure 1.3 shows the simulated intensities at both detectors through the black and colored lines, which are varied over a range of baselines separated by a vertical offset. The right side of the figure shows the cross correlation between the simulated intensities of both detectors as a function of the time-lag. For small detector separations, there will be an excess of correlation at timescales less than the coherence time attributed to the coherent fluctuations of the different sources. As the detector separation is increased, the intensities begin to decorrelate until the separation induces a relative path length difference of a half a wavelength $|\Delta_1 - \Delta_2| = \lambda/2$ at which point the intensities are completely uncorrelated.

1.2.4 The van Cittert-Zernike theorem

Consider a quasi-monochromatic extended source with an angular brightness distribution $S(l,m)$ over the orthogonal coordinates l and m that is observed by a pair of detectors at positions in a plane parallel to the source plane. The van Cittert-Zernike theorem states that the mutual degree of coherence observed between the detectors is given by the Fourier transform of the angular brightness distribution

$$\Gamma(u,v) = \int\int S(l,m)e^{-2\pi i(ul+vm)}dl\,dm \tag{1.19}$$

where u and v are separations given in units of the number of wavelengths in the orthogonal coordinates of the detector plane, such that $u = B_u/\lambda$ and $v = B_v/\lambda$, where B_u and B_v are the detector baselines along the u and v coordinates parallel to the l and m axes. If the source angular brightness distribution is normalized by the total intensity, the complex degree of coherence is obtained

$$\gamma(u,v) = \frac{\int\int S(l,m)e^{-2\pi i(ul+vm)}dl\,dm}{\int\int S(l,m)dl\,dm}. \tag{1.20}$$

Therefore, if one knows the angular brightness distribution, the expected complex degree of coherence can be calculated. Conversely, if one measures the complex degree of coherence over a sufficient number of points in the (u,v)-plane, the source angular brightness distribution can be determined by an inverse Fourier transform. In practice, the sampling of the (u,v)-plane is limited by the number of detectors, and for intensity correlations between two detectors the phase information is lost such that interferometric measurements can only provide the modulus $|\gamma|$ of the degree of coherence. To overcome these limitations, sources are often modeled with some apriori assumptions of the general shape. This procedure is known as visibility modeling, used extensively in interferometric observations.

A widely used model for stellar sources is the uniform-disk that approximates the star as a disk with uniform illumination. Due to the rotational symmetry of the source, the degree of coherence can be written in terms of the radial baseline of the detectors $B = \sqrt{B_u^2 + B_v^2}$. For a star of angular diameter θ, the degree of coherence for a uniform-disk model is found as

$$\gamma(B) = 2\frac{J_1(\pi\theta B/\lambda)}{(\pi\theta B/\lambda)} \tag{1.21}$$

where J_1 is the Bessel function of the first kind. In the equation above, there is a first null $\gamma = 0$ at a separation of $B = 1.22\lambda/\theta$, often referred to as the resolving baseline. The relationship also gives the well-known criteria for the angular resolution of a circular optical element $\theta = 1.22\lambda/D$, substituting $B = D$ for the diameter of the element. Figure 1.4 shows plots of $|\gamma|^2$ as a function of r for several uniform-disk sources with diameters ranging from 0.1 to 10.0 mas, typical of most stars. Interferometric measurements of $|\gamma|^2$

over a range of baselines can used to constrain the value of the stellar diameter through fits using Equation 1.21.

The photospheres of stars are not perfect uniform-disks, and more detailed modeling of the stellar surface is needed to accurately describe them. One common extension to the uniform-disk model is to include the effects of limb-darkening. Limb-darkening refers to the reduction of the observed intensity from the center of the star to its limb. There are several forms of limb-darkening models that differ in the radial dependence of the intensity reduction, including linear, quadratic, and exponential approximations. A commonly used linear limb-darkening model is used, where the radial intensity profile I is given by

$$I(\mu) = I(0)(1 - u_\lambda(1-\mu)) \tag{1.22}$$

where u_λ is a wavelength-dependent linear limb-darkening coefficient, and μ is the cosine of the angle subtended between the line of sight and point on the stellar photosphere. The corresponding squared coherence is (Hanbury Brown et al., 1974b)

$$|\gamma(x)|^2 = \left(\frac{1-u_\lambda}{2} + \frac{u_\lambda}{3}\right)^{-2} \left((1-u_\lambda)\frac{J_1(x)}{x} + u_\lambda\sqrt{\pi/2}\frac{J_{3/2}(x)}{x^{3/2}}\right)^2 \tag{1.23}$$

where

$$x = \frac{\pi\theta_{LD}B}{\lambda}. \tag{1.24}$$

1.3 Working principles of a stellar intensity interferometer

Figure 1.5 shows the basic principles of a stellar intensity interferometer. The starlight intensity fluctuations recorded at two telescopes are brought together and correlated to measure the spatial degree of coherence. To compensate for the optical path delay τ between the telescopes, a delay can be inserted between the telescopes to perform the correlation at equal time. Mandel (1963) shows that the normalized intensity correlation of fully polarized light fluctuations is equal to the the squared degree of coherence

$$\frac{\langle \Delta I_1(t)\Delta I_2(t+\tau)\rangle}{\langle I_1\rangle\langle I_2\rangle} = |\gamma_{12}(\tau)|^2 \tag{1.25}$$

where $\Delta I(t)$ is the fluctuating component of the light intensity $I(t) = \langle I\rangle + \Delta I(t)$. A modern convention often used in quantum optics, condensed matter, and particle physics fields denotes the correlation function as $g^{(2)}$ that can be written in terms of temporal and spatial components

$$g^{(2)}(\tau, r_1, r_2) = \frac{\langle I_1(t, r_1) I_2(t+\tau, r_2) \rangle}{\langle I_1(t, r_1) \rangle \langle I_2(t, r_2) \rangle}. \tag{1.26}$$

For thermal light, this intensity correlation function is given by the Siegert relation (Siegert, 1943)

$$g^{(2)} = 1 + |g^{(1)}|^2 \tag{1.27}$$

where $g^{(1)}$ is the first-order correlation function. Rewriting the light intensities in terms of the mean and fluctuating components as done previously, the following equivalences can be found,

$$g^{(2)} - 1 = |g^{(1)}|^2 = \frac{\langle \Delta I_1(t, r_1) \Delta I_2(t+\tau, r_2) \rangle}{\langle I_1(t, r_1) \rangle \langle I_2(t, r_2) \rangle}. \tag{1.28}$$

By comparison of the Equation 1.28 with Equation 1.25, we see $g^{(1)} = \gamma$ such that the first-order correlation function is equivalent to the complex degree of coherence. Lastly, to simplify notation we introduce

$$\Delta g^{(2)} = g^{(2)} - 1 = \frac{\langle \Delta I_1(t, r_1) \Delta I_2(t+\tau, r_2) \rangle}{\langle I_1(t, r_1) \rangle \langle I_2(t, r_2) \rangle}. \tag{1.29}$$

In practice, the light intensity is recorded using an optical and electronic system with finite temporal and spectral resolution that systematically affect the measured correlation. Additional considerations need to be given to other factors including the finite size of the mirrors and spurious correlated noise. In this section, some nonideal properties of a practical SII system are reviewed.

1.3.1 Detector response time and optical bandwidth effects

An intensity interferometer must employ an optical system and photodetectors to measure the light intensity. The temporal and spectral properties of the instrumental system will affect the measured value of the degree of coherence. In this section, a general mathematical treatment of a practical SII system under a semiclassical approximation is provided.

The response of a photo-detector to an incident photon is to produce a single photoelectron due to the photoelectric effect. The single photo-electron is then amplified to generate a current pulse, which is large enough to be measured with an electronic system. The output current $J(t)$ of a detector with a single photo-electron time response $k(t)$ exposed to a light source can be written as

$$J(t) = \sum_j k(t - t_j) \tag{1.30}$$

where t_j are the arrival times of the photons. The average current produced by the detector over some integration period is

$$\langle J(t) \rangle = \alpha \langle I \rangle Q \tag{1.31}$$

where α is the detector quantum efficiency, $\langle I \rangle$ is the average light intensity in units of photons / sec, and $Q = \int_{-\infty}^{\infty} k(t')dt'$ is the total charge produced by the detector due to the emission of a single photoelectron. Mandel and Wolf (1995) in Chapter 9.8.1 show that for the case of fast detectors, where the response time of the detector is much less than the coherence time of the light, the correlation of the detector currents is

$$\langle \Delta J_1(t) \Delta J_2(t) \rangle \approx \alpha_1 \alpha_2 Q^2 \langle \Delta I_1(t) \Delta I_2(t) \rangle \tag{1.32}$$

where upon normalization by the average currents given by Equation 1.31,

$$\frac{\langle \Delta J_1(t) \Delta J_2(t+\tau) \rangle}{\langle J_1 \rangle \langle J_2 \rangle} \approx \frac{\langle \Delta I_1(t) \Delta I_2(t) \rangle}{\langle I_1 \rangle \langle I_2 \rangle} \tag{1.33}$$

such that the normalized correlations of the detector currents are equivalent to the correlations of the light intensity and thus also to the squared degree of coherence by Equation 1.25.

In the typical case of slow detectors, where the resolution time is much longer than the coherence time of the light, Mandel and Wolf (1995) in Chapter 9.8.3, show that the correlations of detector currents for an unpolarized thermal source is

$$\langle \Delta J_1(t) \Delta J_2(t+\tau) \rangle = \frac{1}{2} \alpha_1 \alpha_2 \langle I_1 \rangle \langle I_2 \rangle |\gamma_{12}|^2 T_c \int k(t') k(t'+\tau) dt' \tag{1.34}$$

where T_c is the correlation time of the light. For simple optical bandwidth profiles (e.g., a rectangular bandwidth transmission), the expected correlation time can be given by Equation 1.3. However, for more complicated profiles, a more general definition of the correlation time is

$$T_c = \int |\gamma(\tau)|^2 \, d\tau = \int |\phi(\nu)|^2 \, d\nu, \tag{1.35}$$

relating T_c to the integral of the squared degree of coherence and by Parseval's theorem, is equivalent to the integral of the squared normalized spectral density $\phi(\nu)$. The effective bandwidth of the light can then be determined by the inverse of the correlation time. After normalization of the Equation 1.3 by the average currents, the reduced correlation of detector currents becomes

$$\frac{\langle \Delta J_1(t) \Delta J_2(t+\tau) \rangle}{\langle J_1 \rangle \langle J_2 \rangle} = \frac{1}{2} T_c |\gamma_{12}|^2 K(\tau) \tag{1.36}$$

where

$$K(\tau) = \frac{\int k(t') k(t'+\tau) dt'}{\left(\int k(t') dt' \right)^2}. \tag{1.37}$$

The above equation allows for the characterization of the expected amplitude and temporal dependence of the measured coherence peak from instrumental parameters. The correlation time is given by the measured spectral density, generally set by the optical filter bandwidth, but can also be dependent on the source spectrum and other frequency dependent atmospheric and instrumental transmission factors. The latter term $K(\tau)$ involving the integral over the pulse shape correlation determines the temporal dependence of the measured correlation.

As an example, consider the case of a system that utilizes an optical filter with unity transmission over a bandwidth $\Delta\nu$. Assuming that light spectral density $S(\nu)$ does not change appreciably over the bandwidth of the filter, the normalized spectral density of the light after transmission through the filter is

$$\phi(\nu) = \frac{S(\nu)}{\int S(\nu) \, d\nu} = \frac{1}{\Delta\nu}, \tag{1.38}$$

and after substitution into Equation 1.35 gives the correlation time as $T_c = 1/\Delta\nu$. Now, assume that the time response of the detector is a rectangular pulse of duration T_r. The latter term of Equation 1.36 is then

$$K(\tau) = \frac{T_r - |\tau|}{T_r^2} \tag{1.39}$$

when $|\tau| < T_r$ and zero otherwise. The temporal dependence of the measured correlation function is given by a triangular function reaching zero at values of $|\tau| = T_r$ peaking at

$\tau = 0$, with an amplitude

$$\frac{\langle \Delta J_1(t) \Delta J_2(t) \rangle}{\langle J_1 \rangle \langle J_2 \rangle} = \frac{T_c}{2T_r} |\gamma_{12}|^2, \tag{1.40}$$

which after replacing the resolution time by the electronic bandwidth given by the Nyquist criteria $\Delta f = T_r/2$, and writing the correlation time in terms of the optical bandwidth, we obtain the commonly used relation

$$\frac{\langle \Delta J_1(t) \Delta J_2(t) \rangle}{\langle J_1 \rangle \langle J_2 \rangle} = \frac{\Delta f}{\Delta \nu} |\gamma_{12}|^2 \tag{1.41}$$

that equates the measured correlation function at zero time-lag to the value of the squared degree of spatial coherence multiplied by the ratio of the electronic to optical bandwidth.

Consider now that the detector time response is a Gaussian of unity amplitude with a one standard-deviation width of σ_r. After derivation it can be shown that

$$K(\tau) = \frac{1}{2\sqrt{\pi}\sigma_r} \exp\left(-\frac{\tau^2}{4\sigma_r^2} \right), \tag{1.42}$$

giving the temporal dependence of the cross-correlation as a Gaussian with a standard deviation $\sigma_r' = \sqrt{2}\sigma_r$. The equal-time correlation is now

$$\frac{\langle \Delta J_1(t) \Delta J_2(t) \rangle}{\langle J_1 \rangle \langle J_2 \rangle} = \frac{T_c}{4\sqrt{\pi}\sigma_r} |\gamma_{12}|^2. \tag{1.43}$$

In either case where the detector time-response is approximated as a Gaussian or as a rectangular pulse, the correlation peak width gives a measure of the effective temporal resolution time of the system. This can be a convenient way to characterize nontrivial temporal properties of the instrumental system that may include transit-time jitter of the photodetectors, phase drift of the sampling electronics, or dispersion in the arrival time of photons due to the optical system.

1.3.2 Effects of background light and dark current

In intensity interferometry observations it is necessary to consider the effect of background light as well as the detector signal current or count rate with no incident light. The signal intensity output from a given detector can be modeled as $I(t) = I_\star(t) + I_B(t)$ where $I_\star$ is the starlight intensity, and I_B is the total background intensity including both background light entering the detector and detector dark current. After substituting the expression for the total intensity into Equation 1.29, the normalized correlation becomes

$$\Delta g^{(2)} = \frac{\langle \Delta I_{\star_1} \Delta I_{\star_2} \rangle + \langle \Delta I_{\star_1} \Delta I_{B_2} \rangle + \langle \Delta I_{\star_2} \Delta I_{B_1} \rangle + \langle \Delta I_{B_1} \Delta I_{B_2} \rangle}{\langle I_{\star_1} + I_{B_1} \rangle \langle I_{\star_2} + I_{B_2} \rangle}. \tag{1.44}$$

The cross-terms in the numerator represent the correlation between the starlight and background light and can generally be ignored as, in principle, these are independent from each other. The latter term $\langle \Delta I_{B_1} \Delta I_{B_2} \rangle$ represents the correlation between the background light fluctuations seen in both detectors. Several factors can cause this term to be non-zero, thus systematically affecting the correlation measurement. For example, high energy cosmic rays air that enter our atmosphere generate showers of UV/optical light that would generate correlations between separated telescopes. This effect was investigated by Hanbury Brown and Twiss (Hanbury Brown and Twiss, 1958a) with the conclusion that it should have no effect on intensity interferometry observations unless very wide spectral filters ($\Delta\lambda > 50\,\mathrm{nm}$) are used on sources with visual magnitudes greater than 5. Under the assumption that the fluctuations in the background light are uncorrelated or negligible, the measured normalized correlation is

$$\Delta g^{(2)} = \frac{\langle \Delta I_{\star_1} \Delta I_{\star_2} \rangle}{\langle I_{\star_1} + I_{B_1} \rangle \langle I_{\star_2} + I_{B_2} \rangle}, \tag{1.45}$$

and after solving for normalized correlation due to starlight intensity fluctuations alone, i.e., $\Delta g_\star^{(2)} = \langle \Delta I_{\star_1} \Delta I_{\star_2} \rangle / \langle I_{\star_1} \rangle \langle I_{\star_2} \rangle$, Equation 1.45 is written

$$\Delta g^{(2)} = \frac{\Delta g_\star^{(2)}}{(1+\beta_1)(1+\beta_2)} \tag{1.46}$$

where β is the ratio between the background to starlight intensity, i.e., $\beta = I_B / I_\star$ for each of the respective detectors. Thus, the main effect of uncorrelated background light is to reduce the correlation of starlight intensity fluctuations $\Delta g_\star^{(2)}$ by a factor $(1+\beta_1)(1+\beta_2)$. In the case where the background light is negligible in comparison to the starlight, this factor goes to 1 as expected.

1.3.3 Expectation of the correlation

The relationships shown in the previous section represent an idealized form of the expected signal obtained for an intensity interferometer. When using actual instruments, many parameters must be included that systematically affect the measurement of $\Delta g^{(2)}$. Hanbury Brown and Twiss derive an expression for the expected correlation $c(d)$ between the outputs of two independent detectors considering several realistic parameters (Hanbury Brown and Twiss, 1958b). The equation is modified[4] and reproduced here

$$c(d) = \langle \Delta i_1(t) \Delta i_2(t) \rangle = e^2 A_1 A_2 \beta_0 \alpha_1(\nu_0) \alpha_2(\nu_0) n^2(\nu_0) \sigma B_0 b_\nu |F_{max}|^2 \overline{\Gamma^2(d)} \tag{1.47}$$

where A_1 and A_2 are the light collection areas, β_0 is a polarization factor with $\beta_0 = 1$ for unpolarized light and $\beta_0 = 2$ for linearly polarized light, $\alpha(\nu)$ is defined here as the normalized transmission at a frequency ν over the entire optical system, including, for example, atmospheric absorption, mirror reflectivity, spectral filter throughput, and detector quantum efficiency, and n is the incident photon spectral density, in units of ph s^{-1} m^{-2} Hz^{-1} where the spectral density is assumed to be equal at both detectors (i.e., $n = n_1(\nu) = n_2(\nu)$). The signal output for each of the detectors can be generally written as $i(t) = eA \int \alpha(\nu) n(\nu) d\nu$. Combining this expression with Equation 1.47, gives the normalized correlation function of the signal outputs

$$\frac{\langle \Delta i_1(t) \Delta i_2(t) \rangle}{\langle i_1(t) \rangle \langle i_2(t) \rangle} = \beta_0 \frac{\alpha_1(\nu_0) \alpha_2(\nu_0) n^2(\nu_0) \sigma B_0 b_\nu |F_{max}|^2}{\int \alpha_1(\nu) n(\nu) d\nu \int \alpha_2(\nu) n(\nu) d\nu} \overline{\Gamma^2(d)}, \tag{1.48}$$

where $b_\nu |F_{max}|^2 = \Delta f_{eff}$ is defined as the effective electronic cross-correlation bandwidth, and σ is the normalized spectral density function

$$\sigma = \int \alpha_1(\nu) n_1(\nu) \alpha_2(\nu) n_2(\nu) d\nu / (B_0 \alpha^2(\nu_0) n^2(\nu_0)). \tag{1.49}$$

After substitution of Equation 1.49 into Equation 1.48, the normalized correlation becomes

$$\frac{\langle \Delta i_1(t) \Delta i_2(t) \rangle}{\langle i_1(t) \rangle \langle i_2(t) \rangle} = \beta_0 \frac{\int \alpha_1(\nu) n_1(\nu) \alpha_2(\nu) n_2(\nu) d\nu}{\int \alpha_1(\nu) n(\nu) d\nu \int \alpha_2(\nu) n(\nu) d\nu} \Delta f_{eff} \overline{\Gamma^2(d)}. \tag{1.50}$$

The term $\overline{\Gamma^2(d)}$ is defined as the normalized correlation function and is given by

$$\overline{\Gamma^2(d)} = \frac{\int |\gamma(d,\nu)|^2 \alpha_1(\nu) n_1(\nu) \alpha_2(\nu) d\nu}{\int \alpha_1(\nu) n_1(\nu) \alpha_2(\nu) n_2(\nu) d\nu}, \tag{1.51}$$

which accounts for the integration of the degree of coherence over a finite bandwidth at a given telescope baseline. For randomly polarized light $\beta_0 = 1$, and subsequently we can draw an equivalence between the terms in Equation 1.51 and Equation 1.47 such that

---

[4] In the original publication, α is defined purely as the detector quantum efficiency but is generalized here as the full optical throughput. Additionally, we assume that there are no losses in the correlator, and so the ϵ parameter in the original equation is set to $\epsilon = 1$.

$$\frac{\langle \Delta i_1(t)\Delta i_2(t)\rangle}{\langle i_1(t)\rangle\langle i_2(t)\rangle} = \frac{\Delta f_{eff}}{\Delta \nu_{eff}}\,\overline{\Gamma^2(d)} \tag{1.52}$$

where the effective cross-correlation bandwidth is defined

$$\Delta \nu_{eff} = \frac{\int \alpha_1(\nu)n(\nu)d\nu \int \alpha_2(\nu)n(\nu)d\nu}{\int \alpha_1(\nu)n_1(\nu)\alpha_2(\nu)n_2(\nu)d\nu}. \tag{1.53}$$

The numerator describes the total intensity measured by each of the detectors, whereas the denominator measures the degree of overlap in frequency. In the case where two different narrow-band filters are used with non-overlapping transmission profiles, $\Delta \nu_{eff}$ goes to infinity, causing the normalized cross-correlation measurement to go to zero. Additionally, the above expressions quantifies the effect of spectral changes in the star due to variability of the spectrum from the source, or perhaps due to attenuation in the atmosphere. Changes that are uniform with respect to frequency do not affect the value of $\Delta \nu_{eff}$, and therefore the measured correlations.

1.4 Practical considerations for SII with imaging air Cherenkov telescopes

IACTs are of an overall optical quality much less than what is standard for conventional optical telescopes. The trade off is that very large light collection areas can be achieved at a much lower cost. While the poor optical quality does not significantly affect their operation as gamma-ray instruments, it does impose some restrictions on their capabilities as intensity interferometers. The large point-spread-function (PSF) increases the background light levels, ultimately determining the observable limiting magnitude. This, along with fast optics typically used in IACTs, makes narrowband filtering more complicated. Additionally, the optics of some IACTs introduce a temporal dispersion amounting to a signal bandwidth limitation.

1.4.1 Time-dispersion of photons

The geometry of some IACT optics introduce a dispersion in the arrival time of photons that otherwise would arrive synchronously. The amount of dispersion is a function of the telescope geometry. The VERITAS telescopes are based on the Davies-Cotton optical design (Davies and Cotton, 1957), where the mirror is composed of 350 hexagonal mirror facets, each with a radius of curvature of 24 m laid along a sphere with a radius of curvature of 12 m and centered on the focal point (Holder et al., 2006). This configuration introduces a difference in the path length between photons that arrive at the center of the mirror in comparison to those that arrive from further out in radius. Thus, the $g^{(2)}(\tau)$ peak for many different pairs of correlated photons would be smeared by the time-dispersion introduced by the telescope optics.

The range in temporal dispersion can understood as the difference in flight time for a pair of initially synchronous photons that, respectively, hit the center and edge of the mirror. Figure 1.6 illustrates the basic geometry of the a primary reflecting surface that is laid out on a sphere following

$$(x - R_c)^2 + r^2 = R_c^2 \tag{1.54}$$

where R_c is the radius of curvature of the mirror with $x > 0$ and $|r| < r_t$ where r_t is the telescope radius. The path length for a photon that initially moves through a point $(x = R_c, r)$ to the focus $(x = R_c, r = 0)$ is

$$l(r) = R_c + \sqrt{R_c^2 - r^2}. \tag{1.55}$$

The light travel time is then $\tau(r) = l(r)/c$. For an f/1 focal ratio, typical of IACT telescopes, $r_t = R_c/2$. The maximum difference in arrival time is then $\tau(r = 0) - \tau(r = r_t) = R_c(1 - \sqrt{3}/2)$. Under this approximation for a dish equal to the size of the VERITAS mirrors $R_c = 12\,\mathrm{m}$, the corresponding time-dispersion range is $\sim 5.4\,\mathrm{ns}$.

While this sets the scale of the temporal dispersion, it is also important to consider the distribution in time-differences for a large number of correlated photons as it affects intensity interferometry observations. Consider a single pair of photons that originally are synchronous (i.e., arrive at $x = 0$ at the same time). The path delay difference between them is

$$\Delta\tau_{ij} = \tau(r_i) - \tau(r_j) \tag{1.56}$$

where the pair of photons land on the radial positions r_i and r_j. An intensity interferometer will average over a large number of correlated photon pairs each reaching the its respective telescope at a random point. The measured correlation function is broadened by the corresponding random difference in time that occurs for many of the correlated pairs. To simulate this, $N_{pairs} = 100000$ independent pairs of photons are generated where each pair is synchronous at $x = 0$ and the location of either photon is uniformly distributed located within the area of the mirror. The difference in time of flight is calculated for each pair, and the overall distribution of time differences is shown in Figure 1.7.

The time dispersion introduced by the optics sets the maximum signal bandwidth that can be used to improve the signal to noise ratio (SNR) of the system. In principle, the SNR is proportional to the square root of the electronic bandwidth, or equivalently, inversely with the square-root of the time resolution. From these arguments, the time dispersion of the VERITAS optics is of order $\sim 4\,\mathrm{ns}$, such that increasing the signal bandwidth beyond 250 MHz does not provide any substantial increase in the SNR.

1.4.2 Collimation and spectral filtering

IACT telescopes generally employ very large light collection areas with focal ratios typically less than 1.5 (referred to as "fast" optics), resulting in a large angular divergence of the light cone arriving at the focal plane. For the VERITAS telescopes, the divergence is $\sim 26^\circ$ for light that arrives from the mirror edge relative to the center. This angular divergence makes it challenging to spectrally filter the light to nanometer scale widths optical bandpasses using narrow-band Fabry-Perot interferometric filters. These filters are designed to work for collimated light with normal incidence. For light that arrives at an angle θ, the spectral throughput of the filter is affected, and to first order, the transmitted wavelength at incident angle θ follows

$$\lambda(\theta) = \lambda_0 \sqrt{1 - \frac{\sin^2(\theta)}{n_{eff}^2}}, \tag{1.57}$$

where λ_0 is the nominal center-band wavelength of the filter for normally incident light, and n_{eff} is the effective coating refractive index. The above equation demonstrates that the degradation of the bandpass can be minimized by choosing filters with higher n_{eff} and lower λ_0, for a fixed bandpass $\Delta\lambda$.

To better quantify the optical bandpass for uncollimated light, we simulate the transmission of a interferometric filter to light reaching it from a circular aperture. For an input spectrum $\eta(\lambda)$ through a filter with a transmission factor $F(\lambda, r)$, the transmission is

$$T(\lambda) = 2\pi \int_0^{r_t} n(\lambda) * F(\lambda, r) r dr. \tag{1.58}$$

Here, we approximate the filter response to be unity when $|\lambda - \lambda(r)| < \Delta\lambda/2$, where $\Delta\lambda$ is the bandpass and $\lambda(r)$ is adapted from Equation 1.57 with $\tan\theta = r/f$. Figure 1.8 shows a simulation of the transmission of uncollimated light from a VERITAS telescope passing through an interferometric filter. The properties of the filter are matched to that currently used in the VERITAS SII system. For light that arrives from an annulus of the mirror at low θ (e.g., from 0° to 7.1°), the transmission of the filter is mostly unaffected. At large θ, the shift in transmitted wavelengths becomes significant, and the transmitted light from outer annuli do not overlap in wavelength with those from the center. The overall throughput of the filter is then skewed when integrating over the entire mirror area, degrading the achievable SNR.

1.4.3 PSF

In Section 1.3.2, we have seen how night sky background (NSB) light reduces the value of the measured spatial coherence by a factor of $(1+\beta)^2$, where β is the ratio between the background to starlight flux for identical optical systems. The signal to noise ratio is reduced by a factor of $(1+\beta)$ (Hanbury Brown and Twiss, 1958b). A region of the sky is integrated within the PSF, and the NSB flux can approach and even exceed that of the starlight. The exact brightness of the NSB is dependent on many factors, for example, the Moon phase, angular separation to the moon, sky-position relative to the galactic plane, and local light pollution. Generally, the NSB flux ranges from $m_V = 18$ to $21.5\,\mathrm{mags/arcsec^2}$ accounting for the variation from full to new moon (Krisciunas and Schaefer, 1991). A PSF diameter of θ_{psf} will then integrate over a solid angle of $A_\theta = \pi\theta_{psf}^2/4$. For a magnitude m, the equivalent spectral density can be approximated as $\eta = \eta_0\,(2.512)^m$, where η_0 is defined as the photon spectral density for a zero-magnitude star in a given spectral band. For the visual (V) photometric band, this corresponds to $\eta_0 \sim 1 \times 10^{-4}\,\mathrm{ph\ m^{-2}\ Hz^{-1}}$ (Bessell, 1979). The total spectral density resulting from the NSB is $\eta_{nsb} = \eta_0 (2.512)^{m_{nsb}} A_\theta$.

Figure 1.9 shows the value of $1+\beta$, or equivalently the reduction in the signal to noise ratio relative to if there was no NSB flux. The calculation is carried out for three different PSF sizes, corresponding to angular PSF diameters of 0.1°, 0.01°, and 1.5″, ranging from sizes typical of IACT telescopes to those of seeing-limited observations. The solid lines are for bright moon conditions where the background light is 18.5 mags/arcsec^2, and the dashed lines indicate dark conditions where the background flux is 21.5 mags/arcsec^2. For a seeing-limited telescope, the NSB flux will not affect the SNR for stars brighter than $m \sim 12$. However, for an IACT telescope, the SNR is drastically reduced under bright moon conditions for visual magnitudes dimmer than ~ 6.

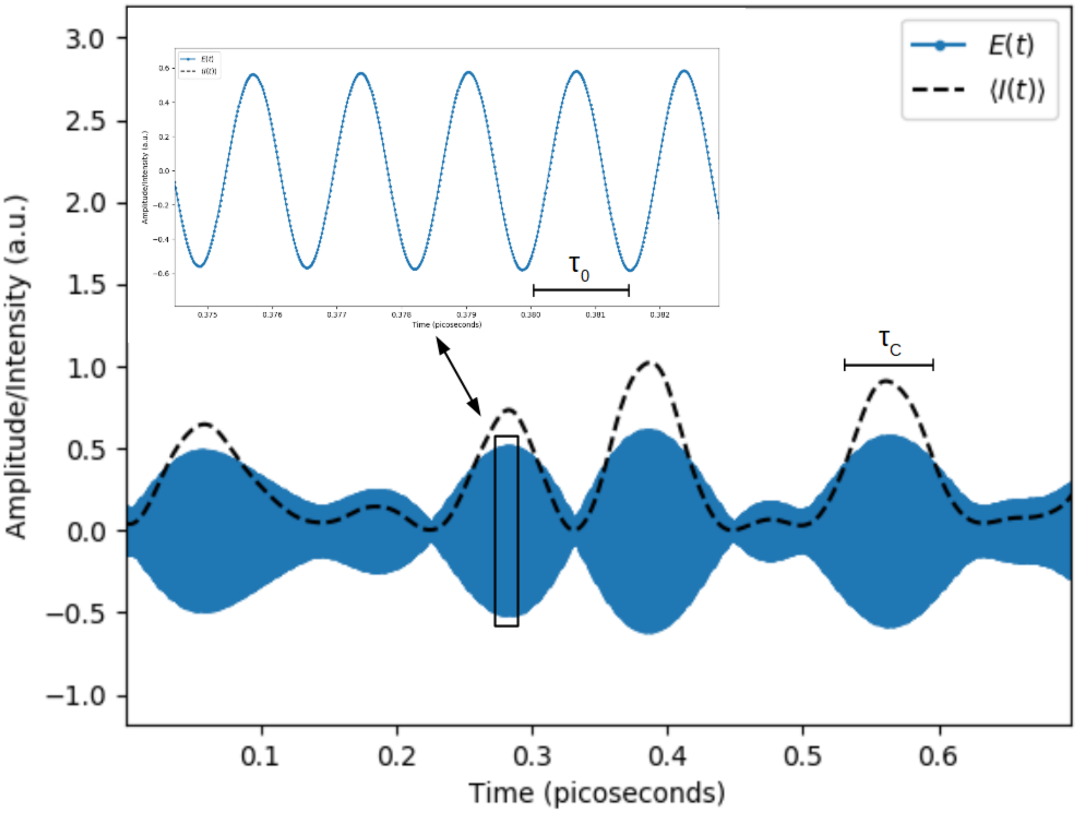

Figure 1.1: Simulations of the electric field and averaged intensity of quasi-monochromatic light of central wavelength 500 nm and bandpass of 10 nm. The blue line shows the electric field, where the dotted black line shows the averaged light intensity. The finite optical bandwidth of the light gives rise to a time-varying amplitude over timescales of the coherence time, which here is ~ 0.08 ps.

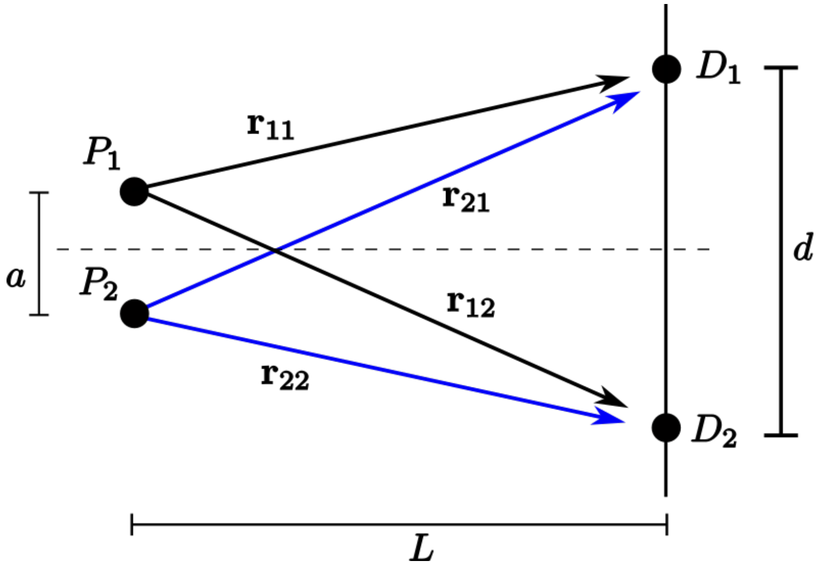

Figure 1.2: Schematic of two point sources illuminating two separated detectors.

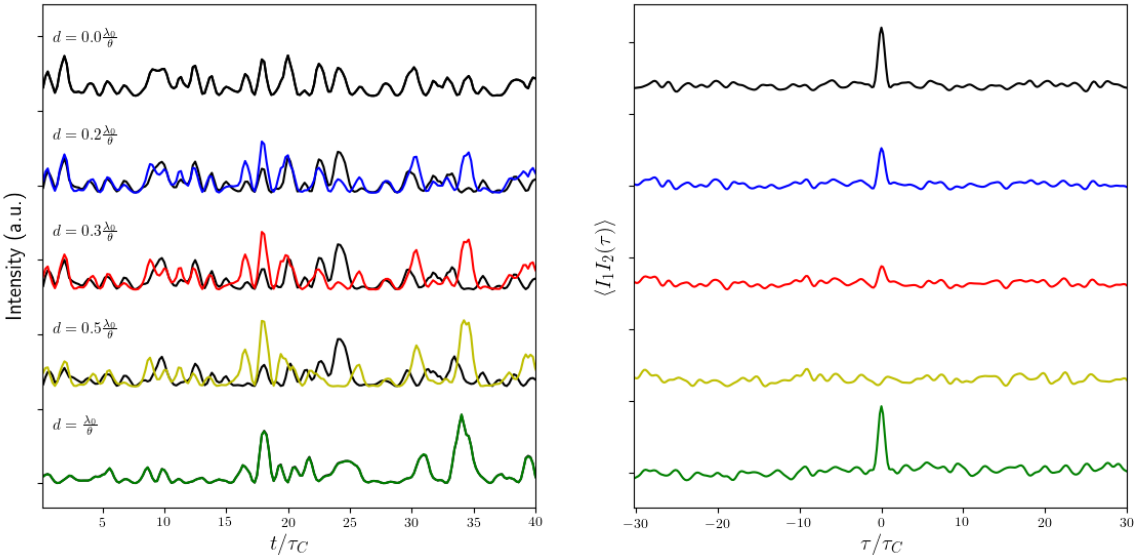

Figure 1.3: Plots of simulated intensities (left) and the intensity cross-correlation (right) for two detectors exposed to a partially-coherent binary composed of two point sources of separation a. The colors indicate the different separations of the detectors and are increasing from the top. As the detector separation is initially increased, the respective intensities at each detector begin to decorrelate and reach a minimum at $d = 0.5\,\lambda/a$ at which point they are completely uncorrelated. As the separation is increased beyond this value, the intensities again start to correlate and are completely correlated at a separation of $d = \lambda/a$, attributed to the binary property of the source.

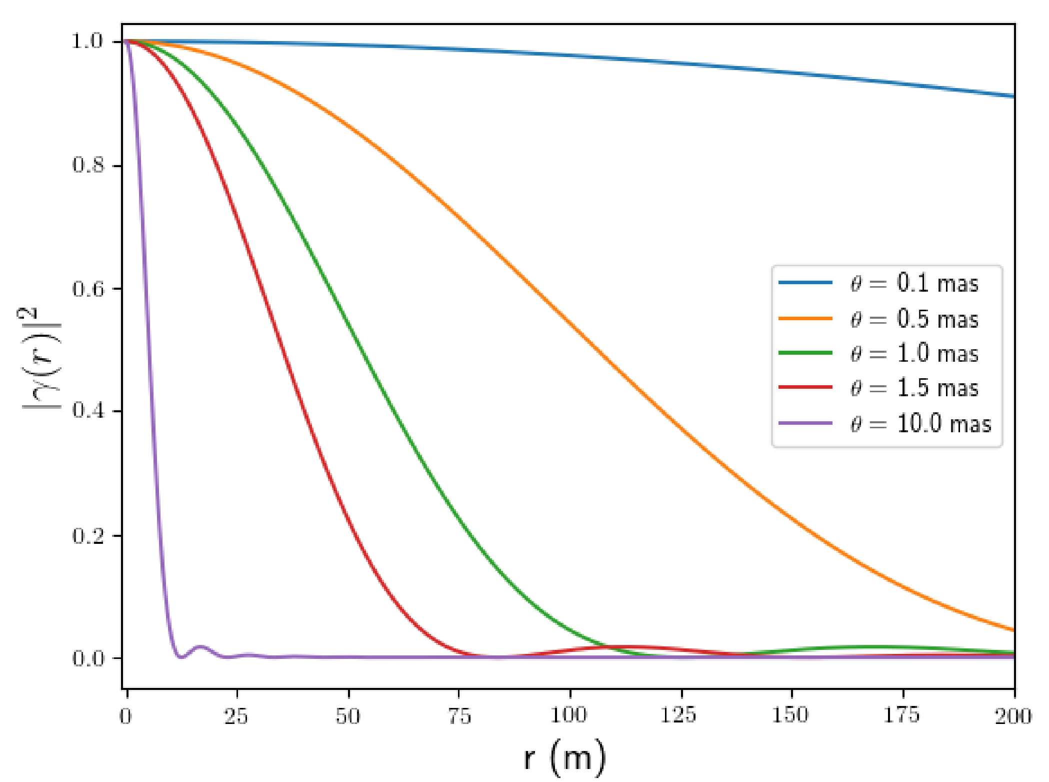

Figure 1.4: Dependence of squared degree of coherence on baseline for several uniform-disk stars of varying angular diameters for an observational wavelength of $\lambda = 500\,\text{nm}$. An interferometer that is able to measure the squared degree of coherence over many baselines can then be used to constrain the angular diameter of the star.

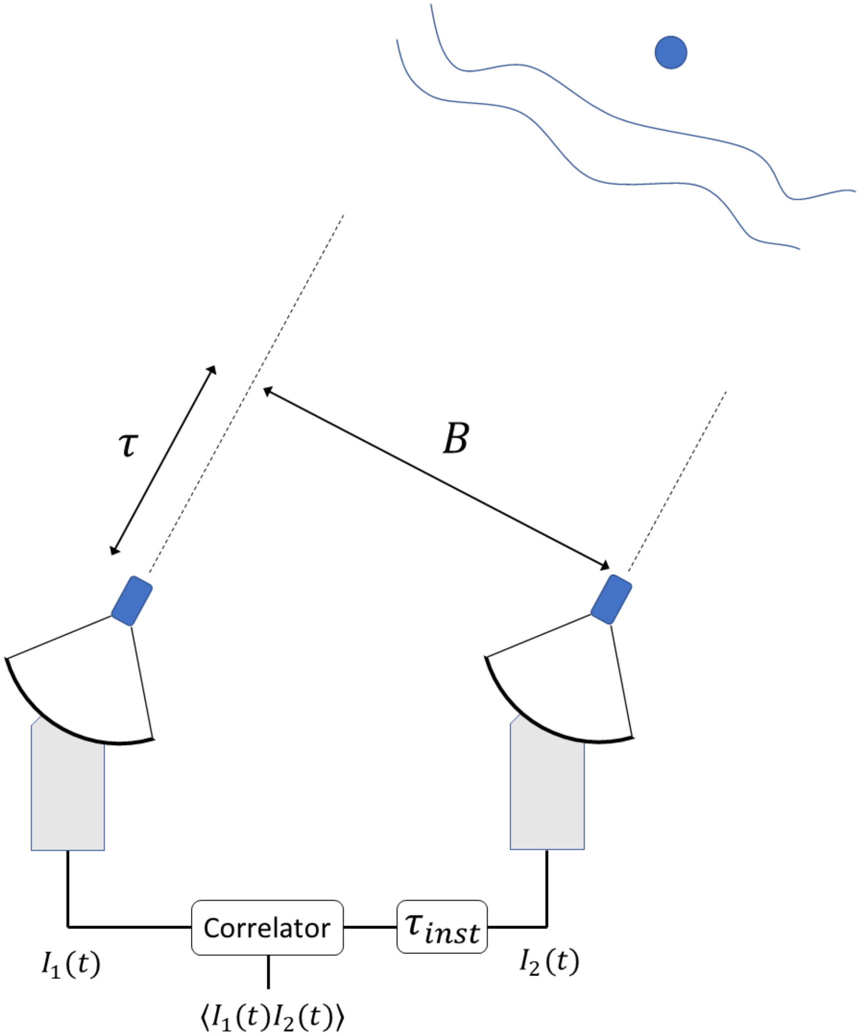

Figure 1.5: Basic schematic of an intensity interferometer. Starlight is collected at two telescopes with a projected separation B and optical path delay τ. The intensity $I(t)$ is recorded at both telescopes by the use of a photodetector, and after compensation for the optical path delay using an intrinsic delay $\tau_{instr} = \tau$ the equal-time correlation can be performed to measure the spatial degree of coherence.

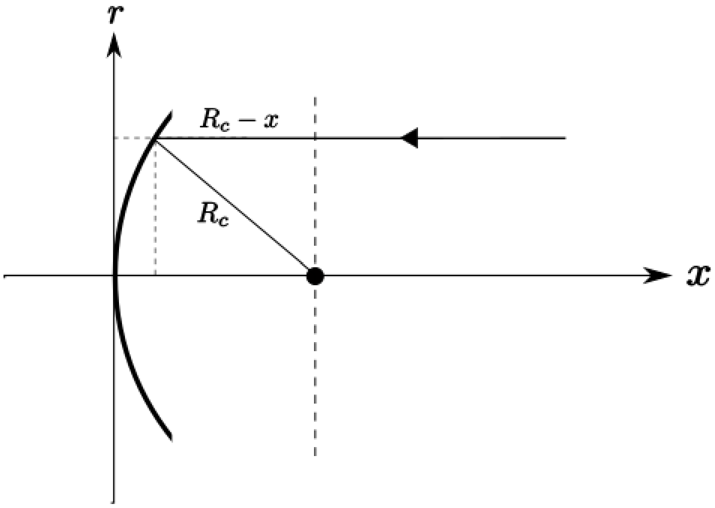

Figure 1.6: Schematic of spherical mirror used to illustrate the time dispersion introduced for some IACT optical designs. Photons that arrive at a radial distance away from the center will have a different path length to the telescope focus which is indicated by the black dot.

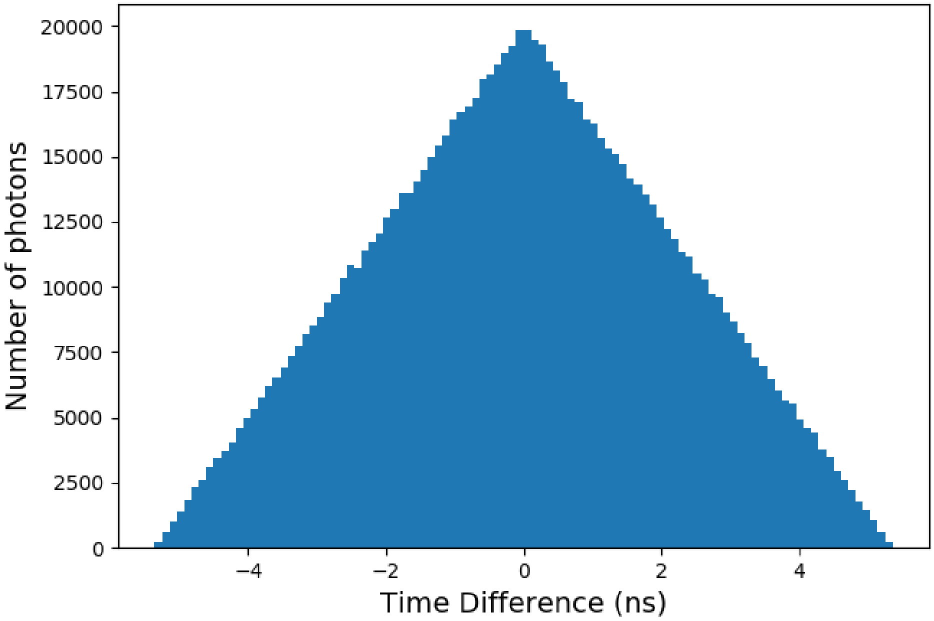

Figure 1.7: Histogram of time differences for N = 10^5 independent correlated pairs of photons arriving onto a mirror described by the geometry in Figure 1.6.

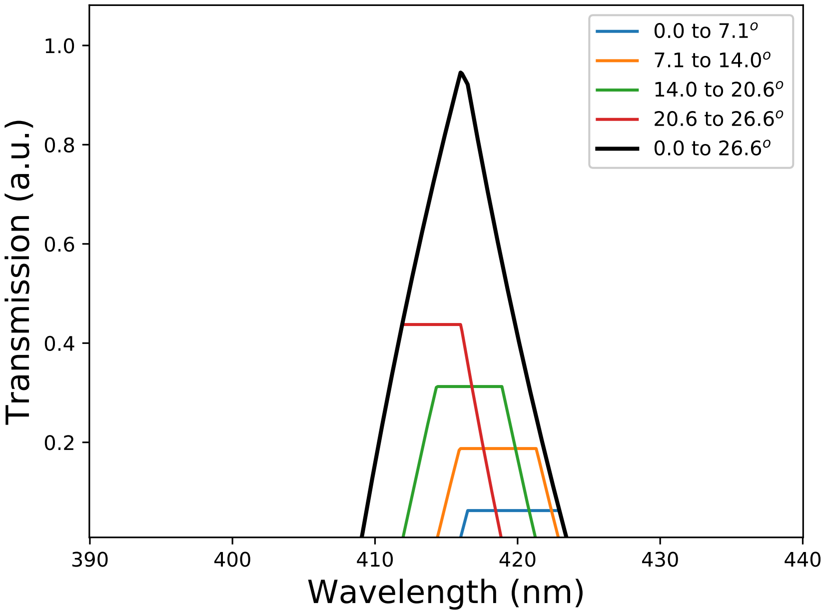

Figure 1.8: Simulation of the filter transmission for uncollimated light from a f/1.0 optical system through a interferometric filter with $\lambda_0 = 420\,\text{nm}$, $\Delta\lambda = 7\,\text{nm}$, and $n_{eff} = 2.38$. (matching the SEMROCK 420/5 filter vendor specifications which is currently used in the VERITAS observations). The black line shows the overall transmission when averaged over the entire mirror area, where each colored line shows the transmission due to different annuli of the mirror in units of the subtended angle.

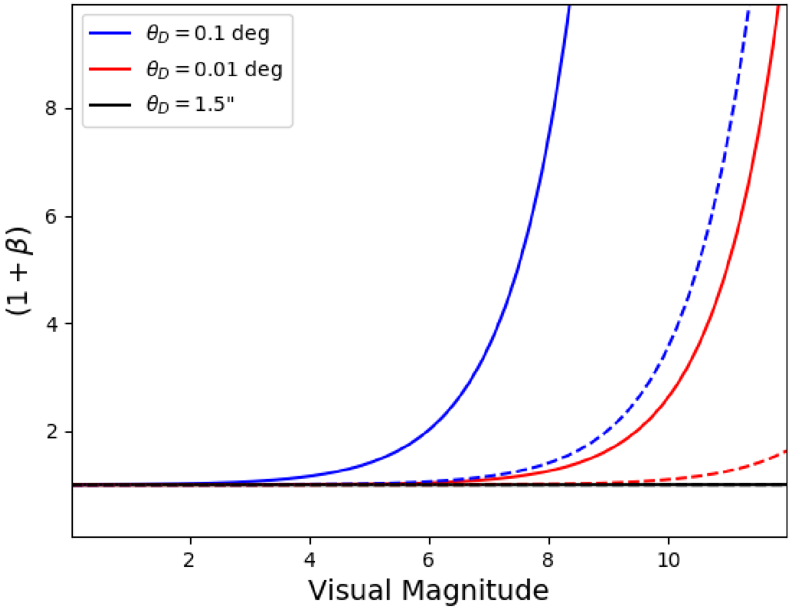

Figure 1.9: Simulation of the effect of a finite angular PSF for bright and dark night sky background conditions represented by the solid and dashed lines, respectively.

CHAPTER 2

SCIENCE APPLICATIONS FOR A MODERN SII OBSERVATORY

2.1 Signal to noise considerations

To first-order, the signal to noise ratio (SNR) for $|\gamma|^2$ in the case of a two-telescope interferometer for unpolarized light is given by (Hanbury Brown, 1974)

$$SNR = A\alpha n|\gamma|^2\sqrt{\Delta f T/2}, \tag{2.1}$$

where A is light collection area, α is the instrumental throughput, n is the photon spectral density, $|\gamma|^2$ is the squared spatial degree of cohrence, Δf is the electronic bandwidth, and T is the total integration time. An empirical form of the expected SNR for the NSII in the case of an unresolved source ($|\gamma|^2 = 1$) was shown by Hanbury Brown (1974) as roughly,[1]

$$SNR = 0.4T^{1/2}10^{-0.4B} \tag{2.2}$$

where B is the blue band magnitude for the star. From this, the corresponding time needed to obtain a SNR = 20 (5 % in the squared visibility) is $\sim$69 hours for B = 2.5. The NSII was ultimately limited for stars brighter than this magnitude. To obtain the same SNR for $B = 3.5$ would have required $\sim$431 hours of observations illustrating why dimmer stars were not pursued with the NSII.

Consider now an idealistic expectation of what can be achieved with a current interferometer using VERITAS as an example. The VERITAS mirrors correspond to an area of $A \sim 113$ m^2 neglecting any shadowing from the camera. Modern photomultiplier tube detectors can achieve quantum efficiencies of $\sim$ 35 %, and assuming an optical throughput of 50 % the overall efficiency is $\alpha \sim 0.18$. For an electronic bandwidth $\Delta f \sim 250$ MHz,

---

[1] The expression found in Hanbury Brown's book (Section 11.12) derives an expression that is $SNR = 0.53\,T^{1/2}10^{-0.4B}$ based on experimental parameters. Data from observations of stars found the actual scaling to be roughly three-quarters of this, and thus resulting in the scaling of 0.4 shown in Equation 2.2.

limited by the optical time dispersion described in Section 1.4.1, the expected scaling is now

$$SNR = 21.4T^{1/2}10^{-0.4B} \tag{2.3}$$

where the photon spectral density for a zeroth magnitude star in the B band is assumed to be $0.95 \times 10^{-4}\,\mathrm{ph\,m^{-2}\,s^{-1}\,Hz^{-1}}$ as done by Hanbury Brown. This corresponds to an improvement of the signal to noise by a factor of approximately 53 over the NSII. Under the same criterion for the limiting magnitude (T= 70 hours, SNR = 20), the corresponding limiting magnitude is then $B < 6.8$. However, the value obtained here does not take into account many parameters that would degrade the sensitivity. These include NSB light, excess noise in the photomultiplier tubes, influence of spurious correlations, and attenuation of light in the atmosphere. Beyond measuring dimmer targets, the squared visibility for bright targets can be measured with a high degree of precision. For example, with the scaling in Equation 2.3, the squared visibility of a partially resolved star $|\gamma|^2 = 0.5$ of magnitude $B = 2.0$ for a one hour integration time can be measured with a SNR of ~ 204 corresponding to an uncertainty of $\sim 1\%$ in $|\gamma|^2$.

While the sensitivity of a modern instrument clearly exceeds that of the NSII, it is important to also compare to the current capabilities of modern observatories that utilize direct interferometery. Some example limiting magnitudes are $m < 6 - 7$ for the NPOI/CLASSIC instrument (Armstrong et al., 2013), $m < 7$ for CHARA/PAVO (Ireland et al., 2008), $m < 6.5$ for CHARA/VEGA (Mourard et al., 2012), $m < 8$ for CHARA/MIRC-X (Anugu et al., 2020), and $m < 6$ for CHARA/CLIMB (Ten Brummelaar et al., 2013). The expected theoretical limiting magnitude of an SII observatory is thus comparable to that of current direct interferometers, particularly in the visible band, and therefore can provide independent high-angular resolution measurements.

Beyond the limiting magnitude, there are several arguments towards a modern intensity interferometer. These generally stem from the robustness of SII against path length fluctuations. The fastest detectors commercially available have temporal resolutions on the order of tens of picoseconds corresponding to a light travel distance of order a few centimeters. In the case of photomultiplier tubes typically used on IACTs, the resolution is of order 1 ns, corresponding to a light travel distance of 30 cm. Atmospheric fluctuations occur over a smaller length scale than these light travel distances and thus SII is insensitive to them.

This provides the capability to operate at large baselines and at all optical wavelengths. Direct interferometers require a mechanical precision at a fraction of a wavelength, and this makes it challenging to operate at short optical wavelengths. Furthermore, since only digital electronic connections are needed to perform intensity correlations, it is relatively straightforward to scale an SII system onto tens, if not hundreds, of telescopes to provide hundreds to thousands of simultaneous baselines. This provides extremely dense coverage of the (u,v)-plane required for studying noncircularly symmetric sources such as binaries or rapid rotators. The baselines can be made arbitrarily large, up to distances where the coherence signal is too weak to measure. These factors therefore allow for a unique complement to existing observatories to assist and advance ongoing scientific programs.

2.2 Angular diameters

One of the most fundamental measurements in optical interferometry is of the angular diameter of stars. Since distances to a large population of Galactic stars are now available, thanks to extensive surveys such as Gaia (Gaia Collaboration et al., 2018), measurement of the angular diameters lead to the physical or “linear” diameters. Direct angular diameter measurements can be used to obtain the effective temperature of the star via the Stefan-Boltzmann law, provided that the bolometric flux can be measured independently (Hanbury Brown et al., 1974b). Effective temperatures estimated from angular diameter measurements can then be tested against stellar models obtained through spectroscopic data. These comparisons allow for calibration of large-scale spectroscopic surveys and tests of atmospheric stellar models (Mann et al., 2015; Casagrande et al., 2014). To interestingly constrain stellar models a measurement precision of better than $\sim 3\%$ in the angular stellar diameter is required (Torres et al., 2010).

Figure 2.1 shows the limb-darkened angular diameter of stars as a function of the visual magnitude for a variety of spectral types obtained from the JSDC spectral catalog (Bourges et al., 2017), which estimates of stellar angular diameters from indirect spectroscopic measurements and, to a lesser degree, direct measurements. The distribution of angular stellar diameters illustrates the requirements for studying stars of different spectra types. For cooler, less massive, stars (e.g., K and M types), a large number can be resolved if a limiting magnitude of $V \sim 10$ can be achieved with relatively modest baseline requirements of $\sim 100\,\mathrm{m}$. However, hotter and more massive stars (e.g., B and A types) require much higher angular resolution capabilities to begin resolving even the brightest of these stars. Current direct interferometers have provided angular diameter surveys for a very large range of spectral types (see van Belle et al. (2019) for a review). Interestingly, it is only fairly recently that these observatories performed measurements of the angular diameter of hotter spectral type (i.e., O or B types) stars with a precision matching what was achieved with the NSII. Notably, these recent angular diameter measurements include surveys of 12 early-type stars (Maestro et al., 2013), 6 O-type stars (Gordon et al., 2018), and 25 B-type stars (Gordon et al., 2019) with an average uncertainty in the measured angular diameters of 2.3%, 7.6%[2], and 6%, respectively.

2.3 Emission line and rapidly rotating stars

Emission line stars are generally identified by Balmer emission (e.g., Hα, Hβ) in their spectra indicating the presence of dense circumstellar material, in the form of a shell and/or disk, that is excited by the stellar radiation. On a larger scale, these stars are a significant source of UV photons driving the formation of HII regions and affecting evolution of the local interstellar medium. They include the subgroups such as 'Be' and Wolf-Rayet stellar types. These stars often display dynamic behaviour and show intensity variations occurring on timescales from minutes to years and radiate over radio to X-ray wavelengths making them interesting observational targets for many astronomers. The mechanisms that drive these systems are not fully understood. Although a significant percentage ($\sim 20\%$) of B-type stars display Be behaviour, the link between them is still debated. In some cases, the circumstellar environments are formed from the stellar mass outflows ('classical' Be Stars), or those that are generated from the accretion of surrounding material (Herbig Ae/Be types). In classical Be stars, the mass outflows are linked to a combination of rapid rotation and intense stellar radiation; however, the rotation rate required for the mass transfer, and exact angular-momentum/mass input interactions with the disk remain unclear (Granada et al., 2013).

High angular resolution observations at the mas and submas level have advanced our

---

[2] Since the angular diameters precision was not stated explicitly in the paper, this was calculated from the tabulated results.

understanding of these objects. Interferometric observations within Hα and Brγ lines probe the spatial distribution of the circumstellar material. Current direct interferometers have recently been used to examine the kinematics of the disk surrounding these stars (Kraus et al., 2012) and to identify nonaxially symmetric spiral density structures present in the disks through multiepoch observations in the blue and red shifted parts of emission line features (so-called V/R variability) (Schaefer et al., 2010). The inclination angle of the disks can be independently obtained by the structure of the observed distribution, and it has been used to calibrate models of Hα line profiles that estimate the inclination from spectroscopic methods (Sigut et al., 2020).

Given the rich history of observations of Be stars in optical interferometry, it is important to identify how SII observations can improve or aid in current observations. A study has shown the capabilities of a CTA-like observatory to perform imaging of the surfaces of rapidly rotating stars, indicating the realistic potential to constrain stellar oblateness and temperature gradients along the stellar surface (Nuñez and Domiciano de Souza, 2015). Observations at short wavelengths provide a unique insight in the probing the stellar surface, since the emission in the disk is presumably weak at these wavelengths.

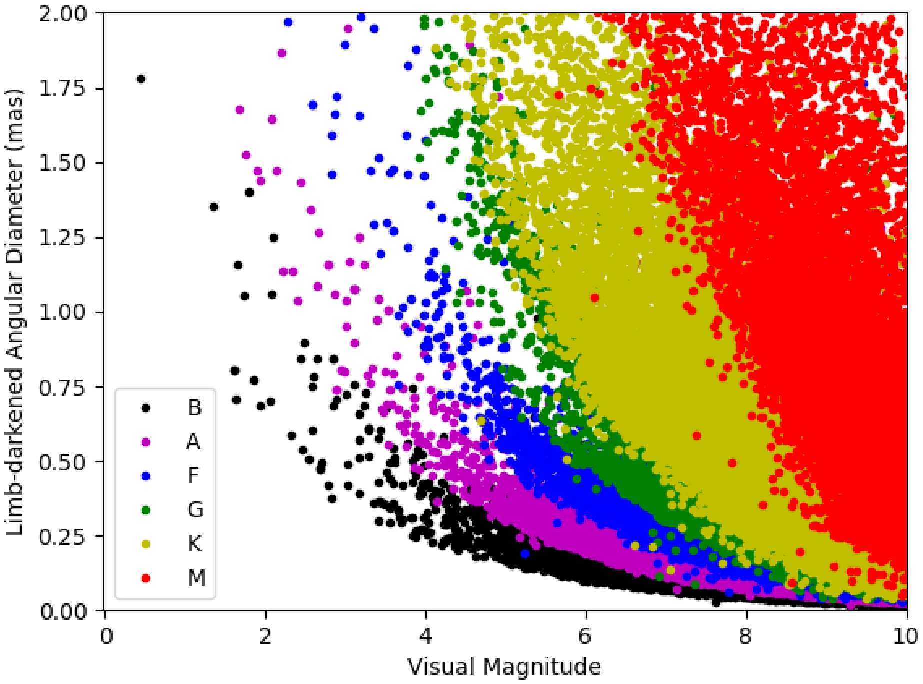

Figure 2.1: Relationship of stellar angular diameters with magnitude for various stellar spectral types. Sources were obtained from the JSDC stellar diameter catalog cross-matched with the SIMBAD database.

CHAPTER 3

COHERENCE MEASUREMENTS OF A PSUEDO-THERMAL SOURCE

Before attempting SII observations on stellar sources with modern observatories, it is extremely helpful, if not necessary, to characterize the sensitivity levels of the instruments in the laboratory by performing similar tests. Measuring the spatial coherence of thermal light is made very difficult as the coherence time is typically several orders of magnitude shorter than the detector resolution time. Even in the laboratory thermal HBT measurements can be difficult to achieve; however, it is straightforward to generate a pseudo-thermal light source that exhibits coherence times much longer, on the order of ms, that allows for much shorter integration times for high SNR measurements. Pseudo-thermal sources allow one to properly characterize the laboratory setup, including parameters such as the source geometry, and also assess sources of systematic noise. The following chapter documents experiments that were conducted in order to demonstrate the working principles of an SII observatory.

3.1 Experimental setup

The laboratory was setup as shown in Figure 3.1. Psuedo-thermal light was generated by shining a HeNe laser (543 nm) onto a rotating piece of ground glass. The scattered light from the glass was then masked by either a single or double pinhole of various dimensions. After propagating down an enclosed box of approximately 3 meters, the light was divided by a 50/50 beam splitter and subsequently detected by single photon avalanche diode (SPAD) detectors (MPC-PDM Series, 100 μm active area). The output SPAD signal was then passed to an analog-to-digital converter (NI 5781) that passed the ADC values to an FPGA based (NI PXIe-7965R) threshold discriminator written in LabVIEW. The FPGA allowed for integrating the detector counts over a controllable time window and streamed the photon counts to disk. The correlation of the two signals is performed via software to retrieve the correlation over a range of time-lags as to resolve the temporal coherence of the light source.

3.2 Photon counter and correlator

When a photon is detected, the SPAD detector outputs a TTL pulse of width 20 ns with rise/fall times of about 2 ns. The ADC converter digitized the output SPAD signal at a rate of 100 MHz, or every 10 ns, to ensure detection of every photo-electron. A discriminator using an FPGA was developed to register the detection of a photon, and double counting was accounted for when the digitized voltage was greater than the discriminator level for two serial samples. The SPAD detector has a characteristic dead-time of 75 ns corresponding to a maximum count rate of about 13 MHz above which the detector response is saturated. Neutral density filters were placed in the laser path to reduce the photon flux such that the count rate for each detector was less than 1 MHz. For a photon detection rate of 1 MHz that follows a Poisson distribution, the probability that 2 or more photons arrive within an interval of width of the dead-time is less than 3 %. The number of photons every microsecond was then recorded to disk for off-line processing.

The cross-correlation and auto-correlation for the detectors was performed via software on the stored data. To implement this, the LabVIEW cross-correlation virtual instrument from the Multi-core Analysis and Sparse Matrix toolkit was used, which calculated the cross and auto-correlations over a range of time lags several times that of the coherence time.

3.3 Visibility models for the laboratory sources

The sources used in the lab consist of either a single or double pinhole as to mimic the observation of single or binary stellar sources. The single pinholes are modeled as a uniform disk with a finite angular diameter, θ_P. The expected visibility then follows an Airy disk profile,

$$V(u,v) = 2\frac{J_1(\pi\theta_P B_r(u,v))}{\pi\theta_P B_r(u,v)} \tag{3.1}$$

where J_1 is the Bessel function of the first kind, and B is the radial separation between detectors, $B = \sqrt{B_x^2 + B_y^2}$, and as expressed in the commonly used uv coordinates, $B_x = u\lambda, B_y = v\lambda$ such that $B = \lambda\sqrt{u^2 + v^2}$.

In the case of the binary, or double pinhole light source, the source intensity distribution is modeled as two uniform disks with finite angular diameters with flux ratio f. It can be shown (Berger and Segransan, 2007) that the visibility under these assumption can be written as

$$|V(u,v)|^2 = \frac{V_1^2 + f^2 V_2^2 + 2f V_1 V_2 cos(\frac{2\pi}{\lambda}\boldsymbol{B} \cdot \boldsymbol{p})}{(1+f)^2} \tag{3.2}$$

where V_1 and V_2 are the respective visibilities of each of the sources, which in this case follow the form of Equation 3.1. The quantity $\boldsymbol{B}$ is the baseline vector and $\boldsymbol{p}$ is the separation vector between the two pinhole centers. From the dot product it can be seen that when the baseline vector is varied parallel to the separation vector, the modulation in the observed visibility from the binary separation can be observed.

3.4 Measurements of the temporal and spatial coherence

Using the experimental setup described in the prior sections, a series of temporal and spatial coherence were performed for a variety of pinhole configurations. Figure 3.2 shows measurements of the auto- and cross-correlations for short and large baseline on a single pinhole configuration. We see that the auto-correlation for a given channel is relatively unchanged for a given baseline separation, but the cross-correlation is reduced significantly for large baseline separations. The temporal variation can be explained by a time-varying speckle pattern (Martienssen and Spiller, 1964). When the detector separations are well within the size of a given speckle, given approximately by λ/θ, the intensities are highly correlated, but as the the separation approaches and exceeds the speckle size, the relative intensity fluctuations become uncorrelated.

The spatial coherence was then measured by measuring correlations over a range of detector separations. One of the detectors was mounted onto a linear actuator to allow control the separation of the detectors. The actuator movement was automated using a LabVIEW script and integrated into the data acquisition code to allow for efficient measurements over a large number of baselines. Two single pinholes of different sizes (vendor specified diameter of 200 and 300 μm) were measured, and the results are shown in Figure 3.3. Each of the measurements were fit to a uniform disk model where the zero-baseline, disk diameter, and normalization were left as free parameters. A clear difference between the measured coherence length of the single pinhole sources were seen, and both are well-approximated by uniform disk sources.

Additionally, three different binary system configurations were also tested, where the results are shown in Figure 3.4. The orientation of the binary was set such that the separation vector of the pinholes was parallel to that of the detector separation. The differences between each of the different configurations are most evident in the second and third lobes. The data for each source were fit to a binary model described by Equation 3.2. The pinholes were approximated as uniform-disks to determine V_1 and V_2, and the angular diameters, angular separation, and flux ratio were left as free parameters. The results of the fits are shown in Table 3.1. The results of the fits show the qualitative expectation of increasing diameters from the 200/200, 200/300, and 300/300 configurations. The fit diameters generally underestimate the vendor-specified values. This is attributed to two factors. First, the distribution of light onto the pinholes is not uniform, as clearly indicated by the unequal flux ratio values. Furthermore, the distribution will follow the spatial profile of the laser beam, and thus each pinhole deviates from a uniform-disk approximation. Additionally, the pinholes were examined under an electron scanning microscope, and the resulting images showed contamination at the edges of the pinhole further distorting the light intensity across the pinhole. The physical separations of the pinholes also systematically under approximate the vendor-specified separations by a constant factor and is also is attributed to the spatial distribution of the light on the pinholes. When factoring in the under estimated diameters, the separations are consistent with the expected separations. However, the overall results are satisfactory, which clearly indicate the binary nature of the pinholes. The fit diameters and separations correlate closely with the expected values.

Table 3.1: Fit results corresponding to the model lines shown in Figure 3.4

	θ_1 (μm)	θ_2 (μm)	p (μm)	f
200/200	155 ± 4	148 ± 10	445 ± 2	0.27 ± 0.01
200/300	171 ± 5	240 ± 10	461 ± 2	0.61 ± 0.03
300/300	262 ± 10	283 ± 22	498 ± 4	0.53 ± 0.03

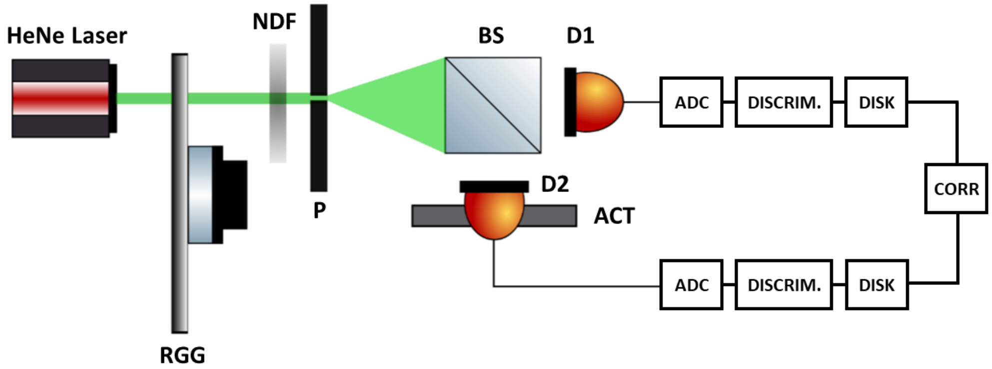

Figure 3.1: Basic schematic of Schematic of laboratory setup for correlation measurements of psuedo-thermal light. In this setup, HeNe laser light is scattered by a piece of rotating ground glass (RGG). The light moves through a neutral density filter (NDF), and spatial mask (P) to generate the articial source. A standard beamsplitter (BS) divides the light into two beams, and each beam is measured by two separated detectors (D1/D2). One of the detectors is mounted onto a linear actuator (ACT) to vary the detector separation. The detector signals are passed to a digitizer (ADC) unit and a FPGA programmed discriminator (DISCRIM) allows for photon-counting over variable time windows. The signal is stored to a hard disk (DISK), and then the correlations between the strems are processed off-line using standard computer processors (CORR).

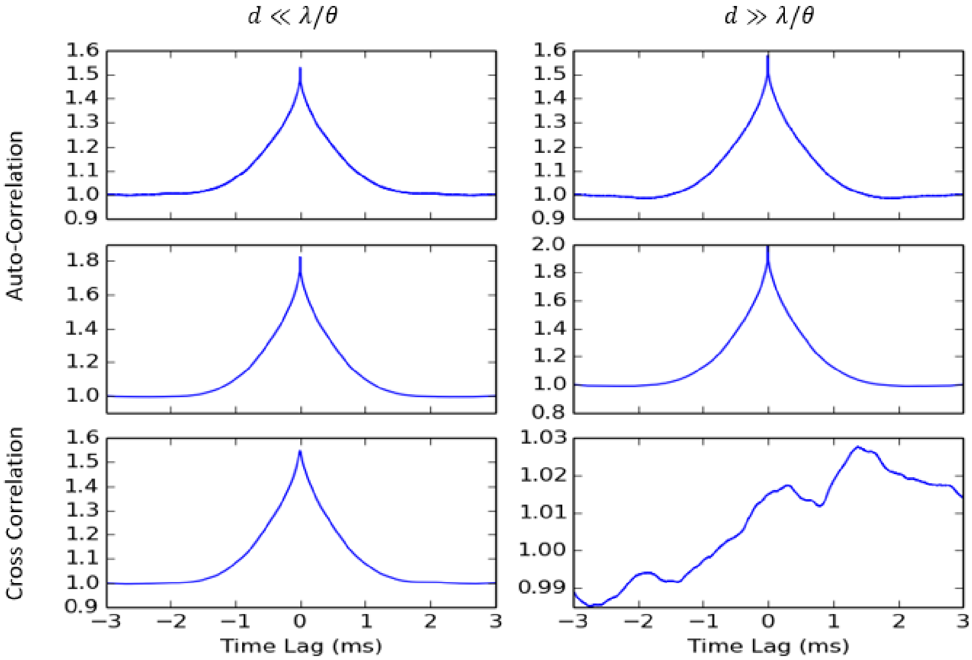

Figure 3.2: The two columns represent measurements performed for small (left) and large (right) baseline separation distances, where the coherence from the source is, respectively, maximal and negligible. The top two rows represent the auto-correlation for each channel and the bottom row is the cross-correlation between different detectors.

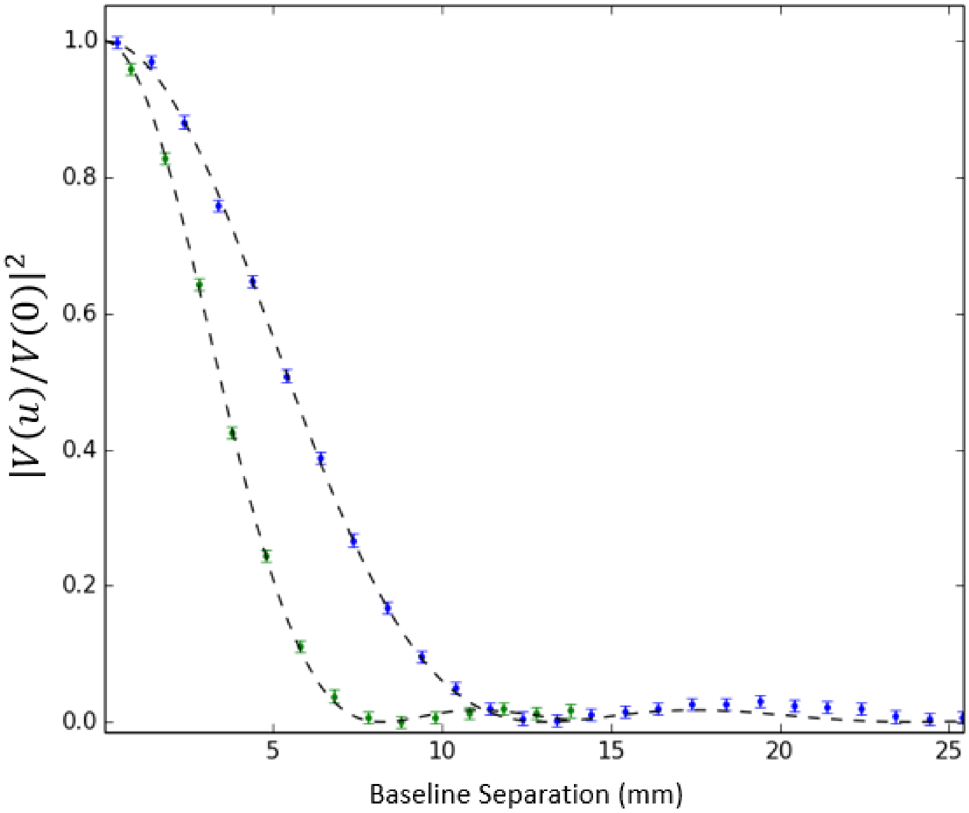

Figure 3.3: Measurements of single pinhole psuedo thermal sources in the laboratory. A clear difference in the extent of the correlation length is observed for sources of different sizes.

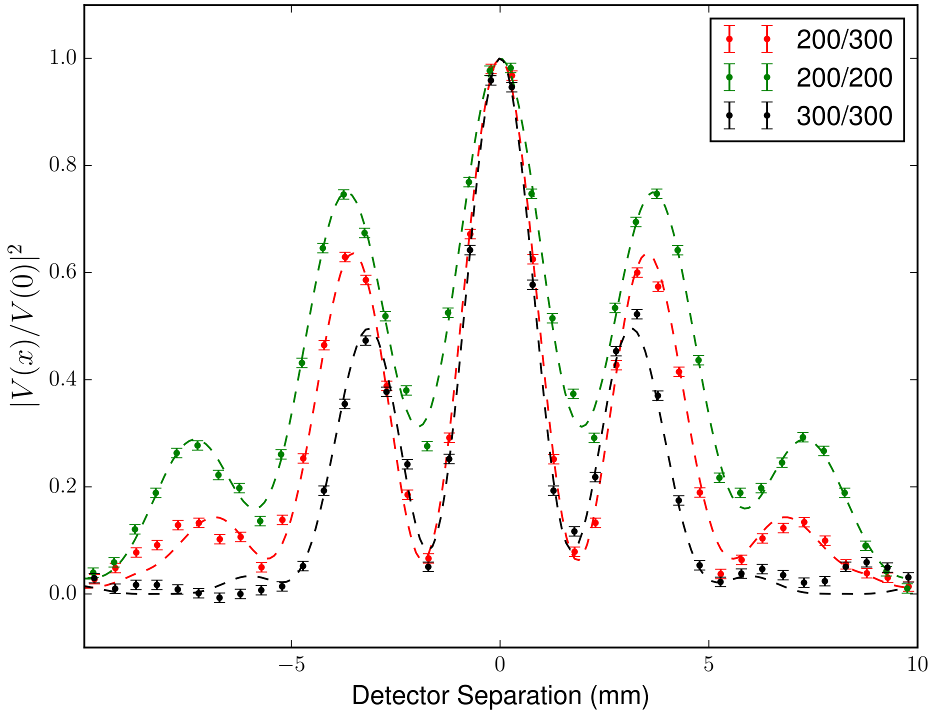

Figure 3.4: The above plot shows measurements of squared visibility as function of the baseline, or detector separation, for various configurations of binary sources. The dotted line represents a theoretical fit to the data, and the error bars on each data point represent the measurement uncertainty, which does not include systematic effects. Each curve is normalized by the value of the squared visibility for the zero baseline position that is provided by the fit.

CHAPTER 4

COHERENCE MEASUREMENTS OF A THERMAL SOURCE

In the laboratory, we present new techniques for measuring the spatial coherence of a laboratory thermal source using high-speed photo-detectors and digital electronics. The modular nature of the detector and data acquisition system allows for straightforward integration with existing observatories. Parallel polarizations clearly demonstrate a photon bunching in time and space, whereas orthogonal polarizations eliminates coherence but reveals any additional correlation due to noise contamination. We show that correlation measurements in the orthogonal configuration, or when the detectors are separated at distances greater than the spatial coherence length of the source, can be used to correct for systematic noise due to spurious electronic correlations.

4.1 Experimental setup

A diagram of our laboratory system is shown in Figure 4.1. Light from a mercury arc-lamp is collimated, passed through a 10 nm narrow-band filter centered on the 435.8 nm G spectral line of the Hg arc-lamp, and then refocused onto a spatial mask. The mask is either a single or double pinhole of various size configurations (typ. 200 - 300 micron diameter) simulating single and binary star systems. The output light passes through a long box (3 m) and is split into two secondary beams via a 50/50 non polarizing beam splitter. The light from each beam is then detected by super bi-alkali ($> 35\%$ Q.E.) high-speed photo-multiplier tubes (PMT). The PMTs used in the laboratory are the same as those currently employed on the cameras of an IACT observatory, VERITAS (Otte, 2011). The light collecting areas of the detectors are limited by a circular aperture of 5 mm diameter. It is noted that the PMT aperture is of comparable size to the spatial coherence length of the source. This is done to increase the amount of light throughput into the detector such that the necessary integration time needed to reach a desired sensitivity level is reduced.

The effects of large detector areas have already been described in other work (Rou et al., 2013) and are taken into account here. The PMTs are also enclosed in a brass tube to shield them from unwanted electro-magnetic radiation. Linear optical polarizers may be placed in front of each PMT and can be individually rotated to select parallel or orthogonal polarization between the detectors.

In order to sample different regions of the spatial coherence curve, one of the PMTs is mounted on a RoboCylinder linear actuator, whose position is controlled via LabVIEW software to high accuracy. The positioning is integrated into our data acquisition system allowing for automated measurements at varying positions. The output cables from the PMTs are fed into a low noise high-speed ($>$ 200 MHz) FEMTO trans-impedance preamplifier. The resulting signal is sent through 10 ft of double shielded cable (RG-223) and then continuously digitized by an analog-to-digital converter (ADC) at a rate of 250 MS/s using an AC-coupled National Instruments (NI) FlexRIO adapter module (NI-5761).

We have successfully employed two different types of digital correlators, off-line and real-time. In the off-line correlator, the digitized data from each channel are scaled, truncated to 8-bits, and merged into a single continuous data stream by a Virtex-5 FPGA (PXIe7965R). The data stream is then recorded to a high speed (700 MB/s) 12TB RAID disk. A software routine using LabVIEW can later be used to retrieve intensity correlations between channels as a function of the digital time lag, typically up to $\pm$ 1 μs in steps of 4 ns. Due to the large number of samples, the data are read in blocks of 512 samples. The convolution theorem gives the correlation between two signals as the inverse Fourier transform of the product of the Fourier transforms of the signals. This is implemented by use of the NI Multi-core Analysis and Sparse Matrix toolkit (MASM) cross-correlation virtual instrument (VI), which optimizes the computation by utilizing separate computing cores.

The largest drawback of performing the correlation off-line is the computation time needed to analyze the data. Data are read into a buffer using a single computing core and then correlated using the remaining cores. Depending on the number of samples in each data block, it takes on the order of an hour of computation time for every minute of data recorded. This is mainly due to the time required to perform the correlation via the Fourier method for each data block in the NI cross-correlation VI. Since the correlation can be easily parallelized, this could be remedied by using a super-computer with many (>1000) processing cores. The NI controller used has only 4 cores, limiting the maximum number of correlations performed at the same time.

Some of the results presented herein were obtained by use of a real-time correlator using the Virtex-5 FPGA. In this implementation, the cross-correlation is computed using a multiply-accumulate algorithm with delay nodes to retrieve the correlation at various time lags with the FPGA clock set at 125 MHz. The standard deviation of the entire correlogram excluding the zero time-delay bin is recorded, and the time-stream of both channels are displayed on the LabVIEW front panel interface to allow visual inspection of the data. The FPGA clock for the algorithm is limited to 125 MHz. This timing restriction reduces the signal to noise ratio (SNR) by a factor of $\sqrt{2}$ in comparison to the off-line correlation. However, the correlations are retrieved in real-time, allowing for immediate inspection of results and iterative tests of the laboratory setup. In the future, a compromise between the off-line and FPGA methods can be achieved by first streaming the data to disk and then using the FPGA to perform the correlations on stored data.

4.2 Observables and data reduction

4.2.1 Review of II measurements

The correlation between AC-coupled amplified voltage signals, $J_1(t)$ and $J_2(t)$, from separated photo-detectors is

$$c(\tau) = \frac{1}{T_0} \int_0^{T_0} J_1(t-\tau) J_2(t) dt \tag{4.1}$$

where T_0 is the total integration time of the correlator, and τ is the time delay between channels. Hanbury-Brown and Twiss showed (Hanbury Brown and Twiss, 1958b) that the correlation $\overline{c(0)}$ for a linearly polarized partially-coherent source of finite angular size could be written as

$$\overline{c(0)} = 2e^2 A_1 A_2 \int_0^\infty |\Gamma(\nu, d)|^2 \, \alpha^2(\nu) \, n^2(\nu) d\nu \int_0^\infty |F(f)|^2 df \tag{4.2}$$

where A_1 and A_2 are the light collection areas for each detector, α is the quantum efficiency, assumed to be the same for both channels, and n is the spectral density of the source in units of photons sec^{-1} Hz^{-1} m^{-2}. Γ is the coherence factor expected from the source and is dependent on the detector separation d. The term $F(f)$ represents the frequency response of the detectors and amplifiers. The optical bandwidth of the light, $\Delta\nu$ as set by filters in the optical system, is generally narrow enough that the quantum efficiency, spectral density, and coherence can be assumed as constant over the optical bandwidth. Additionally, for a rectangular bandpass the integral over the frequency response can be re-written as $\int_0^\infty |F(f)|^2 df = |F_{max}|^2\,\Delta f$, where $|F_{max}|$ is the effective gain in a single channel (assuming identical channels), and Δf is the electronic bandwidth of the correlator assuming that the gain is approximately constant over the electronic bandwidth. The correlation then becomes

$$\bar{c}(0) = 2e^2 A_1 A_2 \alpha^2 n^2 |F_{max}|^2 \Delta\nu \Delta f |\Gamma(d)|^2. \tag{4.3}$$

The ability to detect the coherence of the source is limited due to shot noise fluctuations in each channel. Hanbury-Brown and Twiss showed that for identical channels the root mean square fluctuations in the correlator output due to shot noise is

$$\sigma = \sqrt{2}e^2 \alpha n \Delta\nu (A_1 A_2)^{\frac{1}{2}} |F_{max}|^2 (\frac{\Delta f}{T_0})^{\frac{1}{2}}. \tag{4.4}$$

To find the signal to noise ratio (SNR) we divide Equation 4.3 by Equation 4.4 retrieving

$$SNR = \sqrt{2}(A_1 A_2)^{\frac{1}{2}}\, \alpha\, n\, |\Gamma(d)|^2 \sqrt{\Delta f T_0}. \tag{4.5}$$

The above equation represents an idealistic form of the SNR. In this derivation, we assume point-like detectors that exhibit no dark current or after-pulsing. Furthermore, the above SNR does not include the contribution from stray light entering the detector, losses in the correlator, or pickup of additional noise in the data acquisition system. More complete treatments that include many of these additional considerations have already been performed (Hanbury Brown and Twiss, 1957, 1958b; Rou et al., 2013).

In our experiment, we digitize the voltage such that time is discretized, $J(t) \rightarrow J(t_i)$, making the observed ADC reading

$$K(t_i) = [\frac{2^{n_b}}{V_r} J(t_i)] \tag{4.6}$$

where [ ] represents rounding the value to the nearest integer, V_r is the voltage range of the digitizer, and n_b is the number of resolution bits. The observed digital correlation is then,

$$c(t_k) = \frac{1}{T_0} \sum_{i=0}^{N} K_1(t_i - t_k) K_2(t_i) \Delta t \tag{4.7}$$

where t_k is the discrete digital time delay, and Δt is the sampling time of the ADC.

4.2.2 Correlated noise reduction - ON/OFF analysis

When operating at the large bandwidths required by an intensity interferometry system, there is often the undesired influence of spurious correlated noise degrading the spatial coherence measurement for a given source. Noise sources are varied, from electronic cross-talk between channels in the recording system, to Cherenkov light in the atmosphere due to gamma-rays when observing stars. In the laboratory, a persistent noise source is attributed to radio-frequency (RF) pickup. This RF signal is simultaneously detected in both electronic channels producing correlated noise. Regardless of the source, if the unwanted correlated noise is stable on operational timescales, it can then be measured and removed. The exact behavior of each noise source on the correlated signal must be examined in a case-by-case basis. In this section, a general way to identify and reduce correlated noise by subtraction is presented. In our application, the temporal behavior of the correlated signal, or correllogram, is monitored over small time-lag windows ($< 1\,\mu s$), throughout the integration process. In the laboratory total integration times are on the order of 5 - 20 minutes but will be greater than one hour when observing stellar sources with telescopes.

The measured correlation as a function of the time delay is

$$c(\tau) = \langle K_1(t) K_2(t + \tau) \rangle.$$

Typically, the sampling time of the digitizer is much longer than the coherence time of the light. In this case, the correlation attributed to the spatial coherence of the source will only appear for the zero time-lag bin, $\tau = 0$. For time-lags not equal to zero, the correlation should be distributed randomly according to shot noise from photo-detection.

Additional noise is then written as an additive term to the ADC reading recorded for each channel at the digitizer input,

$$K(t) = S(t) + N(t)$$

where $S(t)$ is the signal attributed to the source, which includes both the wave and shot noise components, and $N(t)$ is the noise introduced into the system. In general, the noise term, $N(t)$, may result from a combination of several noise sources. The resulting correlation is then

$$\begin{aligned} c(\tau) =& \langle S_1(t) S_2(t+\tau)\rangle + \langle N_1(t) N_2(t+\tau)\rangle \\ &+ \langle S_1(t) N_2(t)\rangle + \langle S_2(t+\tau) N_1(t)\rangle \end{aligned}$$

The goal is then to identify and remove all above terms except for the correlation between S_1 and S_2. Now, it is necessary to consider at what stage in the measurement process is the noise introduced into the detection. For purely electronic noise which occurs after photo-detection, the cross-terms between the signal in one channel and noise in another, known as the cross-talk, is ignored. In the laboratory, we observe that the cross-talk between the channels is negligible compared to the signal and noise correlations. The measured correlation can then be written as

$$c(\tau) = \langle S_1(t) S_2(t+\tau)\rangle + \langle N_1(t) N_2(t+\tau)\rangle$$

where only the noise not correlated to the signal itself was kept. The correlated noise appears as a purely additive term to the overall correlation.

To remove the correlated noise, we perform a background measurement of the correlation which does not contain the signal attributed to the spatial coherence, but includes the noise contribution at the same level as in the desired correlation measurement. The final measurement is obtained as the residual between the ON observation, where source coherence is expected, and the OFF observation. A straightforward way to obtain OFF data in the laboratory is to measure the correlation for detector separations large enough for the contribution due to the coherence of the source to be negligible. This makes the observed correlation

$$\begin{aligned} c_F(\tau, T, d) =& \langle S_1(t) S_2(d_{on}, t+\tau)\rangle - \langle S_1(t+T) S_2(d_{off}, t+T+\tau)\rangle \\ &+ \langle N_1(t) N_2(d_{on}, t+\tau)\rangle - \langle N_1(t+T) N_2(d_{off}, t+T+\tau)\rangle \end{aligned}$$

where T is the time difference between recordings of the ON and OFF runs, and d_{on} and d_{off} are the detector separations in the ON and OFF configurations. Given a circular source with angular diameter θ_d, the detector separation for the background correlation must be greater than $1.22\lambda/\theta_d$ so that the coherence from the source is very small. Ideally, the noise sources do not significantly change between ON and OFF runs such that the residual between noise correlations tends to zero, leaving only the difference in signal correlations. In order to alleviate for the slow changes in noise level between ON and OFF observations, we tend to proceed with relatively rapid observation cycles of no more than a few minutes period.

To ensure that the noise subtractions are properly performed, the R.M.S. distribution over the entire correlogram excluding the zero time-lag is monitored against the expected trend of $\frac{1}{\sqrt{T_0}}$, where T_0 is the total integration time. Initially, the shot noise component will dominate the R.M.S, but as the integration of the correlator proceeds, low-level noise correlations may be detected which sets a limit on the minimum detectable R.M.S. When the noise correlation is significant, the R.M.S. trend will deviate from $\frac{1}{\sqrt{T_0}}$. For proper noise subtraction, the residual between the ON and OFF correlations should follow the $\frac{1}{\sqrt{T_0}}$ trend. Figure 4.2 shows a typical result in the laboratory for the R.M.S. trend. An ON and then OFF run of 5 minutes were taken sequentially. The integrated correlation for ON, OFF, and ON-OFF was recorded every second, and the R.M.S. was calculated for each measurement over the entirety of the integration time. The bottom panel displays the R.M.S. multiplied by the $\sqrt{T_0}$ such that the expected value should fluctuate about a constant. For both the ON and OFF runs, it begins to deviate from the expected trend after only 50 seconds of integration (when the noise is detected). However, the residual between the ON and OFF runs appears to be more stable, suggesting that the noise subtraction is being performed properly. Here, the normalization for the R.M.S. trend for ON and OFF runs is different, which we attribute to varying levels in the light intensity and also the noise.

The measurements can also be performed using parallel (ON) and orthogonal polarization (OFF) configurations between the detectors. Light between orthogonal polarizations should show no coherence and thus can be used as a background or OFF observation. This method provides an additional benefit since both parallel and orthogonal configurations can be observed simultaneously for a single detector separation.

4.3 Results

4.3.1 Validation of ON/OFF analysis

The ON/OFF analysis was validated in the laboratory with the experimental setup shown in Figure 4.1 using the off-line correlator and without the use of polarizing filters. Figure 4.3 displays the correlogram both before and after obtaining the residual between ON and OFF runs. The ON region was chosen at zero baseline separation, and the OFF at a separation of 10 mm. Given the expected angular size of the source the first zero of the coherence function is reached at approximately 5.5 mm. The subtraction of spurious noise reveals the coherence of the source at the zero time-lag bin.

4.3.2 Spatial coherence measurement

To measure the spatial coherence a LabVIEW routine was developed which integrated the actuator movement with the data acquisition. The source consisted of a circular pinhole of approximately 300 micron diameter at a distance of 3.15 m with a central wavelength of $\lambda = 435\,\mathrm{nm}$. Correlations were recorded at each position in 5 minute segments for both an ON and subsequent OFF run. A total of 6 ON positions each separated by 1mm were recorded about the zero baseline position. After each 5 minute integration, the mean of the correlogram, excluding the value at the zero time-lag bin, was subtracted from the entire correlogram. The residual between ON and OFF runs was then calculated. This process was repeated 4 times, yielding a total integration time of 20 minutes at each position.

The result of this procedure is shown in Figure 4.4. The uncertainty in each measurement was determined by the RMS scatter for time lags away from zero. The dashed line represents a fit to the data by modeling the source as a uniform disk with fixed wavelength and angular diameter. The zero baseline (or center position) and normalization are left as free parameters and determined by the fit. The solid line includes the effects of the extended detector size (Rou et al., 2013). To include these effects in the fit, an initial model is generated by convolving the detector areas with the expected normalized spatial coherence. The resulting model was interpolated and then fit to the data in a similar manner as the initial fit without the detector size effects.

A reduced χ^2 test was performed between the uniform disk model with detector size effects and the measured spatial correlation finding $\chi^2/\nu = 0.83$, suggesting agreement between the data and model. However, there are several considerations for the source that are not taken into account here. Examination of the pinhole under a scanning electron microscope revealed irregularities in the diameter on the order of 5-10 %. Additionally, the angular brightness distribution may not be constant over the area of the pinhole, making the uniform disk model assumption not fully valid.

4.3.3 Correlation between orthogonal and parallel polarized light

The experiment was setup using the polarizing filters in a parallel configuration in front of each detector. Real-time FPGA correlations for minimal detector separation were recorded for a period of 5 minutes. The filter was manually rotated by 90 degrees to select the orthogonal configuration and the correlation measurement was repeated. The results are shown in Figure 4.5, which shows the correlogram both before and after the application of the ON/OFF subtraction. The noise subtraction between parallel and orthogonal polarizations offered an improvement of 59% of the SNR over the parallel configuration measurements.

4.4 Outlook

The second order coherence function for simulated stars using a thermal light source were measured with a digital correlator. An ON/OFF analysis routine was developed allowing for removal of systematic spurious correlations due to unwanted noise pickup. The routine consisted of either physically separating the detectors so that the coherence from the source is negligible or using orthogonal polarizations in order to measure a background. The main application of this work is towards a modern SII array using IACT arrays to observe stars. The system will be integrated into the StarBase-Utah observatory over the Summer of 2017 for initial tests to verify operation on actual astronomical telescopes.

Our group is actively working to improve some of the features presented in this paper. At the time when these results were obtained, the maximum bandwidth of the FPGA correlator was limited due to timing restrictions. However, a modified algorithm was developed allowing for more optimal operation of the FPGA correlator. Additionally, instead of performing the correlations in real-time, the data can be first streamed to disk, where the correlations are performed after digitization. A benefit of streaming data to disk is that an arbitrary number of channels can be correlated with computation time as the only limitation. This opens the possibility for correlations between selected polarization modes as well as multiple spectral channels. The obtainable SNR is then improved by the square root of the number of additional channels. Also, proper normalization of the correlation between runs for varying light levels has yet to be demonstrated. The true normalization depends on a number of factors, primarily the light intensity and gain variations. Within small integration times in the laboratory, the light intensity and gain can be expected to be constant; however, over hour-long time scales as needed for stellar observations, these changing parameters need to be accounted for. The normalization of the correlation for varying light intensity and gain fluctuations has already been studied by Hanbury-Brown and Twiss (Hanbury Brown, 1974).

For the integration into IACT telescopes there are several tasks to be demonstrated. First, to use the ON/OFF analysis it is necessary to measure the orthogonal and parallel polarization of light simultaneously to remove the lasting effect of any transient noise sources as well as reducing total data collection time. A straightforward implementation of this is to use a polarized beam splitter to separate the orthogonal polarizations. Each telescope will have its own data acquisition hardware with the data brought together to a central processing unit after digitization. This requires synchronization of the ADC modules to sub nanosecond precision, which already can be accomplished using fiber optics and external clocks (Serrano et al., 2009). In the laboratory, we have already achieved synchronization for closely spaced (< 1m) but physically separated data acquisition modules using a central timing unit and coaxial cable connections. However, this capability still needs to be demonstrated over large (> 100m) distances.

We have successfully measured the coherence of a thermal blackbody source in both time and space using a digital correlator. Small modifications to the current experimental setup allow interferometric capabilities on large arrays of IACTs at very modest costs and are currently being pursued.

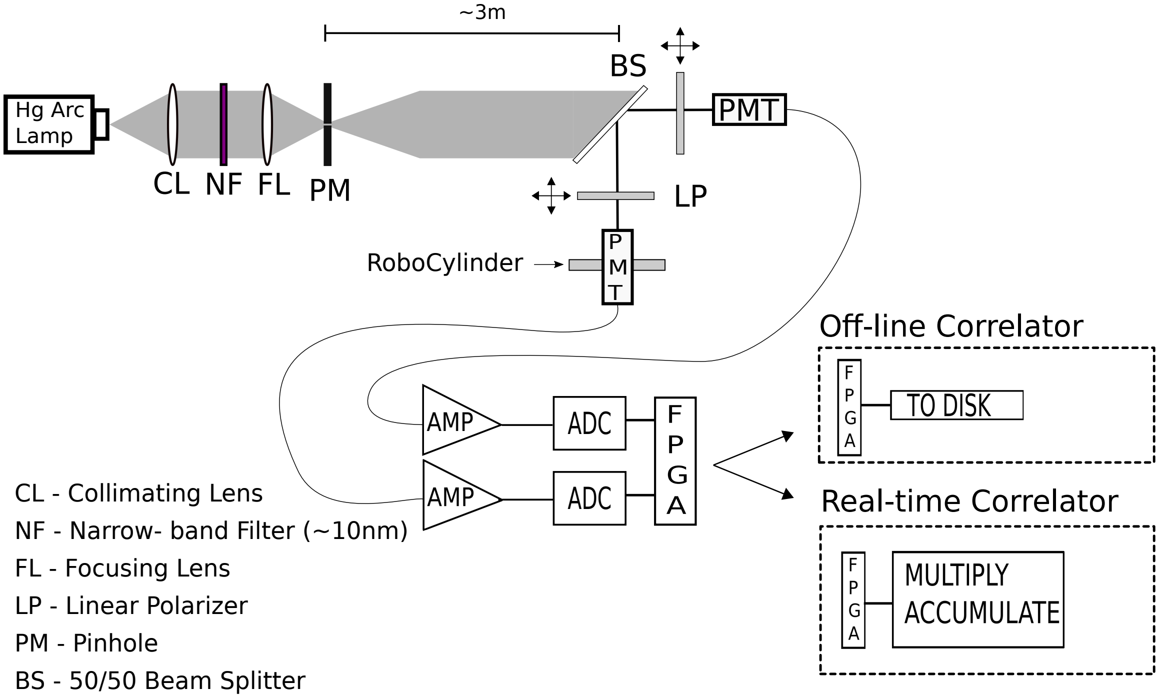

Figure 4.1: Schematic of the laboratory setup

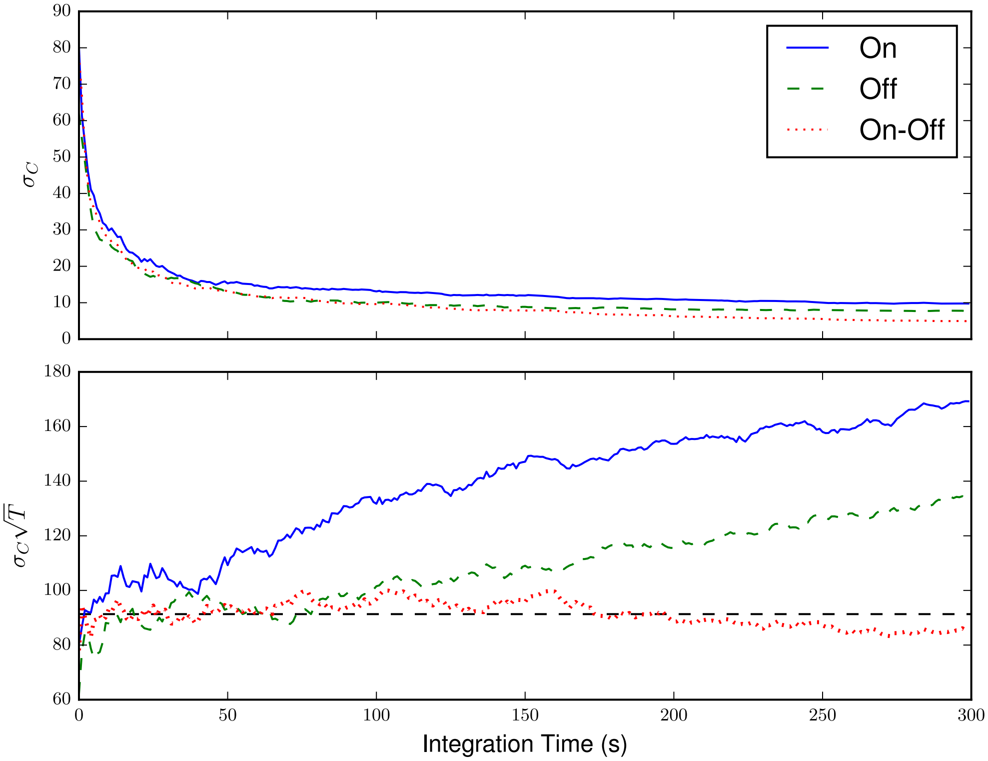

Figure 4.2: The top panel shows the standard deviation of the correllogram excluding the zero time-lag bin as a function of the total integration time. In the bottom panel, the same data are shown but multiplied by $\sqrt{T_0}$. The horizontal black dashed line shows the mean of the ON-OFF analysis. For both the ON and OFF runs, the presence of spurious correlations causes the R.M.S. trend to deviate from the expected $\frac{1}{\sqrt{T_0}}$. In the case of the ON-OFF analysis, the R.M.S. tends to follow the expected trend.

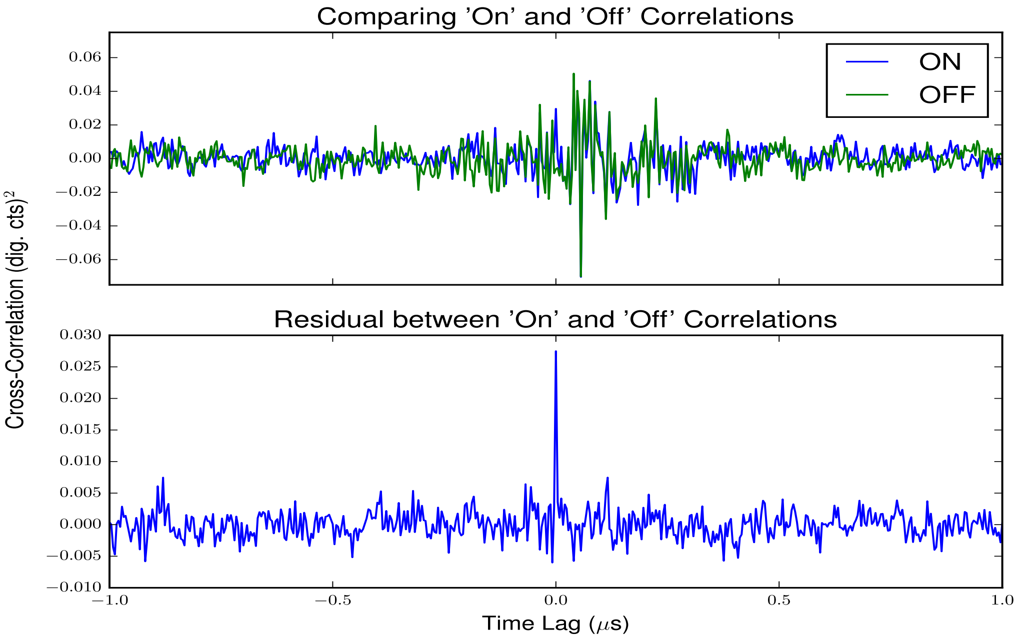

Figure 4.3: In the top panel sequential ON and OFF measurements of the correlogram over an integration time of 30 seconds each are overlaid. For small time lags ($\tau < 500\,\text{ns}$), the scatter between the measured correlation for different time lags increases significantly due to the presence of correlated noise. In the bottom panel, the residual between a total of 10 minutes each of ON and OFF data (comprised of 30 second sequential runs alternating between ON and OFF) is shown, which reveals the zero time-lag correlation emanating from the spatial coherence of the source.

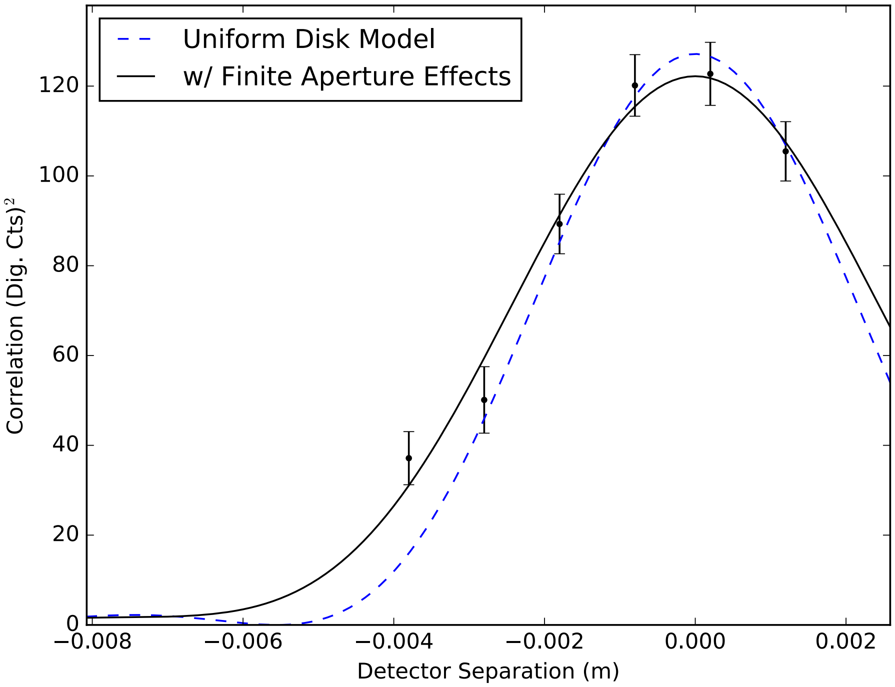

Figure 4.4: The above image shows the measured correlation from the FPGA correlator as a function of the detector separation. The dotted blue line is a fit to the data assuming a uniform disk model for the light source. The wavelength and diameter of the source are held constant but the normalization and center can vary. The black line is a similar fit but includes the effects of the extended detector aperture.

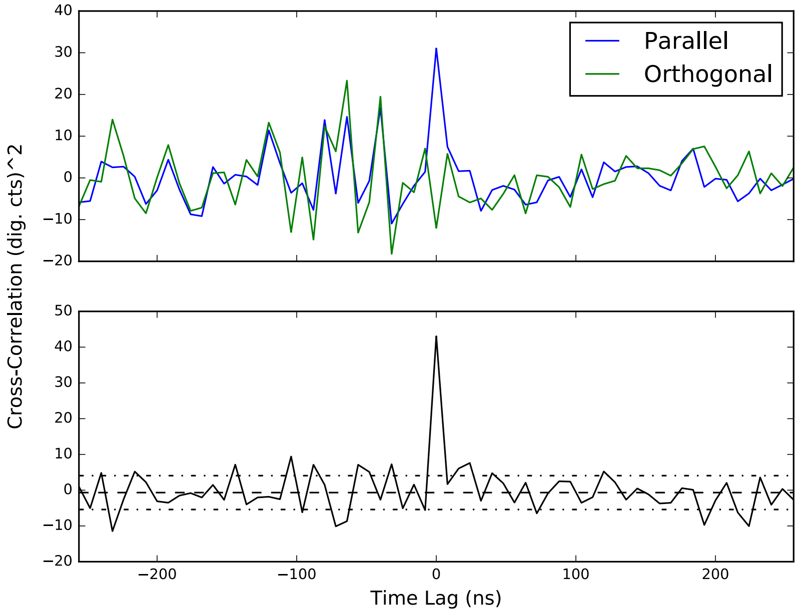

Figure 4.5: Correlogram for the polarization tests performed in the laboratory. The top panel shows the result for both the parallel and orthogonal configuration, and the bottom panel shows the residual along with $\pm 1\sigma$ indicators.

CHAPTER 5

THE VERITAS STELLAR INTENSITY INTERFEROMETER

Following the experimental developments made in the laboratory and with the *StarBase*-Utah observatory (Matthews et al., 2018a), an SII instrument was constructed for use on the VERITAS telescopes. An initial iteration of the system was built during the Summer 2018, with on-sky tests beginning in Fall 2018. Observations of the two stars γ Orion and κ Orion were performed during January 2019, successfully measuring coherent intensity fluctuations with two of the telescopes. The system was then expanded to all four VERITAS telescopes, successfully completed in May of 2019. Observations in December 2019 of the β CMa and ϵ Orion allowed for the determination of the angular stellar diameters of both stars to a precision of 3-4% in agreement with prior results, thus establishing the working operation of the complete SII system. This chapter presents the current state of the VERITAS-Stellar Intensity Interferometer (VSII) and overviews the instrumentation and observations of β CMa and ϵ Orion.

5.1 Instrument

5.1.1 Camera

The VSII camera hardware is mounted onto a removable aluminum plate that is mounted in front of the VERITAS gamma-ray camera. A photograph of the camera with associated hardware is shown in Figure 5.1. On the plate, a 45° mirror[1] redirects the light from the primary onto an optical diaphragm with a diameter corresponding to approximately 0.1° on the sky. The light then passes through an interferometric filter with a vendor-specified center wavelength of 420 nm and bandpass of 5 nm.[2] Since the light is not collimated

---

[1] https://firstsurfacemirror.com/uv-enhanced-first-surface-mirror/

[2] https://www.semrock.com/FilterDetails.aspx?id=FF01-420/5-25

onto the filter the effective bandpass is broadened. Calculations established the resulting bandpass to be centered on a wavelength of 416 nm with an effective width of $\Delta\lambda = 13\,\text{nm}$. This effect reduces the overall spectral density throughput, and correspondingly, the signal-to-noise by approximately a factor of 2. A plot of the expected throughput including the effects of large AOI light, as well as other instrumental and atmospheric parameters are shown in Figure 5.2. The light is then detected by a Hamamatsu R10650 PMT (Otte, 2011). The gain of each PMT is controlled via battery-powered high voltage. The exact high voltage delivered to each PMT is individually controlled by adjusting the duty cycle of a pulse-width modulator that sets the high voltage level using an electrically isolated optical fiber (Cardon et al., 2019). A LabVIEW based graphical user interface was developed to remotely control the HV level delivered to each PMT. The output current of each PMT is fed into a low-noise trans-impedance FEMTO HCA-200M-20K-C 200 MHz pre-amplifier. The voltage output of the pre-amplifier drives a long triaxial cable that is connected to the data acquisition system for continuous readout.

5.1.2 Data acquisition

A National Instruments (NI) NI-5761 250 MHz DC-coupled analog-to-digital (ADC) converter continuously digitizes the amplified PMT signal at 250 MS/s with 14-bit resolution per sample (pushed into a signed 16-bit integer) over a peak to peak voltage range of 1.23 V. Digitized values are passed to a NI PXIe-7965R module, which hosts a Virtex 5 SX95T FPGA. The FPGA is programmed to downcast the sampled value to an 8-bit integer and push the data through a first-in-first-out (FIFO) buffer which is then streamed to a 12TB NI-8265 RAID disk array at a data rate of 250 MB/s per telescope. Figure 5.3 shows an example of the digitized waveforms recorded with all four telescopes.

5.1.3 Synchronization of data acquisition units

The ADC sample clock for each telescope is referenced and phase-locked to a common external 10 MHz clock. To generate the reference clock, a centrally located White Rabbit (WR) Switch is used to distribute a 10MHz clock through optical fiber connections to WR-Len modules each located near the respective data acquisition systems. The WR-Len module takes in the optical fiber signal and generates the synchronized electronic 10 MHz signal to which the ADC sample clock is referenced.

Tests in the laboratory were performed to establish the quality of the synchronization. Using a high bandwidth pulse generator, a narrow periodic square pulse of width $\Delta t \sim 2\,\mathrm{ns}$ was split and distributed to two separated data acquisition systems. The correlation was measured for each of the digitized signals. If the sampling of the separate systems are properly synchronized the cross-correlation between them should match closely with the measured auto-correlation of the signal. If, for example, there is a temporal drift in the sampling of one of the acquisition units relative to another, the cross-correlation will show a broader peak in time relative to the auto-correlation. The results of these tests are shown in Figure 5.4. The correlation was measured in two different synchronization configurations, one where the internal sampling clock was referenced to the external common 10 MHz clock (referenced), and another control test that did not reference the sample clock to the external clock (free-running). We see that in the referenced case, the cross-correlation closely matches that of the auto-correlation, demonstrating that the synchronization is stable to within a fraction of our sampling time. There is a relative shift of the signal of 1 sample, attributed to variability of the data acquisition systems ability to start acquiring data on the same clock cycle. For the free-running case, the correlation peak is much broader due to the relative drift of the sampling clock of each system. These tests validate the ability of the independent data acquisition systems to record synchronous data, and as well the need for a common external clock to provide the synchronization.

5.1.4 Correlator

In R. Hanbury-Brown's book on the development of intensity interferometry, he presents a quote stating "The most challenging part of constructing an intensity interferometer is the design of a satisfactory correlator." While still challenging today, the widespread availability of high speed digital electronics have significantly eased the complexity of a suitable correlator for intensity interferometry. For the VERITAS Stellar Intensity Interferometer a field programmable gate array (FPGA) based correlator was developed to perform the correlation between the data streams of the starlight intensity recorded at each of the telescopes. FPGAs were used due to their efficiency in processing data at large rates. In a single night of observation, a 6 hour data-set will generate a total of 5.4 TB of data at each telescope. The total available space in each hard drive is $\sim$ 10 TB, and therefore the data need to be processed before the next night of observation in order to clear space on the disks.

To perform the cross-correlation between the digitized starlight intensities $I_1(t_i)$ and $I_2(t_i)$, a multiply-accumulate algorithm is utilized where the correlation $c_N(k)$ over N samples is calculated as

$$c_N(k) = \frac{1}{N}\sum_{i=0}^{N-1} I_1(t_i)I_2(t_{i+k}) \tag{5.1}$$

where i is the FPGA clock cycle, and k is a digital time-lag inserted between the channels. The speed of this correlation algorithm is dependent on the maximum allowable FPGA clock cycle rate, and in our experience was limited to about 8 ns. Since the data are sampled at a rate of 4 ns, each pair of correlations would take twice the amount of time to process as it did to record, which would not be sufficient in order to clear hard drive space for observations on a subsequent night. To improve the correlator speed, multiple sequential samples can be processed in parallel. However, this requires that both the correlation at k and at $k+1$ be calculated in each clock cycle, thus demonstrating a trade between the hardware resource usage in the FPGA and computational speed of the correlation. For two sequential samples at t_i and t_{i+1} the correlation then becomes

$$c_N(k) = \frac{1}{N}\sum_{j=0}^{N-2} [I_1(t_i)I_2(t_{i+k}) + I_1(t_{i+1})I_2(t_{i+1+k})] \tag{5.2}$$

$$c_N(k+1) = \frac{1}{N}\sum_{j=0}^{N-2} [I_1(t_i)I_2(t_{i+k+1}) + I_1(t_{i+1})I_2(t_{i+1+k+1})] \tag{5.3}$$

where $i = j/2$, and $j = 2n$, with n being integer numbers. Since two samples are processed at a time, the overall number of clock cycles needed to do all the correlations is halved over the case when only one sample is processed per clock cycle, thus doubling the efficiency of the correlator if the FPGA clock cycle rate can be maintained.

The above algorithm was successfully compiled on the FPGA with a clock speed of 80 MHz processing two sequential samples per clock cycle over a total of 64 delay channels spanning time-delays from -128 to 124 ns in units of the sampling time of 4 ns. As a result, the correlator can process data samples at a rate of 160 MS/s. Since the data are recorded at rate of 250 MS/s, the computation time is longer than the observation time by a factor of ~ 1.6. Given the four telescopes available, there are six independent correlations between all telescope pairs. By running the correlations on a single FPGA, where each pair is processed sequentially, the total computation time would be almost 10 times that of the observation time, and thus a nightly observation of 6 hours would require 60 hours of processing. To alleviate this, a second FPGA was installed to parallelize the correlation, doubling the rate of computation. A 6 hour observation is then halved to approximately 30 hours of computation for all telescopes. Since the total processing time still exceeded the amount time between nightly observations, a spare drive was added on-site in order to provide overflow space for any observing runs not processed. While not optimal, this computational efficiency was sufficient for initial observations with all four telescopes in order to validate the rest of the SII instrumentation.

Future upgrades to the correlator include extending the algorithm to processing more than two samples per clock cycle, while maintaining the clock rate. By simply doubling the computation rate, the computational efficiency would allow for a processing of 7 hours of data in approximately 16 hours, sufficient for performing the correlation between all other telescope pairs between nightly observations. Extra FPGA correlators can also be added to further parallelize the correlation, up to the speed of the limiting bandwidth of either the network or disk read speed.

5.2 Observations

5.2.1 Installing the SII camera

To enable SII observations, the plate and corresponding SII optical and detector hardware are installed in front of the VERITAS gamma-ray camera as depicted in Figure 5.1. The location (and therefore the alignment) of the SII detector can be adjusted with sliding plates on which the PMT is mounted. The plates allow for the positioning of the PMT both along the optical axis, as well over the X-Y position in the focal plane. To align the PMT in the focal plane the location is matched to the center pixel of the VERITAS gamma-ray camera. This is performed using a beamsplitter mounted within an inset of the 45 degree mirror. The image of the SII-PMT can then be adjusted with the plates to align with the center pixel that, in principle, is matched to the positioning of the VERITAS tracking software.

The HV system is setup by connecting a fiber optic cable that provides control of the

HV level to the HV supply mounted on the SII camera. The HV supply is then connected to the PMT using a short coaxial cable. The HV supply is powered through a 15V battery supply mounted internally in the VERITAS camera and connected through a coaxial cable.

The output of each PMT signal preamplifier is connected to a double-shielded coaxial cable connected to the data acquisition system in each telescope trailer. The 45 degree mirror is collapsible allowing the entire system to be fully enclosed within the VERITAS camera shutter that is closed during daytime or in inclement weather. All hardware, with the exception of deploying/collapsing the mirror, is untouched after the SII plate is installed onto the VERITAS focal plane. At the end of the SII observing period, the cables are disconnected, and the plates are removed to allow gamma-ray observations. The plates are stored with dust covers over the mirrors and PMT in each VERITAS trailer.

5.2.2 Data Taking

A series of start-up procedures are performed to prepare observations:

- A trigger pulse is distributed to all telescopes and the recordings are checked to ensure that each system start data acquisition simultaneously.
- A calibration run is performed to measure the DC level of the PMT signal with the HV removed.
- After twilight, the HV to each PMT is tested to ensure that power to each of the detectors is provided.
- The telescopes are then slewed to the target of interest. The HV for each PMT is manually adjusted such that all detectors produce a DC photocurrent of $\sim 15\,\mu A$.

Once the start-up routine is completed, the data taking on stars can begin. A full observation of a given target star consists of a series of ON/OFF runs, where each run typically corresponds to 30/1 minute exposures, respectively. The ON runs reflect when the star is centered in the SII optics, whereas the OFF runs are taken on dark patches of sky within a few degrees of the target. A CCD camera (the VERITAS pointing monitor) enables monitoring of the star image in the focal plane. A snapshot of observations of a star slightly off-center is shown in Figure 5.5. Any residual inaccuracies in centering the star image can be corrected by adjusting the tracking software sky position.

A LabVIEW-based interface was developed to help monitor the recording of the data. The interface displays the recorded signal intensity over short time-buffers of $\sim 1\,\mu$s with the full 4 ns time resolution. In addition, the currents are averaged over a 1 second duration and displayed over longer timescales. The monitoring of the fast and slow signal intensity helps ensure data quality, and also provides an indication of changes to the atmospheric quality (e.g., thin clouds, aerosols, etc.).

5.3 Data analysis

The output of the correlator is a series of cross-correlations $\langle V_x(t)V_y(t+t_k)\rangle_i$ along with the average value $\langle V_x\rangle_i$ and $\langle V_y\rangle_i$ at each telescope over a series of integration periods or "accumulation frames" $i = 0\ldots N$, each corresponding to 1 second of data. The average currents over the same time periods $\langle V_x\rangle_i$ and $\langle V_y\rangle_i$ are also measured allowing us to calculate

$$g_i^{(2)}(t_k) = \frac{\langle V_x(t)V_y(t+t_k)\rangle_i}{\langle V_x\rangle_i\langle V_y\rangle_i} \tag{5.4}$$

over a range of discrete time-lags t_k performed over 64 time-lag channels spanning -128 to 124 ns in steps of 4 ns.

5.3.1 Correction for the optical path delay

As a star changes position in the sky, the geometrical optical path delay (OPD) between a given pair of telescopes is continuously changing on a scale that is generally greater than the time-resolution of the system. Since the desired coherence signal is observable at zero OPD, it must be accounted for before averaging all of the frames obtained in a run together. The OPD, τ_{OPD}, can be calculated from the target sky position given by the right ascension and declination, current time and observatory latitude and longitude, as well as the physical baseline separation betwen the telescopes measured in three dimensional orthogonal coordinates (East-West, North-South, and Up-Down separations) (Ségransan, 2007). Using prior measurements of the relative telescope positions shown in Table 5.1, the OPD is calculated for each frame. To correct for the OPD, each frame is shifted and centered by the average number of samples to zero optical path delay by performing

$$g_i^{(2)}(\tau_k) = g_i^{(2)}(t_k - t_{sig}) \tag{5.5}$$

where $t_{sig} = \text{round}(\tau_{OPD}/\Delta t)$.

5.3.2 Noise cuts

A series of quality control cuts are applied to frames that are either corrupted by spurious correlations or affected by a loss of photocurrent due to poor weather conditions. The spurious correlations are largely attributed to a narrowband, episodic RF emission that affects all VERITAS-SII telescopes at the same instance, but the source of which is unknown. The Fourier transform of each correlation frame is performed, where Figure 5.6 shows the power spectral density of all correlograms each averaged over one second integration for a run of 30 minutes. The signal attributed to the known noise frequency can be seen by the peak at $\sim 80\,\text{MHz}$ affecting many frames. To quantify if a run is affected by the noise, the following observable, herein referred to as the "noise ratio," is calculated

$$NR = \frac{P(f_N)}{\langle P(f \neq f_N) \rangle} \tag{5.6}$$

for all frames where $P(f_N)$ is the noise power at the frequency in which the noise power peaks (80 MHz), and $\langle P(f \neq f_N) \rangle$ is the average of the power at all other frequencies.

Figure 5.7 shows the evolution of NR as a function of time during a typical observation. Frames where NR goes high (NR greater than ~ 5) are corrupted by the spurious correlations, whereas in the converse case where NR goes low (NR approximately equal to 1) are not affected. A clear ON/OFF bimodal behavior seen where the noise will appear/disappear over timescales on the order of tens of seconds. The current analysis deals with the noise affected correlations by removing any frames in which NR exceeds a prespecified threshold. Typically, the threshold value of NR is ~ 5 but is varied over a range of values to ensure that there is no systematic effect to the value chosen.

After all correlogram frames are averaged together in a respective run, the Fourier transform of the resulting correlation is performed. Figure 5.8 shows the power spectral density distribution before and after noise cuts. If noise cuts are not applied, there is a dominant peak near the $80\,\text{MHz}$ noise frequency, which corrupts the averaged results. By including the threshold cut to frames that exceed a given NR, the noise contribution is removed, and the power spectral density is smooth with respect to frequency, indicating that episodic RF emission has been removed. Typically, 30 - 40% of the data are removed during the cuts, decreasing the usable data set to 60-70 % of the actual observation time. The achievable sensitivity is therefore degraded by $\sim$ 15 - 25%. Ideally, the noise should be treated in hardware rather than as a noise cut in software, and future work should focus on identifying the source of the noise, and developing schemes to remove or shield it to improve the observational duty cycle.

5.3.3 Correlator drift

After noise cuts are applied, each of the frames are zero-subtracted to remove the effects of "correlator drift," initially coined by HBT, that are non-Gaussian fluctuations of the zero-level of the correlator. The measurements of $g^{(2)}(\tau) - 1$ should fluctuate about zero for any time-lag where coherence is not expected. In practice, certain frames can significantly differ due to possible low frequency spurious correlations. Since the correlator spans a range of 250 ns, periodic spurious corrleations that occur over a much longer time-scale will appear as shifts in the zero-level of the correlator. The zero-drift is removed from each frame by calculating

$$\Delta g_i^{(2)}(\tau_k) = g_i^{(2)}(\tau_k) - \langle g_i^{(2)}(\tau_k) \rangle_{|\tau_k| \geq \sigma_\tau} \tag{5.7}$$

where $\langle g_i^{(2)}(\tau_k) \rangle_{|\tau_k| \geq \tau_{sig} + \sigma_\tau}$ is the average over all time-lag values excluding any that are within a time-window $\tau_k < \sigma_\tau$ where σ_τ represents an uncertainty window including both the width of expected $g^{(2)}$ correlation peak, and variability in the relative timing of the system. Figure 5.9 shows the evolution of the zero-drift throughout a run.

5.3.4 Measurement of the spatial coherence

Once noise cuts, path delay and zero-drift corrections have been applied to all frames, a weighted mean is performed to obtain a single correlation measurement for each observation run

$$\overline{\Delta g^{(2)}(\tau)} = \frac{\sum_i \Delta g_i^{(2)}(\tau) w_i}{\sum_i w_i} \tag{5.8}$$

where the weight w_i is determined by the scatter in the un-normalized correlation over all time lags divided by the product of the average signal intensities for a given time lag (i.e., in a given frame $w_i = 1/\sigma^2_{\Delta g_i^{(2)}}$) with

$$\sigma_{\Delta g^{(2)}} = \frac{\sigma_{\langle V_x V_y \rangle_i}}{\langle V_x \rangle_i \langle V_y \rangle_i} \tag{5.9}$$

where $\sigma_{\langle V_x V_y \rangle_i}$ is the standard deviation of the unormalized correlations. Weighting the error by the fluctuations over many independent time-lags takes into account the shot noise fluctuations as well as spurious correlations.

After the averaged $\Delta g^{(2)}(\tau_k)$ value has been calculated, the next step is to extract the correlation attributed to the spatial coherence. The signal should show up as an excess in the reduced $\Delta g^{(2)}(\tau_k)$ data within the time window $|\tau_k| < \sigma_\tau$. The shape of the excess peak is determined by the correlation of the optical time response of each system. The peak is modeled as Gaussian of the form

$$f(\tau) = Ae^{-\frac{1}{2}(\tau-\tau_0)^2/\sigma^2_{\tau_{g2}}} + C \tag{5.10}$$

with A, τ_0, and C left as fit parameters. A is the amplitude of the coherence peak and directly measures $|g^{(1)}(\mathbf{r})|^2$, τ_0 is a parameter that accounts for a variable start time between the separated data acquisition systems and is constrained within $|\tau| < 10\,\text{ns}$ of zero-lag, and C is another correction parameter that subtracts off any drift in the mean level of the correlator. The value of the fit width is fixed to a value of $\sigma^2_{\tau_{g2}} = 4.0\,\text{ns}$ determined empirically from the data and consistent with expectations from simulations. The value of the width was obtained by allowing it to be a free parameter in the fit of the integrated $\left|g^{(1)}(\tau)\right|^2$ correlation measurements for runs showing a peak amplitude with a p value less than 3×10^{-7}. The value of the fit width was stable within fit uncertainties for several runs demonstrating that no significant fluctuations in the relative timing of the acquisition systems are present.

Table 5.1: Relative telescope positions separated into East-West, North-South, and Up-Down directions

Tel.	B_{EW} (m)	B_{NS} (m)	B_{UD} (m)
T1	135.9	7.5	6.0
T2	45.1	-49.1	-0.95
T3	28.9	60.7	4.5
T4	-36.2	11.7	1.63

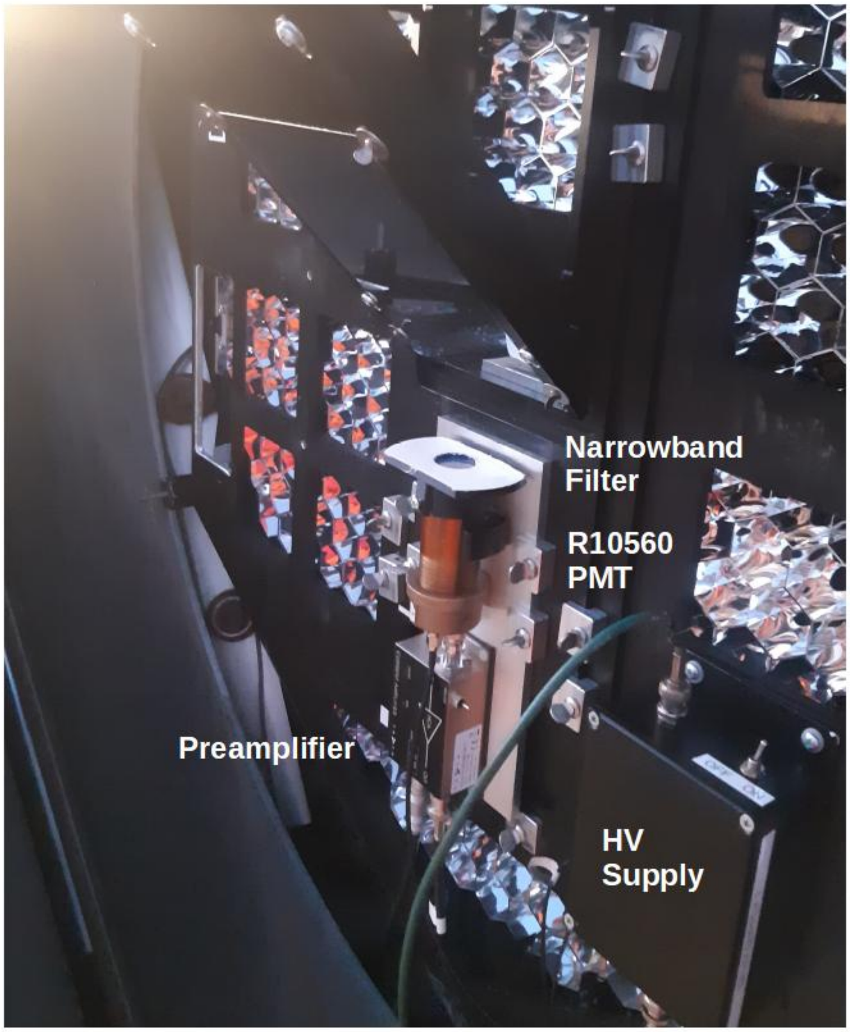

Figure 5.1: Photograph of the SII camera mounted in front of the VERITAS gamma-ray camera.

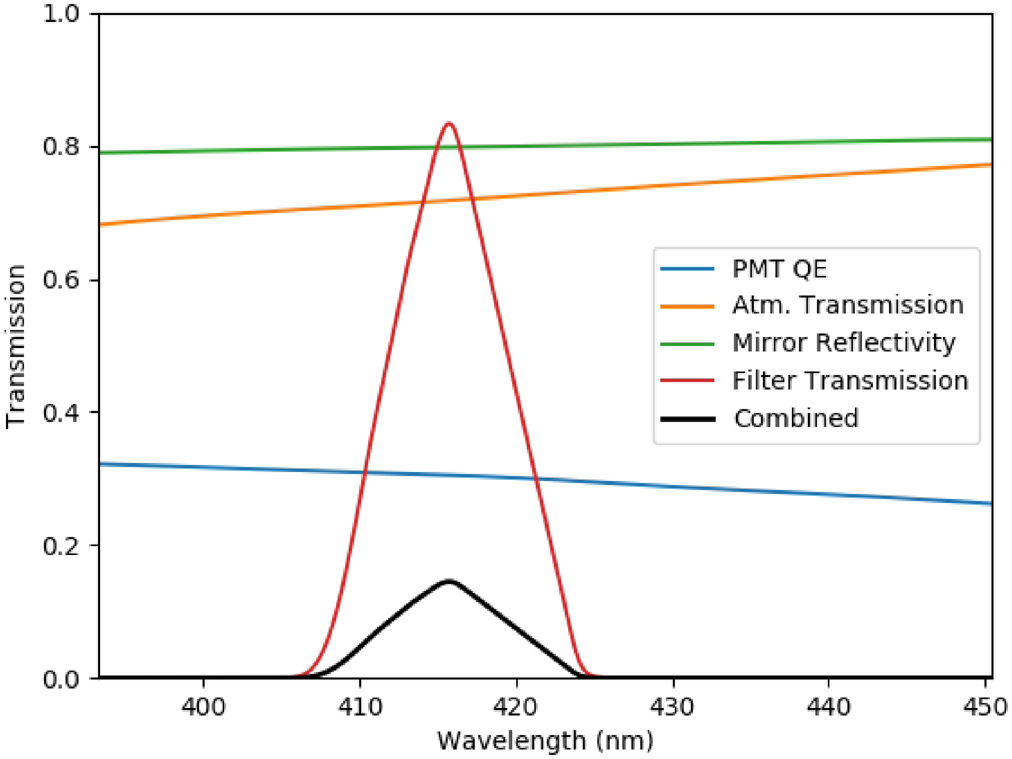

Figure 5.2: Calculation of the estimated spectral throughput including atmospheric and instrumental parameters.

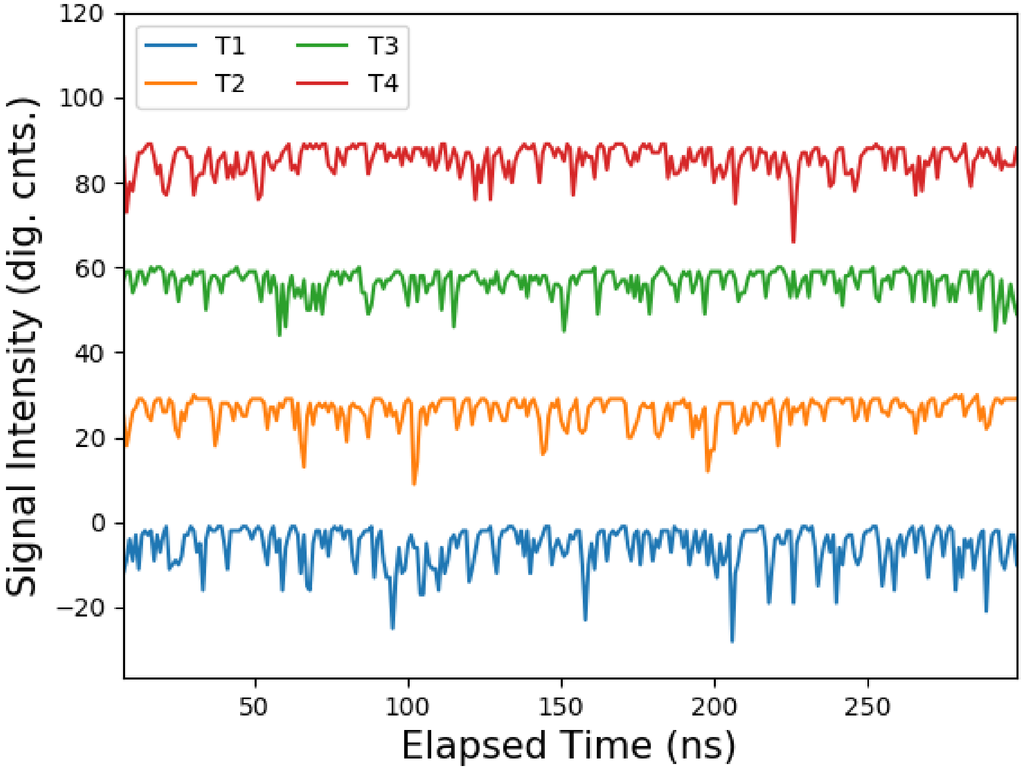

Figure 5.3: Waveforms from all four telescopes when exposed to a dark patch of the sky during bright moonlight conditions.

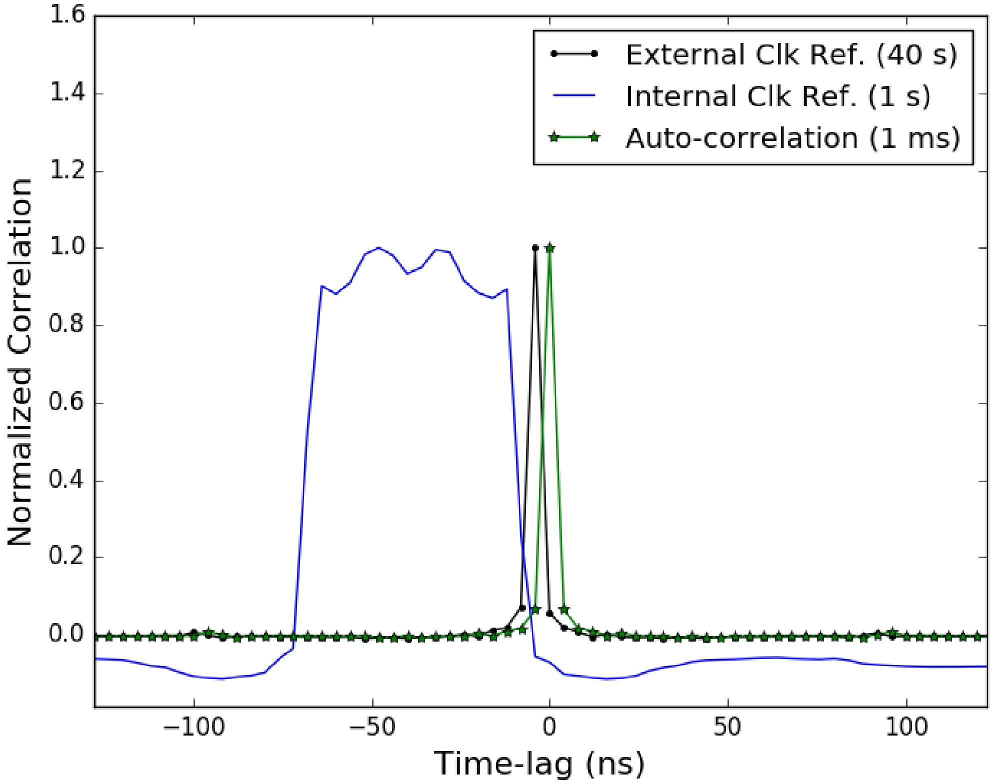

Figure 5.4: Results of laboratory tests on the synchronization of two separated DAQ systems. The green curve shows the auto-correlation measured by one of the DAQ units of a periodic square pulse with a very narrow pulse width. The cross-correlation between the signals measured in the two DAQs are also performed when a common clock is referenced (black) and when each DAQs refereneces an internal sample clock with external reference (blue). Clearly, in the case of no external reference the synchronization is poor, as the sampling between the systems drifts by amount much greater than the sampling time. When the external clock is referenced, the shape of the correlation matches that of the auto-correlation but offset by one sample due to variability in the start times of the systems.

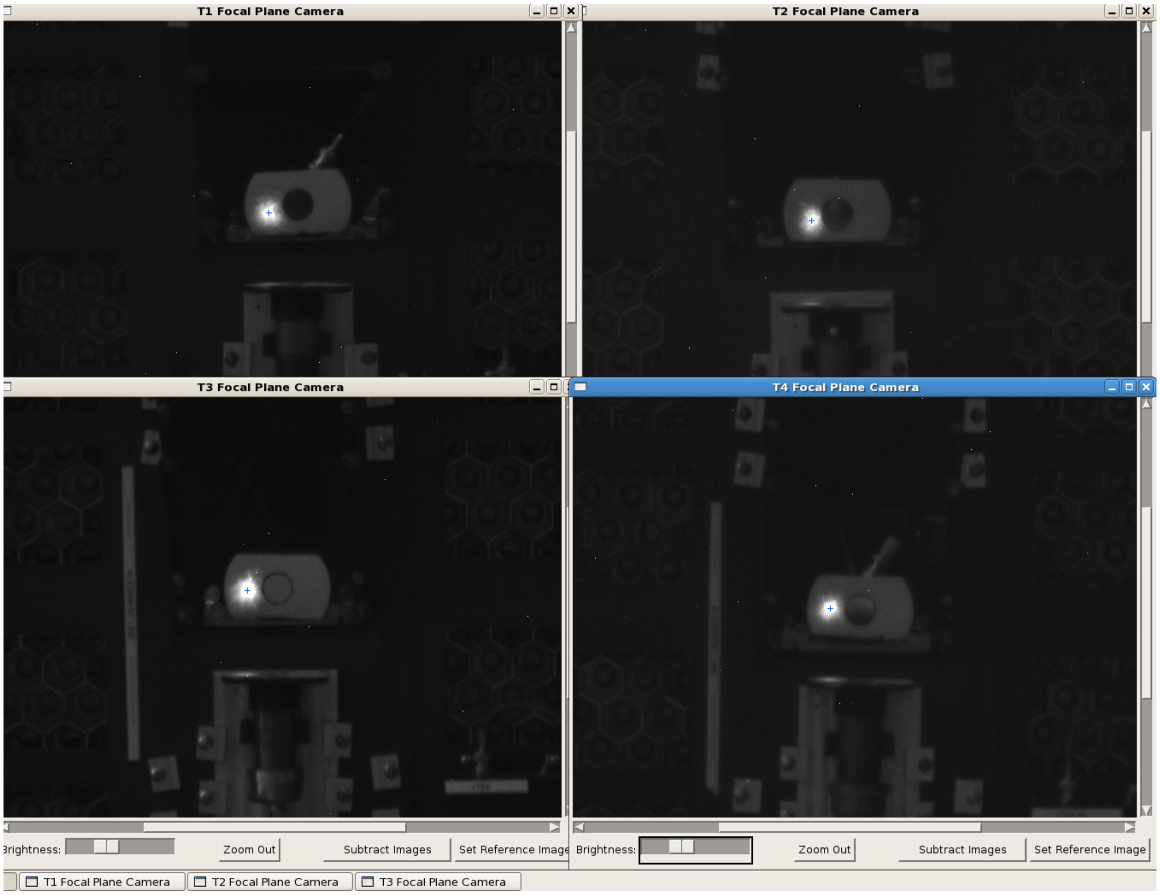

Figure 5.5: Image of the VERITAS telescope focal planes when tracking a stellar target.

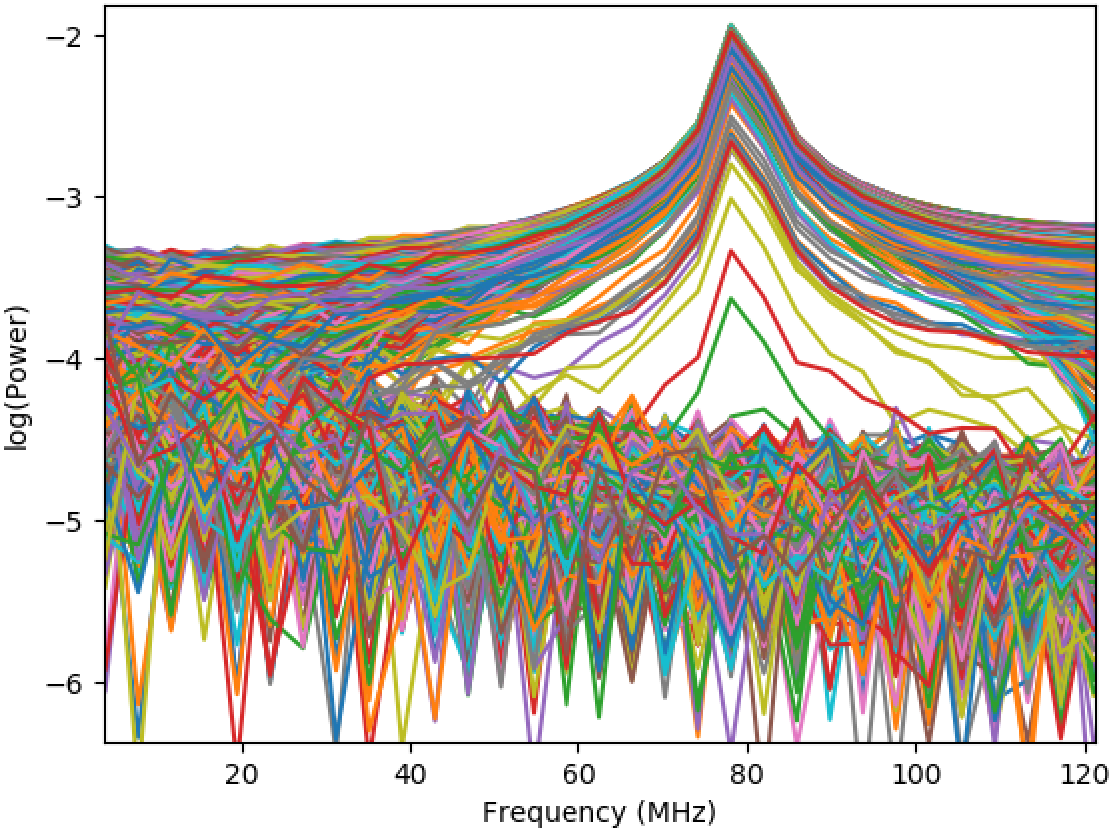

Figure 5.6: Power spectral density over all correlation frames for a single run where each line is a different frame.

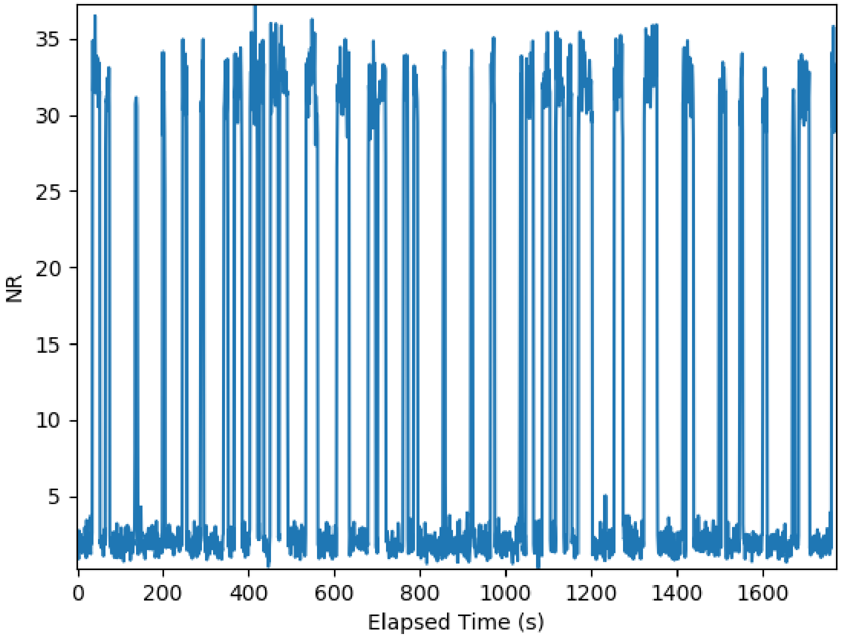

Figure 5.7: Evolution of the noise ratio over a typical 30 minute observation.

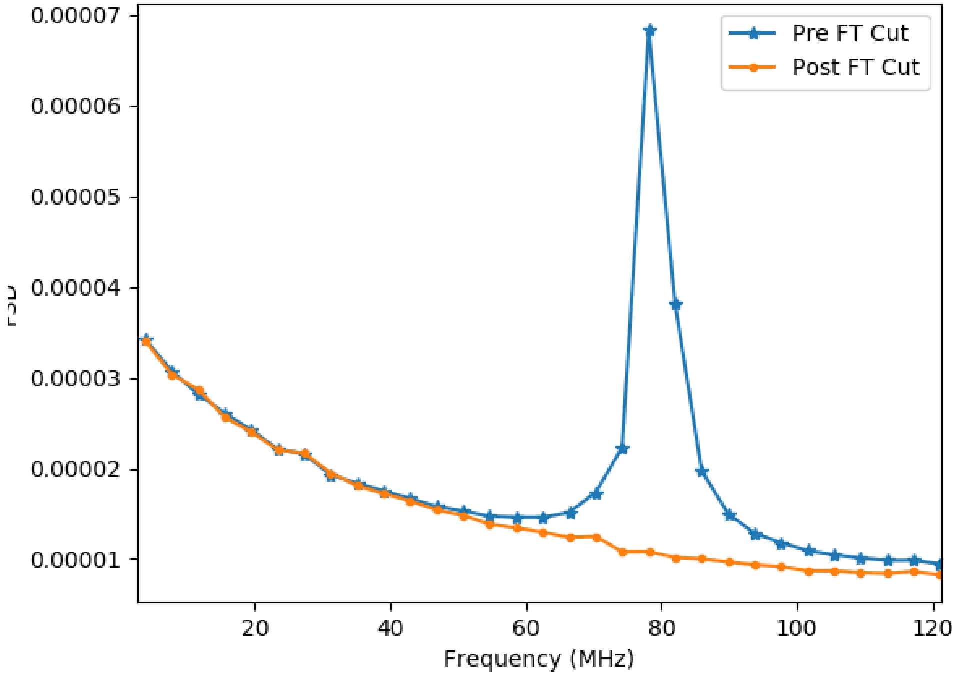

Figure 5.8: Power spectral density of the averaged correlation performed over all correlation frames before (blue) and post (orange) noise cuts.

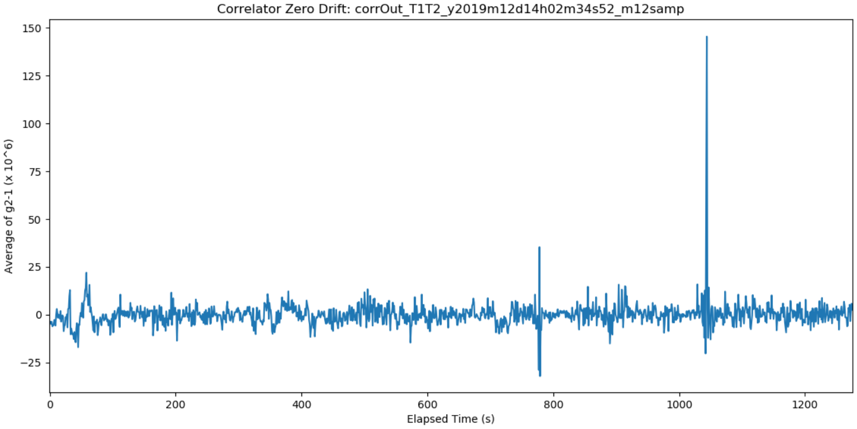

Figure 5.9: Evolution of the mean level of the correlator (zero-drift) over a run

CHAPTER 6

DEMONSTRATION OF STELLAR INTENSITY INTERFEROMETRY WITH THE FOUR VERITAS TELESCOPES

High angular resolution observations at optical wavelengths provide valuable insights in stellar astrophysics (Monnier, 2003; Ridgway et al., 2019), directly measuring fundamental stellar parameters (Boyajian et al., 2013; Casagrande et al., 2014), and probing stellar atmospheres, circumstellar disks (Kraus et al., 2012), elongation of rapidly rotating stars (van Belle, 2012), and pulsations of Cepheid variable stars (Kervella et al., 2017). The angular size of most stars are of order one milli-arcsecond or less, and to spatially resolve stellar disks and features at this scale requires an optical interferometer using an array of telescopes with baselines on the order of hundreds of meters. We report on the successful implementation of a stellar intensity interferometry system developed for the four VERITAS imaging atmospheric-Cherenkov telescopes. The system was used to measure the angular diameter of the two submas stars β Canis Majoris and ϵ Orionis with a precision better than 5%. The system utilizes an off-line approach where starlight intensity fluctuations recorded at each telescope are correlated after observation. The technique can be readily scaled onto tens to hundreds of telescopes, providing a capability that has proven technically challenging to current generation optical amplitude interferometry observatories. This work demonstrates the feasibility of performing astrophysical measurements with imaging atmospheric-Cherenkov telescope arrays as intensity interferometers and the promise for integrating an intensity interferometry system within future observatories such as the Cherenkov Telescope Array.

High-angular resolution optical astronomy is often performed through optical amplitude interferometry (OAI), which measures the source spatial coherence function by observing the fringe visibility of interference patterns produced when light collected at separated telescopes is superimposed (Labeyrie et al., 2006). One other approach is stellar intensity interferometry (SII) that instead uses correlations of star-light intensity fluctuations recorded with independent detectors on separated telescopes to measure the spatial coherence (Hanbury Brown and Twiss, 1957). SII was developed in the late 1950s (Hanbury Brown, 1974) and resulted in the Narrabri Stellar Intensity Interferometer (NSII) that was used for observations from 1963 to 1974, providing the first definitive catalog of 32 stellar angular diameters (Hanbury Brown et al., 1974a). Observations with the NSII were limited to only very bright stars with visual magnitudes less than 2.5. The sensitivity of an SII telescope is linearly proportional to the telescope area and detector efficiency, and inversely proportional to the square root of the time-resolution as shown in the Methods section (see Equation 6.6). The capabilities of the NSII were restricted by these factors and concurrent technical advancements in OAI provided substantial gains in the achievable limiting magnitude using much smaller telescopes, forestalling further developments in astronomical SII efforts.

SII has re-emerged as a viable technique for high-angular resolution astronomy primarily due to the potential of outfitting current and future large diameter ($> 10\,\mathrm{m}$) telescope arrays with SII capabilities (LeBohec and Holder, 2006; Pilyavsky et al., 2017b). A suitable SII instrument requires recording the star-light intensity with nanosecond level time-resolution and then correlating the intensities between telescope pairs. The optical path length only needs control with a precision no better than a few centimeters, determined by the light travel distance over a duration equal to the detector time resolution. The insensitivity to optical imperfections allows for SII instrumentation to be installed onto imaging atmospheric-Cherenkov telescope (IACT) arrays constructed for gamma-ray astronomy. With mirror diameters typically exceeding 10 m, IACTs are among the largest astronomical light collectors. IACTs employ fast ($\mathrm{f} \sim 1.0$) optics with segmented mirrors to reduce cost, and so the large light collection area is achieved at the expense of imaging resolution, but they remain capable for performing rapid optical photometry (Lacki, 2011) and SII measurements of stars that are several magnitudes fainter than those accessible to the NSII (Rou et al., 2013). There are several practical arguments for a modern SII observatory that uniquely complement the current capabilities of OAI. The tolerance to path length fluctuations allows for observations at all optical wavelengths, even in the U and B photometric bands that are generally inaccessible to OAI observatories on account of the required mechanical precision at a fraction of a wavelength. Furthermore, the baselines between telescopes can be made arbitrarily large in order to probe unprecedented angular scales as small as tens of microarcseconds with kilometer length baselines. A significant advantage of SII is that the technique can be scaled up to an arbitrary number of telescopes since only digital electronic connections are required (Dravins et al., 2015), enabling an optical intensity interferometry observatory that operates in a comparable way to radio interferometry. These realizations have led to several recent experimental efforts towards a modern intensity interferometer (Zampieri et al., 2016; Tan et al., 2016; Weiss et al., 2018; Zmija et al., 2020), successful SII observations of coherent intensity fluctuations using two telescopes (Guerin et al., 2018; Acciari et al., 2020), and distance calibration to the luminous blue variable P Cyg (Rivet et al., 2020). We improve upon these observations by directly measuring angular stellar diameters through fits to the squared visibility-baseline dependence with an SII system extended to four telescopes to provide six simultaneous baselines.

6.1 Observations of β CMa and ϵ Ori

We report here on observations of the two bright ($m_v < 2.1$), hot ($\mathrm{T} > 22{,}000\,\mathrm{K}$) B stars ϵ Ori (Alnilam) and β CMa (Mirzam) that were conducted using an SII system (see Methods) installed onto the Very Energetic Radiation Imaging Telescope Array System (VERITAS) IACTs shown in Figure 6.1 (Kieda et al., 2019). A total of 4.25 and 5.5 hours of data were taken of ϵ Ori and β CMa, respectively, spanning the nights of December 12-14, 2019, local time. The interferometric (u,v)-plane coverage (Ségransan, 2007) for both sources are shown in Figure 6.2.

The observations took place within a few days from the full moon when VERITAS does not operate as a gamma-ray instrument as the night sky background light overwhelms the faint Cherenkov signal. A custom camera is mounted near the focal plane of the VERITAS telescopes directly in front of the gamma-ray camera to enable SII observations. The starlight is passed through an interferometric filter with an effective center wavelength of $\lambda = 416\,\mathrm{nm}$ and bandpass of $\Delta\lambda = 13\,\mathrm{nm}$ that were chosen to match the peak reflectivity and quantum efficiency of the mirrors and detector. The filtered starlight is then detected by a photomultiplier tube. The resulting signal is continuously digitized and streamed to disk at a rate of 250 MS/s at each telescope. Correlations between the intensities recorded at each telescope are performed off-line using a field-programmable gate array. We then analyze the correlated data by correcting for instrumental and geometrical time delays, background light effects, and applying noise cuts to obtain the squared first-order coherence function $|g^{(1)}(\tau, \mathbf{r})|^2$ that is proportional to the squared visibility measured in OAI. It is a function of the path delay corrected time lag τ and projected baseline $\mathbf{r}$ that is defined as the separation between the telescopes as viewed from the star. As the star tracks through the sky, a given telescope pair will span a range of projected baselines. The amplitude of $|g^{(1)}(\mathbf{r})|^2$ at $\tau = 0$ measures the spatial coherence that is dependent on the source angular brightness distribution and projected baseline, reaching a minimum at the baseline $r \sim 1.22\lambda/\theta$ for an observation wavelength λ and stellar angular diameter θ. The angular diameter can then be determined by fitting the $|g^{(1)}(\mathbf{r})|^2$ measurements to an appropriate visibility model for a given source angular brightness distribution (see the Analysis section for more details). Stars that have a larger angular diameter will show a more rapid decline in $|g^{(1)}(\mathbf{r})|^2$ in comparison to stars with smaller angular diameters.

Figure 6.3 presents the temporal (top) and spatial (bottom) correlation measurements from the observations of β CMa (left) and ϵ Ori (right).

The top two panels show integrated $|g^{(1)}(\tau)|^2$ correlations for various pairs of the telescopes as a function of τ. The significant peak at $\tau = 0$ is the signal associated with the spatial coherence of the star. The width of the $|g^{(1)}(\tau)|^2$ peak is determined by the correlation between the combined telescope optics and detector time response at each telescope. The dashed lines show Gaussian fits to the data. The Gaussian fit width, representative of the temporal resolution time of the system, is fixed to 4 ns, as explained in Methods, and the amplitude is left as a free parameter. The lower panels of Figure 6.3 show values of $|g_*^{(1)}(\mathbf{r})|^2$ representing the correlation resulting only from star-light. These values are obtained by scaling the $|g^{(1)}(\tau, \mathbf{r})|^2$ amplitude fit by a factor that accounts for the effect of night sky background light and detector dark current. Each set of points are shown as a function of the projected baseline and correspond to an average of 17 minutes of data live-time per measurement. Using uniform-disk and limb-darkened models for the star angular brightness distribution, we perform a fit to the data with the stellar diameter and the zero-baseline correlation as free parameters. The shaded region shows the 68 % confidence regions obtained from the uniform-disk fit. The value of the zero-baseline correlation should be on the order of the ratio of the electronic to the optical bandwidth, each set by the instrumental system. In practice, the measured correlation can be affected by other factors including the telescope mirror extent, and spectral absorption or emission lines. We find that these additional effects are negligible in comparison to our measurement uncertainty, and thus the zero-baseline value should be the same for both stars. The zero-baseline normalization fit values are measured to be $N_0 = (1.23 \pm 0.05) \times 10^{-6}$ for β CMa, and $N_0 = (1.26 \pm 0.06) \times 10^{-6}$ for ϵ Ori, consistent within fitted errors thus demonstrating the reliability of the system to systematic effects in observations of different stars.

For β CMa, we find a uniform disk diameter of $\theta_{UD} = 0.523 \pm 0.017$ mas in agreement with the original NSII measurements of $\theta_{UD} = 0.50 \pm 0.03$ mas (Hanbury Brown et al., 1974a). In the case of ϵ Ori, we obtain $\theta_{UD} = 0.631 \pm 0.017$ mas, also in agreement with the NSII measurements ($\theta_{UD} = 0.67 \pm 0.04$ mas). Using a limb-darkened model, given by Equation 6.4, we find limb-darkened diameters of $\theta_{LD} = 0.542 \pm 0.018$ for β CMa and $\theta_{LD} = 0.660 \pm 0.018$ for ϵ Ori. We note that the VERITAS stellar intensity interferometer (VSII) gave more precise angular diameter measurements in comparison to the NSII, with less than a tenth of the observation time. The improvement is largely due to the greater light collection areas of the VERITAS mirrors, as well as the increased instantaneous baseline coverage offered by using multiple telescopes. To our knowledge, the angular diameters of these stars have not been measured since the time of the NSII. The current work thus provides confirmation of the NSII measurements of the stellar angular diameters to better than 5% uncertainty, a required capability for many science topics described later. Future observations can further reduce the uncertainty, as the root mean square fluctuations in the correlation should reduce inversely with the square root of the observation time. Here, we measure the uncertainty of the $|g^{(1)}(\tau)|^2$ fluctuations at a level of 2.0×10^{-8} for several telescope pairs using the entire data set for ϵ Ori. These values correspond to an uncertainty in the squared visibility of 1.6 % for the measured zero-baseline correlation of $N_0 = 1.26 \times 10^{-6}$. Extrapolating these results to fainter stars demonstrates the current capability to measure squared visibilities with a precision of 4.0 % for stars of magnitude 2.5 and 10 % for stars with magnitude 3.5 for equivalent observation time. Direct comparison of these results with the NSII (Hanbury Brown et al., 1974a) shows an improvement in the sensitivity by a factor of 6. Future improvements in the duty cycle and collimation of light through the narrowband filter offer expected gains in the sensitivity by a factor of 2 to 3, thus offering the potential for optical intensity interferometry measurements for stars with $m_B \sim 5$.

These two stellar angular diameter measurements with VSII demonstrate the feasibility of performing optical interferometry with IACT arrays. The approach developed here using high speed streaming with off-line correlations demonstrates the technical capability to perform optical intensity interferometry with tens to hundreds of telescopes, a capability that remains challenging for modern OAI observatories. We also show that SII observations increase the scientific output and scope of IACT observatories during bright moonlight conditions when gamma-ray observations are otherwise limited. The future Cherenkov Telescope Array (CTA) will employ up to 99 telescopes with up to kilometer baselines in the Southern hemisphere, and 19 telescopes in the Northern hemisphere with up to several hundred-meter baselines (Acharyya et al., 2019), allowing for unprecedented angular resolution capabilities approaching the tens of microarcsecond scale. The large number of telescopes would provide hundreds and possibly thousands of simultaneous baselines. Capability studies of SII on a CTA-like observatory demonstrate the ability to observe stellar targets brighter than a limiting visual magnitude of $m_V < 6$ or 7 (Nuñez et al., 2012). Science opportunities with a future CTA-SII observatory include surveying the angular diameter of stars larger than ~ 0.05 mas at short visible wavelengths, measuring the orbital and stellar parameters of interacting binaries (Dravins et al., 2013), characterizing the effects of gravity darkening and rotational deformation of rapidly rotating stars (Nuñez and Domiciano de Souza, 2015), and imaging of dark or hot star spots (Nuñez et al., 2012). The VSII observations presented here demonstrate the core requirements for such an observatory, thus providing a technological pathway in addition to performing SII observations with unprecedented sensitivity. Our results demonstrate the capability to attain squared visibilities at the level of a few percent and therefore can directly complement ongoing science campaigns pursued by current OAI observatories (Stee et al., 2017).

6.2 Methods

6.2.1 Instrumentation

The VERITAS observatory at the Fred Lawrence Whipple Observatory, located in Amado, AZ, consists of an array of four 12 meter diameter telescopes of the Davies-Cotton design. The primary mirrors of each telescope consist of 345 hexagonal mirror facets arranged in f/1 optics. SII hardware is mounted onto an aluminum plate that is installed in front of the VERITAS gamma-ray camera. Initial tests of the hardware were performed in the laboratory (Matthews et al., 2018b) and with on-sky tests at the *StarBase*-Utah observatory (Matthews et al., 2018a). The equipment was then scaled for use on the VERITAS telescopes with successful tests of correlated intensity fluctuations with two telescopes (Matthews, 2019). On the plate, a 45° mirror redirects the light from the primary onto an optical diaphragm with a diameter corresponding to approximately 0.1° on the sky. The light then passes through an interferometric filter (SEMROCK 420/5) with a vendor-specified center wavelength of 420 nm and bandpass of 5 nm. Since the light is not collimated onto the filter, the effective bandpass is broadened due to the large angle of incident light of up to 26.6 °. Calculations established the resulting bandpass to be centered on a wavelength of 416 nm with an effective width of 13 nm. This effect reduces the overall spectral density throughput, and correspondingly, the signal-to-noise by approximately a factor of 2. The light is then detected by a Hamamatsu R10650 photomultiplier tube (PMT) with a quantum efficiency of $\sim 30\,\%$ at the observing wavelength (Otte, 2011). The gain of the PMT is controlled via battery-powered high voltage. The exact high voltage delivered to the PMT is set by the duty cycle of a pulse-width modulator that is connected to the high voltage supply via an optical fiber (Cardon et al., 2019). The output current of the PMT is fed into a low-noise trans-impedance FEMTO HCA-200M-20K-C 200 MHz pre-amplifier. The voltage output of the pre-amplifier drives a long triaxial cable that is connected to the data acquisition system. A National Instruments (NI) NI-5761 DC-coupled analog-to-digital (ADC) converter continuously digitizes the amplified PMT signal at 250 MS/s with 14-bit resolution per sample over a peak to peak voltage range of 1.23 V. Digitized values are passed to a NI PXIe-7965R module, which hosts a Virtex 5 SX95T field-programmable gate array (FPGA). The FPGA is programmed to downcast the sampled value to an 8-bit integer, and push the data through a first-in-first-out buffer and then streamed to a 12TB NI-8265 RAID disk array at a data rate of 250 MB/s per telescope. The ADC sample clock for each telescope is referenced and phase-locked to a common external 10 MHz clock. To generate the reference clock, a centrally located White Rabbit (WR) Switch is used to distribute a 10MHz clock through optical fiber connections to a WR-Len module located near each of the data acquisition systems. The WR-Len module takes in the optical fiber signal and generates the electronic 10 MHz signal to which the ADC sample clock is referenced.

After observations are completed, the correlation between the stored data of each telescope is processed off-line by a FPGA-based correlator. The FPGA is programmed to retrieve the mean intensities of each time stream $\langle I\rangle = \frac{1}{N}\sum_i^N I(t_i)$, for the sample i, and the cross correlation between each pair of data streams, c(k) = $\langle I_1(t_i)I_2(t_{i+k})\rangle = \frac{1}{N}\sum_i^N I_1(t_i)I_2(t_{i+k})$, where k is a digital time-lag inserted between the two channels. The correlation is calculated over 64 time-lag channels, corresponding to time-lags of -128 to +124 ns in steps of 4 ns.

6.2.2 Analysis

From the outputs of the correlator, the second-order coherence function can be calculated by normalizing the cross correlation by the product of the mean intensities

$$g^{(2)}(\tau,\mathbf{r}) = \frac{\langle I_1(t)I_2(\mathbf{r},t+\tau)\rangle}{\langle I_1(t)\rangle\langle I_2(t)\rangle} \tag{6.1}$$

where $\mathbf{r} = \mathbf{r_1} - \mathbf{r_2}$ is the projected baseline between the two telescopes, τ is the relative time lag, and the brackets indicate a statistical average in time assuming a stationary light source. For chaotic thermal light, such as that from a star, the second-order coherence function can be written (Foellmi, C., 2009) in terms of the first-order coherence $g^{(1)}(\tau,\mathbf{r})$,

$$g^{(2)}(\tau,\mathbf{r}) = 1 + |g^{(1)}(\tau,\mathbf{r})|^2. \tag{6.2}$$

The van Cittert-Zernike theorem states that at $\tau = 0$, the measured first-order coherence is equivalent to the Fourier transform of the source angular intensity distribution in the sky (Born and Wolf, 1980). For randomly polarized light, the squared modulus of the first-order coherence is reduced by a factor of 1/2. In the typical case where the detector resolution time T is much longer than the light coherence time $\tau_c \sim 1/\Delta\nu$, where

$\Delta\nu$ is the optical bandwidth, it is reduced by another factor of $\sim \tau_c/T$. We then write the expected zero-baseline coherence as $N_0 = \epsilon\tau_c/2T$, where ϵ is a correction factor that accounts for the shape of the detected light spectral density that sets the optical bandwidth and corresponding coherence time. The correction factor also includes potential losses in the coherence signal that, as detailed by Hanbury-Brown and Twiss (Hanbury Brown, 1974), are attributed to nonideal properties of the filters, detectors, and electronic readout system that may influence the effective electronic or optical bandwidth. Under a uniform disk approximation for a star of angular diameter θ_{UD}, the squared first-order coherence can be written as

$$|g_*^{(1)}(\tau = 0, r)|^2 = N_0 \left| 2\frac{J_1(x_{UD})}{x_{UD}} \right|^2 \tag{6.3}$$

where $x_{UD} = \pi\theta_{UD} r/\lambda$, $|g_*^{(1)}|^2$ is the coherence due to starlight alone, i.e., $g_*^{(2)} = \langle I_{1_*} I_{2_*} \rangle / (\langle I_{1_*} \rangle \langle I_{2_*} \rangle)$, where I_{1_*} and I_{2_*} are the starlight intensities at detectors 1 and 2, J_1 is the Bessel function of the first kind, and λ is the mean observational wavelength. A linear limb-darkened model (Hanbury Brown et al., 1974b) was also fit to the data, where the expected squared first-order coherence is given by

$$|g_*^{(1)}(\tau = 0, \mathbf{r})|^2 = N_0 \left(\frac{1-u_\lambda}{2} + \frac{u_\lambda}{3} \right)^{-2} \left((1-u_\lambda)\frac{J_1(x_{LD})}{x_{LD}} + u_\lambda \sqrt{\pi/2}\frac{J_{3/2}(x_{LD})}{x_{LD}^{3/2}} \right)^2 \tag{6.4}$$

where u_λ is the wavelength-dependent linear limb-darkening coefficient, and $x_{LD} = \pi\theta_{LD} r/\lambda$, where θ_{LD} is the limb-darkened angular diameter.

The measured spatial coherence signal can be affected by detector dark current and background light. The total signal intensity can be written as a sum of the starlight and background light sources $I(t) = I_* + I_{bkg}$, and using Equation 6.1, it is straightforward to derive the relationship

$$|g_*^{(1)}|^2 = |g^{(1)}|^2 \times (1 + \beta_1)(1 + \beta_2) \tag{6.5}$$

under the assumption that the fluctuations in the starlight-background and background-background terms are uncorrelated (i.e., $\langle \Delta I_{1_*} \Delta I_{2_{bkg}} \rangle = \langle \Delta I_{1_{bkg}} \Delta I_{2_*} \rangle = \langle \Delta I_{1_{bkg}} \Delta I_{2_{bkg}} \rangle = 0$), where ΔI is the AC component of the given source intensity such that $I(t) = \langle I \rangle + \Delta I(t)$. The terms β_1 and β_2 are the ratios of the background to starlight intensity I_{bkg}/I_* for a given telescope.

Hanbury Brown and Twiss (1957) showed that the expected signal to noise ratio of the correlation due to the spatial coherence of the source, under a first-order approximation, is given as

$$S/N = A\,\alpha\,n\,|g^{(1)}(r)|^2\sqrt{\frac{\Delta f T_0}{2}} \tag{6.6}$$

where A is the telescope mirror area, α is the quantum efficiency of the detectors, n is the spectral flux density of the source given in units of ph s^{-1} m^{-2} Hz^{-1}, Δf is the electronic bandwidth set by the time-response of the combined optical and electronic system, and T_0 is the observation duration.

For a given run, typically 20 to 30 minutes in total duration, the value of $\left|g^{(1)}(\tau)\right|^2$ is calculated over accumulation frames of 1 second. Any $\left|g^{(1)}(\tau)\right|^2$ frames contaminated by correlated high-frequency radio pickup are removed. The Fourier transform of each frame is calculated to identify corrupted frames. If the power at the specific noise frequency is greater than the average power over all other frequencies by a predetermined threshold cut, the frame is removed. For a typical run, 30 - 40 % of the data are removed as a result of the electronic noise. Additionally, any frames are removed where the mean PMT current falls below 5 μA, or approximately one-half of the total current due to star light. These current losses are attributed to the attenuation of star light by clouds, or also imperfect tracking that results in the collected star-light not centered onto the detectors. Each frame is shifted in time by the average number of samples to zero optical path delay to correct for the geometrical optical path-delay. After path-delay corrections and noise/current cuts are applied, all $|g^{(1)}(\tau)|^2$ frames are averaged together through a weighted mean to produce a final $|g^{(1)}(\tau)|^2$ frame for that run. The weights for each frame are given by $1/\sigma^2_{|g^{(1)}|^2}$ where $\sigma_{|g^{(1)}|^2} = \sigma_{\langle I_1 I_2\rangle}/\left(\langle I_1\rangle\langle I_2\rangle\right)$, and where $\sigma_{\langle I_1 I_2\rangle}$ is the standard deviation of the correlation over all time-lag bins for a given frame. Provided sufficient throughput and spatial coherence, the corrected and averaged results reveal an excess peak at zero time lag due to the spatial coherence of the source. In our case where the detector resolution time is much greater than the coherence time of the light, the shape of the peak is determined by the cross-correlation of the telescope and detector time response with an amplitude proportional to the amount of spatial coherence. The Davies-Cotton mirror design of the VERITAS telescopes introduces an approximate 4 ns spread in the arrival time of photons that otherwise would arrive synchronously (Holder et al., 2006). A PMT detects the photons, with a characteristic single photo-electron pulse width of 3.7 ns and additional timing jitter on the order of 1 ns. Simulations of these effects find that the $\left|g^{(1)}(\tau)\right|^2$ peak can be modeled as a Gaussian following the form

$$f(\tau) = Ae^{-\frac{1}{2}(\tau-\tau_0)^2/\sigma_\tau^2} + C \tag{6.7}$$

with A, τ_0, and C left as fit parameters. A is the amplitude of the coherence peak and directly measures $|g^{(1)}(\mathbf{r})|^2$, τ_0 is a parameter that accounts for a variable start time between the separated data acquisition systems and is constrained within $|\tau| < 10\,\mathrm{ns}$ of zero-lag, and C is another correction parameter that subtracts off any drift in the mean level of the correlator. The value of the fit width is fixed to a value of $\sigma_\tau = 4.0\,\mathrm{ns}$ determined empirically from the data and consistent with expectations from simulations. The value of the width was obtained by allowing it to be a free parameter in the fit of the integrated $\left|g^{(1)}(\tau)\right|^2$ correlation measurements for runs showing a peak amplitude with a p value less than 3×10^{-7}. The value of the fit width was stable within fit uncertainties for several runs demonstrating that no significant fluctuations in the relative timing of the acquisition systems are present.

The value of the fit amplitude and corresponding uncertainty are found for all runs to measure $\left|g^{(1)}(\tau = 0)\right|^2$ as a function of the projected baseline. The projected baseline is calculated from the telescope positions and source sky position at the time of observation. The value of the fit amplitude is then multiplied by the scaling factor described in Equation 6.5 to compensate for night sky background and detector dark current. The mean level of the background is found by pointing the telescope off source and recording the average intensity. These off runs are taken before and after each run on source. The background light corrected values of $|g_*^{(1)}|^2$ are then fit to a function with the form of Equation 6.3 in order to obtain the uniform-disk normalization and stellar diameter. Values of the linear limb-darkening coefficient u_λ were estimated by interpolating existing tables that calculate expected values of u_λ from atmospheric parameters (Claret and Bloemen, 2011). Using the atmospheric values listed in Table 6.1, for observations in the B band, a microturbulent velocity of 2 km/s, and solar metallicity, we find values of u_λ of 0.38 and 0.46 for β CMa and ϵ Ori, respectively.

Table 6.1: Atmospheric parameters used to estimate values of the linear limb-darkening coefficient. The spectral type and B band magnitudes were obtained from SIMBAD. ^{a} Taken from reference (Levenhagen and Leister, 2006), ^{b} taken from reference (Crowther et al., 2006), ^{c} and taken from reference (Abt et al., 2002).

Source	Spectral Type	B	T_{eff} (K)	$log(g)$ (dex)	$v\sin(i)$ (km/s)
β CMa	BII/III	1.73	24000 ± 500^a	3.43 ± 0.10^a	20 ± 7^a
ϵ Ori	B0Ia	1.51	27000 ± 1000^b	2.90 ± 0.02^b	65 ± 15^c

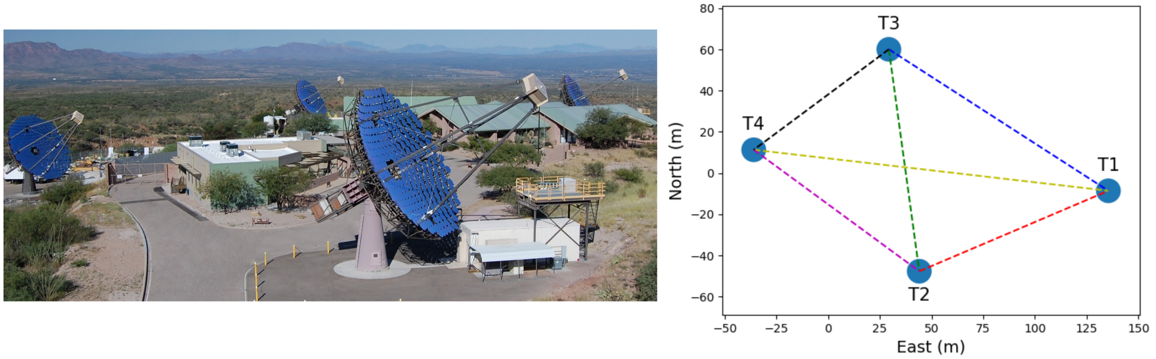

Figure 6.1: The VERITAS array. The left image shows a photograph of VERITAS located at the Fred Lawrence Whipple Observatory located in Amado, Az. The array consists of four 12 m diameter telescopes, T1 (front-center), T2 (leftmost), T3 (rightmost), and T4 (back-center). The right plot shows a top-down view of the array with each of the radial telescope separations.

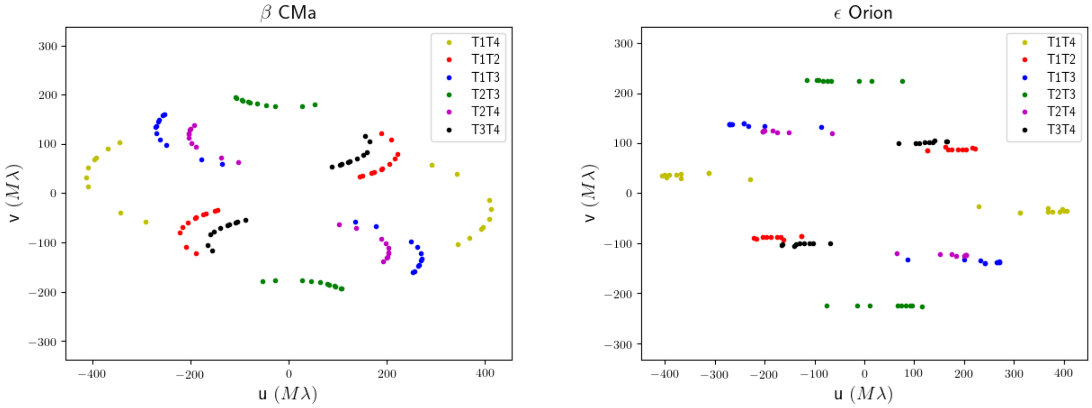

Figure 6.2: Coverage of the sources in the (u,v)-plane. Each of the colored points represent different runs for a given telescope pair.

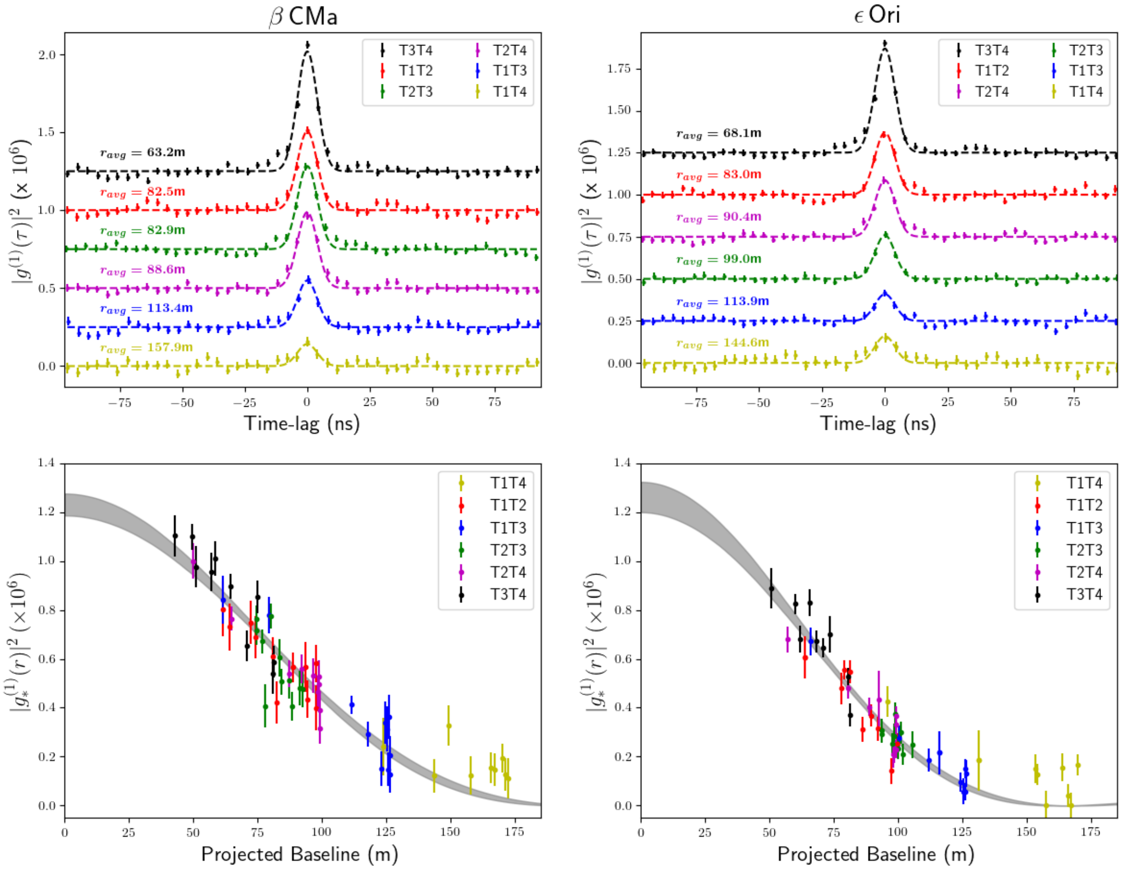

Figure 6.3: Temporal and spatial coherence measurements. The top two panels show the averaged $|g^{(1)}(\tau)|^2$ correlation measurements over the full live time between different pairs of telescopes for β CMa (left) and ϵ Ori (right). Each respective telescope pair measurement is color-coded matching the combinations shown in Figure 6.1. The uncertainties are given by the standard deviation of the mean normalized correlation and are estimated independently for each time-lag. The correlations are ordered by increasing average baseline from the top, corresponding to decreasing spatial coherence. The dashed lines show Gaussian fits to the data. The amplitude and corresponding fit uncertainty of the $|g^{(1)}(\tau)|^2$ peak over shorter time intervals are obtained as a function of the baseline and shown by the individual points in the bottom panels. The uncertainty is determined by the square root of the covariance matrix resulting from the fit. These measurements are fit to a function that approximates the star as a uniform disk (see Equation 6.3) and includes free parameters for the overall normalization and angular diameter. The shaded area shows the 68 % confidence intervals determined through the uncertainty in the fit parameters.

CHAPTER 7

CONCLUSIONS

Stellar intensity interferometry can once again advance our understanding of stellar astrophysics by improving the angular resolution and extending the spectral coverage offered by current optical interferometric observatories. The advent of arrays of large diameter optical telescopes and technological progress in the capabilities of detector and data readout systems offer the potential for an SII observatory that is several orders of magnitude more sensitive than the original Narrabri Stellar Intensity Interferometer and can match, if not exceed, the limiting stellar magnitude of current state-of-the-art interferometric observatories at visible wavelengths. Intensity interferometry can be used for high angular resolution observations of many interesting stellar systems to measure stellar angular diameters, study of high-mass/early-type stars, the orbital motion and individual components of close binary systems, and probe the surfaces and extended line regions of emission-line stars.

The main astrophysical result of this work was of the diameter of two bright B stars, β CMa and ϵ Ori. The angular diameters were obtained with a precision better than 5%, improving the current measurement by a factor of two and was achieved using less than 1/10th of the prior observation time. These results clearly demonstrate an improvement over the NSII. Future observations can extend these angular diameter measurements to fainter stars previously unmeasured, or extended duration observations can be performed to improve the uncertainty.

Future IACT arrays will employ tens of telescopes dispersed with up to kilometric baselines (Acharyya et al., 2019), offering unprecedented (u,v)-plane coverage and resolution capabilities. These observatories, while designed for gamma-ray astronomy, are suitable for SII observations, and this realization has spawned a large amount of experimental effort towards developing SII instruments with them. All major IACT observatories (MAGIC, HESS, and VERITAS) are pursuing SII observations, where successful on-sky results have come very recently demonstrating the feasibility of SII observations with these observatories. Here, SII observations were successfully performed using more than two telescopes demonstrating a core capability for an intensity interferometry system within future IACT arrays. A high-speed continuously digitizing system developed here allowed for the processing correlations after observation providing a novel technical achievement for intensity interferometry. An FPGA correlator was programmed to process the correlations between all four pairs of telescopes on daily timescales. It therfore was able to manage the large volume of data, on the order of tens of TB's per night, generated in this continuous streaming approach. The system can be readily scaled to additional telescopes by duplicating the current system for each added telescope.

While IACT telescopes are attractive to use for SII, the relatively poor optical quality presents a few unique challenges when using them as SII observatories. Particularly, the fast optics and large PSF make it challenging to spectrally filter to a bandpass of a few nanometers. The current system here takes advantage of the fact that the degradation of the sensitivity is mitigated when using interferometric filters with a high coating refractive index. For this initial implementation of the instrument, the optical system was kept very simple consisting of a single narrowband filter placed in front of the PMT. Future work and any proposed upgrade should attempt to improve the quality of the filter transmission over the entire mirror area. In principle, a standard approach is to incorporating large diameter collimating optics. There are also possibilities for using multiple interferometric filter segments laid along a surface that minimizes the indicent angle of light from different mirror annuli. We estimate that improving the quality of the filter transmission over the mirror area can improve the sensitivity of the instrument by a factor of 2 to 3. Furthermore, if a reasonably narrow band can be achieved, the possibility of observing within the emission lines of certain stars is opened to prove the extended circumstellar material associated with the emission line. Since SII can operate at short optical wavelengths, this allows for observation in several emission lines not available to current observatories including Hβ, but also even other emission lines that are seen, for example, in the spectra of luminous blue variable stars.

REFERENCES

Abeysekara, A. U., Benbow, W., Brill, A., et al. 2020, NaturAs, 4, 1164, doi: `10.1038/s41550-020-1143-y`

Abt, H. A., Levato, H., and Grosso, M. 2002, ApJ, 573, 359, doi: `10.1086/340590`

Acciari, V. A., Bernardos, M. I., Colombo, E., et al. 2020, MNRAS, 491, 1540, doi: `10.1093/mnras/stz3171`

Acharyya, A., Agudo, I., Angüner, E., et al. 2019, APh, 111, 35 , doi: `https://doi.org/10.1016/j.astropartphys.2019.04.001`

Anugu, N., Le Bouquin, J.-B., Monnier, J. D., et al. 2020, arXiv e-prints, arXiv:2007.12320. `https://arxiv.org/abs/2007.12320`

Armstrong, J. T., Hutter, D. J., Baines, E. K., et al. 2013, JAI, 2, 1340002, doi: `10.1142/S2251171713400023`

Berger, J. P., and Segransan, D. 2007, NewAR, 51, 576 , doi: `https://doi.org/10.1016/j.newar.2007.06.003`

Bessell, M. S. 1979, PASP, 91, 589, doi: `10.1086/130542`

Born, M., and Wolf, E. 1980, in Principles of Optics (Sixth Edition), sixth edition edn., ed. M. Born and E. Wolf (Pergamon), 491 – 555, doi: `https://doi.org/10.1016/B978-0-08-026482-0.50017-7`

Bourges, L., Mella, G., Lafrasse, S., et al. 2017, VizieR Online Data Catalog, II/346

Boyajian, T. S., von Braun, K., van Belle, G., et al. 2013, ApJ, 771, 40, doi: `10.1088/0004-637x/771/1/40`

Cardon, R., Matthews, N., Abeysekara, U., and Kieda, D. 2019, in 36th International Cosmic Ray Conference, Vol. 358

Casagrande, L., Portinari, L., Glass, I. S., et al. 2014, MNRAS, 439, 2060, doi: `10.1093/mnras/stu089`

Che, X., Monnier, J. D., Zhao, M., et al. 2011, ApJ, 732, 68, doi: `10.1088/0004-637X/732/2/68`

Claret, A., and Bloemen, S. 2011, A&A, 529, A75, doi: `10.1051/0004-6361/201116451`

Crowther, P. A., Lennon, D. J., and Walborn, N. R. 2006, A&A, 446, 279, doi: `10.1051/0004-6361:20053685`

Davies, J. M., and Cotton, E. S. 1957, Solar Energy, 1, 16 , doi: `https://doi.org/10.1016/`

0038-092X(57)90116-0

Dravins, D., Lagadec, T., and Nuñez, P. D. 2015, A&A, 580, A99, doi: `10.1051/0004-6361/201526334`

Dravins, D., LeBohec, S., Jensen, H., and Nuñez, P. D. 2013, APh, 43, 331 , doi: `https://doi.org/10.1016/j.astropartphys.2012.04.017`

Duvert, G. 2016, VizieR Online Data Catalog, II/345

Foellmi, C. 2009, A&A, 507, 1719, doi: `10.1051/0004-6361/200911739`

Gaia Collaboration, Brown, A. G. A., Vallenari, A., et al. 2018, A&A, 616, A1, doi: `10.1051/0004-6361/201833051`

Gordon, K. D., Gies, D. R., Schaefer, G. H., Huber, D., and Ireland, M. 2019, ApJ, 873, 91, doi: `10.3847/1538-4357/ab04b2`

Gordon, K. D., Gies, D. R., Schaefer, G. H., et al. 2018, ApJ, 869, 37, doi: `10.3847/1538-4357/aaec04`

Granada, A., Ekström, S., Georgy, C., et al. 2013, A&A, 553, A25, doi: `10.1051/0004-6361/201220559`

Gravity Collaboration, Abuter, R., Amorim, A., et al. 2018, A&A, 615, L15, doi: `10.1051/0004-6361/201833718`

Guerin, W., Dussaux, A., Fouché, M., et al. 2017, MNRAS, 472, 4126, doi: `10.1093/mnras/stx2143`

Guerin, W., Rivet, J.-P., Fouché, M., et al. 2018, MNRAS, 480, 245, doi: `10.1093/mnras/sty1792`

Hanbury Brown, R. 1974, The intensity interferometer. Its applications to astronomy (Taylor & Francis)

Hanbury Brown, R., Davis, J., and Allen, L. R. 1974a, MNRAS, 167, 121, doi: `10.1093/mnras/167.1.121`

Hanbury Brown, R., Davis, J., Herbison-Evans, D., and Allen, L. R. 1970, MNRAS, 148, 103, doi: `10.1093/mnras/148.1.103`

Hanbury Brown, R., Davis, J., Lake, R. J. W., and Thompson, R. J. 1974b, MNRAS, 167, 475, doi: `10.1093/mnras/167.3.475`

Hanbury Brown, R., and Twiss, R. Q. 1954, Philosophical Magazine, 45, 663, doi: `10.1080/14786440708520475`

—. 1956, Natur, 177, 27, doi: `10.1038/177027a0`

—. 1957, RSPA, 242, 300, doi: `10.1098/rspa.1957.0177`

—. 1958a, RSPA, 248, 199. `http://www.jstor.org/stable/100597`

—. 1958b, RSPA, 243, 291, doi: `10.1098/rspa.1958.0001`

Hecht, E. 2010, Optics, 5th edn. (Pearson)

Herbison-Evans, D., Hanbury Brown, R., Davis, J., and Allen, L. R. 1971, MNRAS, 151, 161, doi: `10.1093/mnras/151.2.161`

Holder, J., Atkins, R. W., Badran, H. M., et al. 2006, APh, 25, 391, doi: `10.1016/j.astropartphys.2006.04.002`

Ireland, M. J., Mérand, A., ten Brummelaar, T. A., et al. 2008, in Optical and Infrared Interferometry, ed. M. Schöller, W. C. Danchi, and F. Delplancke, Vol. 7013, International Society for Optics and Photonics (SPIE), 681 – 690, doi: `10.1117/12.788386`

Kervella, P., Trahin, B., Bond, H. E., et al. 2017, A&A, 600, A127, doi: `10.1051/0004-6361/201630202`

Kieda, D., for the VERITAS Collaboration, T., LeBohec, S., and R., C. 2019, in International Cosmic Ray Conference, Vol. 358, 36th International Cosmic Ray Conference

Kloppenborg, B., Stencel, R., Monnier, J. D., et al. 2010, Natur, 464, 870, doi: `10.1038/nature08968`

Kraus, S., Monnier, J. D., Che, X., et al. 2012, ApJ, 744, 19, doi: `10.1088/0004-637X/744/1/19`

Krisciunas, K., and Schaefer, B. E. 1991, PASP, 103, 1033, doi: `10.1086/132921`

Labeyrie, A. 1970, A&A, 6, 85

—. 1975, ApJ, 196, L71, doi: `10.1086/181747`

Labeyrie, A., Lipson, S. G., and Nisenson, P. 2006, An Introduction to Optical Stellar Interferometry (Cambridge University Press), doi: `10.2277/0521828724`

Lacki, B. C. 2011, MNRAS, 416, 3075, doi: `10.1111/j.1365-2966.2011.19255.x`

LeBohec, S., and Holder, J. 2006, ApJ, 649, 399–405, doi: `10.1086/506379`

Levenhagen, R. S., and Leister, N. V. 2006, MNRAS, 371, 252, doi: `10.1111/j.1365-2966.2006.10655.x`

Maestro, V., Che, X., Huber, D., et al. 2013, MNRAS, 434, 1321, doi: `10.1093/mnras/stt1092`

Mandel, L. 1963, PrOpt, 2, 181, doi: `10.1016/S0079-6638(08)70560-2`

Mandel, L., and Wolf, E. 1995, Optical Coherence and Quantum Optics (Cambridge University Press), doi: `10.1017/CBO9781139644105`

Mann, A. W., Feiden, G. A., Gaidos, E., Boyajian, T., and von Braun, K. 2015, ApJ, 804, 64, doi: `10.1088/0004-637X/804/1/64`

Martienssen, W., and Spiller, E. 1964, AmJPh, 32, 919, doi: `10.1119/1.1970023`

Matthews, N. 2019, in International Cosmic Ray Conference, Vol. 36, 36th International Cosmic Ray Conference (ICRC2019), 740. `https://arxiv.org/abs/1908.03587`

Matthews, N., Clarke, O., Snow, S., LeBohec, S., and Kieda, D. 2018a, in Society of Photo-Optical Instrumentation Engineers (SPIE) Conference Series, Vol. 10701, Optical and Infrared Interferometry and Imaging VI, 107010W, doi: `10.1117/12.2312716`

Matthews, N., D., K., and S., L. 2018b, JMO, 65, 1336, doi: `10.1080/09500340.2017.1360958`

Michelson, A. A., and Pease, F. G. 1921, ApJ, 53, 249, doi: `10.1086/142603`

Monnier, J. D. 2003, RPPh, 66, 789, doi: `10.1088/0034-4885/66/5/203`

Mourard, D., Challouf, M., Ligi, R., et al. 2012, in Optical and Infrared Interferometry III, ed. F. Delplancke, J. K. Rajagopal, and F. Malbet, Vol. 8445, International Society for Optics and Photonics (SPIE), 200 – 210, doi: `10.1117/12.925223`

Nuñez, P. D., and Domiciano de Souza, A. 2015, MNRAS, 453, 1999, doi: `10.1093/mnras/stv1719`

Nuñez, P. D., Holmes, R., Kieda, D., Rou, J., and LeBohec, S. 2012, MNRAS, 424, 1006, doi: `10.1111/j.1365-2966.2012.21263.x`

Otte, A. N. 2011, in 32nd International Cosmic Ray Conference

Paladini, C., Baron, F., Jorissen, A., et al. 2018, Natur, 553, 310, doi: `10.1038/nature25001`

Pease, F. G. 1921a, PNAS, 7, 177, doi: `10.1073/pnas.7.6.177`

—. 1921b, PASP, 33, 204, doi: `10.1086/123081`

Pilyavsky, G., Mauskopf, P., Smith, N., et al. 2017a, MNRAS, 467, 3048, doi: `10.1093/mnras/stx272`

—. 2017b, MNRAS, 467, 3048, doi: `10.1093/mnras/stx272`

Ridgway, S., Armstrong, J. T., Baines, E. K., et al. 2019, in BAAS, Vol. 51, 157

Rivet, J. P., Siciak, A., de Almeida, E. S. G., et al. 2020, MNRAS, 494, 218, doi: `10.1093/mnras/staa588`

Rou, J., Nuñez, P. D., Kieda, D., and LeBohec, S. 2013, MNRAS, 430, 3187, doi: `10.1093/mnras/stt123`

Schaefer, G. H., Gies, D. R., Monnier, J. D., et al. 2010, AJ, 140, 1838, doi: `10.1088/0004-6256/140/6/1838`

Schaefer, G. H., Brummelaar, T. T., Gies, D. R., et al. 2014, Natur, 515, 234, doi: `10.1038/nature13834`

Serrano, J., Alvarez, P., Cattin, M., et al. 2009, The White Rabbit Project, Tech. Rep. CERN-ATS-2009-096, CERN, Geneva. `https://cds.cern.ch/record/1215571`

Siegert, A. J. F. 1943, On the fluctuations in signals returned by many independently moving scatterers, Report / Radiation Laboratory, Massachusetts Institute of Technology, Cambridge, Mass.: Radiation Laboratory, Massachusetts Institute of Technology;. `https://www.tib.eu/de/suchen/id/TIBKAT%3A584715161`

Sigut, T. A. A., Mahjour, A. K., and Tycner, C. 2020, ApJ, 894, 18, doi: `10.3847/1538-4357/ab8386`

Stee, P., Allard, F., Benisty, M., et al. 2017, arXiv e-prints, arXiv:1703.02395. `https://arxiv.org/abs/1703.02395`

Ségransan, D. 2007, NewAR, 51, 597 , doi: `https://doi.org/10.1016/j.newar.2007.06.005`

Tan, P. K., Chan, A. H., and Kurtsiefer, C. 2016, MNRAS, 457, 4291, doi: `10.1093/mnras/stw288`

Ten Brummelaar, T. A., Sturmann, J., Ridgway, S. T., et al. 2013, JAI, 2, 1340004, doi: `10.1142/S2251171713400047`

Torres, G., Andersen, J., and Giménez, A. 2010, A&ARv, 18, 67, doi: `10.1007/s00159-009-0025-1`

van Belle, G., Baines, E., Boyajian, T., et al. 2019, arXiv e-prints, arXiv:1903.06750. `https://arxiv.org/abs/1903.06750`

van Belle, G. T. 2012, A&ARv, 20, 51, doi: `10.1007/s00159-012-0051-2`

Weiss, S. A., Rupert, J. D., and Horch, E. P. 2018, in Optical and Infrared Interferometry and Imaging VI, Vol. 10701, International Society for Optics and Photonics (SPIE), 255 – 261, doi: `10.1117/12.2313922`

Zampieri, L., Naletto, G., Barbieri, C., et al. 2016, in Proc. SPIE, Vol. 9907, Optical and Infrared Interferometry and Imaging V, 99070N, doi: `10.1117/12.2233688`

Zmija, A., Deiml, P., Malyshev, D., et al. 2020, OExpr, 28, 5248, doi: `10.1364/OE.28.005248`